On the laminar specificity of BOLD-based cortical activation profiles

Irati Markuerkiaga

On the laminar specificity of BOLD-based cortical activation profiles

Proefschrift

ter verkrijging van de graad van doctor
aan de Radboud Universiteit Nijmegen
op gezag van de rector magnificus, prof. dr. J. H. J. M. van Krieken,
volgens besluit van het college van decanen
in het openbaar te verdedigen op vrijdag 25 januari 2019
om 13:30 uur precies

door

Irati Markuerkiaga Olabe

geboren op 3 mei 1983
te Markina-Xemein, Spanje

Promotor:

   Prof. dr. David G. Norris

Manuscriptcommissie:

   Prof. dr. Floris de Lange   (voorzitter)

   Prof. dr. Sue Francis (University of Nottingham, Verenigd Koninkrijk)

   Dr. Natalia Petriodou (Universitair Medisch Centrum Utrecht)

On the laminar specificity of BOLD-based cortical activation profiles

Doctoral Thesis

to obtain the degree of doctor
from Radboud University Nijmegen
on the authority of the Rector Magnificus, prof. dr. J. H. J. M. van Krieken,
according to the decision of the Council of Deans
to be defended in public
on Friday, January 25, 2019 at 13:30 hours

by

Irati Markuerkiaga Olabe

born on May 3, 1983
in Markina-Xemein, Spain

Nire aurrekoei

Contents

Chapter 1

Introduction

The brain is the main organ associated with consciousness. The efforts to understand brain function do not only respond to an inherent interest of humans, but might be key to respond to challenges related to aging and new societal paradigms.

Since the early 80's, Magnetic Resonance Imaging (MRI) has been employed to obtain structural images with excellent image resolution and tissue contrast compared to other available techniques. Since the discovery in the early 90's that the MR signal was sensitive to blood oxygenation changes following local neural activation, functional MRI (fMRI) has become the workhorse to study brain function. A temporal correlation analysis of the local MRI signal with the used task allows the detection of brain regions involved in the given task.

Although task-based fMRI is still a widely used technique, the field has evolved to study brain networks, groups of brain regions that communicate with each other in certain situations and the hierarchical structure between them. Communication between brain regions takes place in the order of milliseconds, while the hemodynamic changes measured in MRI happen in the order of seconds. The temporal resolution of the technique does not allow for estimating the hierarchy and interdependencies between regions, unless an underlying model is assumed.

A method to establish interdependencies between regions that does not require modelling would be measuring activation at the cortical laminar level. It has been shown that layers in a region play a distinct role in passing on information to regions higher up in the hierarchy or to regions lower down in the hierarchy. Hence, there is an interest among neuroscientists in high-resolution functional MRI techniques that will deliver measures of cortical depth resolved activity.

High resolution fMRI has been performed by measuring any of the hemodynamic changes that follow neuronal activation. The approach easiest to implement and with the best temporal efficiency is the Gradient Echo based Blood Oxygenation Level Dependent (BOLD) approach. However, it has the poorest spatial specificity as the measured signal has a strong contribution from venous vasculature that is located downstream from the activation site.

1.1   Purpose of this work

This work is a collection of studies aiming at characterizing the laminar specificity of the static BOLD-response of mainly Gradient Echo based acquisitions.

First, in Chapter 6, a model of cortical vasculature is developed, and Spin Echo (SE) and Gradient Echo (GE) -BOLD profiles are simulated to study the laminar specificity of the two and estimate the physiological point spread function of the activation. Then, in Chapter 7, the use of this estimated PSF to deconvolve GE-BOLD profiles to obtain laminar specific activation profiles is studied.

SE-BOLD fMRI has a better laminar specificity than GE-BOLD based fMRI. Its implementation at 7 T can be cumbersome for a number of reasons, one of which being excessive power deposition. That is why, in Chapter 8, the use of non-balanced SSFP is studied as a means of obtaining SE-BOLD-like functional contrast and laminar specific activation profiles, but without the high-power deposition associated with spin echoes.

Increasing the image resolution leads to a decrease in signal to noise ratio. Most of the studies in high resolution functional MRI in humans have been acquired at 7 T. If the question studied allows it, SNR can be further increased if signal at a given cortical depth is averaged over a patch of cortex. Hence, in Chapter 9, laminar activation profiles are acquired at 1.5 T, 3 T and 7 T over a range of echoes and processed using the averaging approach to study the feasibility of laminar fMRI at lower fields.

1.2   Structure of this thesis

The following four chapters introduce the basic concepts to understand the motivation and the work carried out during this thesis. Chapters 6-9 are the scientific studies performed. Lastly, a summary and conclusions of this thesis are discussed in Chapter 10.

Chapter 2

Basics of MRI

Magnetic Resonance Imaging (MRI) is a technique that allows us to visualize non-invasively structures and processes in living subjects. It relies on the nuclear magnetic resonance (NMR) phenomenon, which occurs when nuclei that possess a spin are placed in an external magnetic field. In this chapter, first the NMR phenomenon is introduced, describing the interaction of nuclei with the external magnetic field and its temporal behaviour. Thereafter, it is explained how the spatial localization of the NMR signal is achieved and the basic sequences used in MRI are introduced.

2.1 The nuclear magnetic resonance phenomenon

2.1.1 The spin and the magnetic moment

Quantum mechanical spin is a basic property of elementary particles. Protons and neutrons belong to the family of fermions and carry a spin, I, with the quantum number 1/2. If the number of both neutrons and protons in a nucleus is even, spins are paired and cancel each other out, resulting in zero net spin. Nuclei in which the sum of the number of protons and neutrons is odd have a half-integer spin (i.e. $I = 1/2, 3/2, 5/2 \cdots$). Nuclei in which the number of protons and neutrons are both odd have an integer spin (i.e. $I = 1, 2, 3 \cdots$).

The spin angular momentum, $\boldsymbol{I}$, and magnetic moment, $\boldsymbol{\mu}$, are coupled by the element specific gyromagnetic ratio γ

$$\boldsymbol{\mu} = \gamma \boldsymbol{I} \tag{2.1}$$

Nuclear magnetic resonance can be observed in nuclei with non-zero net spin. Hydrogen is the most abundant element in the human body, and the most naturally abundant isotope of hydrogen is ^{1}H or protium (99.98%), which has spin 1/2. Hence, this is an excellent candidate for performing MRI *in-vivo*. The gyromagnetic ratio for ^{1}H is γ=42.58 MHz/T.

2.1.2   Interaction of the nucleus with an external magnetic field

In equilibrium the magnetic moments of individual nuclei are randomly distributed. As a result, the net magnetisation of the system is zero. In the presence of an external magnetic field, B_0, by convention in the z-direction, the I_z component of the angular momentum can align in 2I+1 ways reinforcing or opposing B_0:

$$I_z = m\hbar \tag{2.2}$$

where $\hbar$ is the reduced Planck constant $\hbar = h/2\pi$ ($h = 6.63 \times 10^{-34} Js$) and m are the eigenvalues of I_z, which can take the values m=-I,-I+1,...,I-1,I. Following Equation 2.1 and 2.2 it is clear that the z-component of the magnetic moment will also be quantized:

$$\mu_z = \gamma I_z = \gamma m \hbar \tag{2.3}$$

Each eigenstate corresponds to a precession of the magnetic moment around the z-axis at a fixed angle. Zeeman coupling describes the energy states of a spin in an external magnetic field in dependence of its orientation:

$$\hat{H} = -\boldsymbol{\mu} \cdot \boldsymbol{B_0} \tag{2.4}$$

where $\hat{H}$ denotes the Hamiltonian, the operator that corresponds to the total energy in the system. Hence, the discrete energy states, E_m, of the eigenvalues are:

$$E_m = -m\hbar\gamma B_0 \tag{2.5}$$

Hydrogen has spin 1/2, so it can take only two eigenvalues and can align in two ways: either parallel (m=+1/2) or antiparallel (m=-1/2) to B_0. The energy difference between these two states is given by:

$$\Delta E = E_{-1/2} - E_{1/2} = \hbar\gamma B_0 = \hbar\omega_0 \tag{2.6}$$

Equation 2.6 shows that the parallel state has a lower energy than the antiparallel state and that the state occupancy can be varied by applying an external magnetic field with an angular frequency $\omega_0 = \gamma B_0$, referred to as the *Larmor frequency*. The probability of occupancy of the two eigenstates depends on ΔE, the Boltzmann constant k_B ($k_B = 1.38 \times 10^{-23} J/K°$) and the absolute temperature T:

$$\frac{n_{\frac{1}{2}}}{n_{-\frac{1}{2}}} = e^{-\Delta E / k_B \cdot T} \tag{2.7}$$

where $n_{\frac{1}{2}}$ and $n_{-\frac{1}{2}}$ indicate the number of magnetic moments aligned parallel and antiparallel to B_0. As the state aligned parallel to B_0 is energetically more favourable, there is a net magnetic moment in that direction. Following Equation 2.7, at room temperature and at 7 T, the net magnetisation obtained is ~1/20000 of the maximum magnetisation. This net magnetisation, M_0, also called *sample magnetisation at equilibrium* or *longitudinal magnetisation*, is the source of the signal in magnetic resonance imaging. It is the sum of all individual magnetic moments, $M_0 = \Delta n \cdot \mu$, and after some derivations it can be shown that it can be expressed as:

$$M_0 = \frac{\rho_0 h^2 \gamma^2 B_0}{4 k_B T} \tag{2.8}$$

where ρ_0 is the proton spin density. The transverse component of the magnetisation in the equilibrium state is zero as there is no associated energy state and all orientations are equally probable. The net magnetisation obtained in MRI is rather weak. Equation 2.8 shows that for *in-vivo* measurements, the only parameter that can be varied to increase the available magnetisation is the external magnetic field, B_0, which explains the quest for higher field strengths in MRI.

2.1.3 Interaction of the nucleus with a radiofrequency pulse

According to the Newton's second law in rotational form, an external magnetic field, B, exerts a torque, T, on any magnetic moment, such as the sample magnetisation, M:

$$T = \frac{dI}{dt} = M \times B \tag{2.9}$$

Modifying Equation 2.1 for a system of spins to $M = \gamma I$, then Equation 2.9 can be written as:

$$\frac{dM}{dt} = M \times \gamma B \tag{2.10}$$

The net magnetisation induced by introducing the spins in an external magnetic field is parallel to this field and needs to be tilted away from the z-axis to measure an NMR signal. This is achieved by adding a transversal electromagnetic field B_1 in the x-y plane, generally rotating at the Larmor frequency, ω_0. As a result, following Equation 2.10, the net magnetisation will precess around the effective field B_{eff}, the total magnetic field experienced by the system:

$$B_{eff}(t) = \begin{bmatrix} B_1 \, cos\,(\omega_0 t) & B_1 \, sin\,(\omega_0 t) & B_0 \end{bmatrix} \tag{2.11}$$
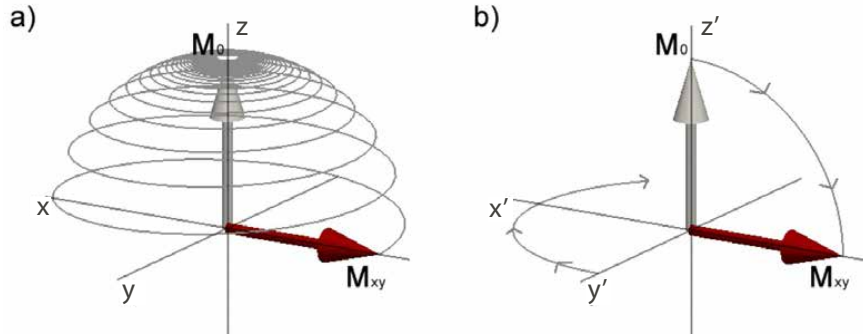
Figure 2.1: Trajectory of the magnetisation vector when an RF pulse that tips the magnetisation by 90° is applied **a)** in the laboratory frame of reference and **b)** in the rotating frame of reference.

The mathematical description of the magnetisation vector that results from the combination of B_{eff} and B_0 can be simplified by transforming the system from the laboratory frame of reference to the rotating frame of reference, a frame that rotates at ω_0 around the z-axis. In this frame of reference, precession around B_0 is invisible and B_1 can be chosen to be parallel to the x-axis, so the total magnetic field is

$$B'_{eff}(t) = \begin{bmatrix} B_1 & 0 & 0 \end{bmatrix} \tag{2.12}$$

In MRI, B_1 oscillates at the Larmor frequency, which in MR scanners is in the MHz range and is usually applied for a brief period of time. Therefore, it is generally referred to as a *radiofrequency (RF) pulse*. During the application of the RF-pulse, precession around B_1 occurs and magnetisation is tilted from the z-axis by an angle α, called the *flip angle*.

$$\alpha = \gamma \int_0^T B_1(t)dt \tag{2.13}$$

where T is the duration of the pulse. RF pulses that are applied with the purpose of tipping magnetisation to the transversal plane are called *excitation pulses*, whereas RF pulses that aim at tipping magnetisation by 180° are called *inversion* or *refocusing pulses*.

2.1.4   Spin relaxation

Once B_1 excitation has ceased, spins will return to the state of thermal equilibrium (i.e. net magnetisation along the z-axis). This process is called *relaxation*. There are two types of relaxation: the *spin-lattice* relaxation, which describes the recovery of the longitudinal magnetisation, and the *spin-spin* relaxation, which describes the loss of magnetisation in the transverse plane.

Spin-Lattice relaxation

The spin-lattice relaxation refers to the mechanism by which nuclei transfer the magnetisation received from the RF excitation to the environment they are embedded in, i.e. the lattice or tissue. As they transfer energy to the lattice, spins return to equilibrium and longitudinal magnetisation is recovered. It is governed by the relaxation time T_1, which can also be given as a relaxation rate $R_1 = 1/T_1$. Phenomenologically, spin-lattice relaxation is described by the differential equation

$$\frac{dM_z}{dt} = \frac{(M_z - M_0)}{T_1} \tag{2.14}$$

Considering $M_z(t = 0)$, then the solution to the differential equation is given by

$$M_z(t) = M_0(1 - e^{-t/T_1}) + M_z(0)e^{-t/T_1} \tag{2.15}$$

Energy is transferred to the surrounding lattice through the molecules that resonate at or near the Larmor frequency. With increasing B_0, the Larmor frequency increases and the number of molecules that can resonate at that frequency decreases. Hence, the energy transfer is less efficient and the T_1 is longer. The T_1 time depends on the properties of the surrounding material: for solid insulators it can be in the order of hours, whereas in conductors it can be in the order of milliseconds. Biological tissue, have relaxation times in the order of seconds, depending on tissue type and field strength (see Table 2.1).

Spin-Spin relaxation

The spin-spin relaxation refers to the mechanism by which spins lose phase coherence and the net transverse magnetisation induced by the RF-pulse disappears. As nuclei undergo Brownian motion, the local magnetic properties of the particles change and nuclei precess at slightly different frequencies ($\omega = \gamma B$). Hence the phase coherence that the particles had when the RF pulse was applied is eventually lost. The spin-spin relaxation time is known as T_2 and is sometimes given as a rate $R_2 = 1/T_2$. Mathematically, transverse magnetisation is given by:

$$\frac{dM_T}{dt} = \frac{-M_T}{T_2} \tag{2.16}$$

Considering $M_T(t = 0) = M_0 \sin(\alpha)$ the magnitude of the transverse magnetisation immediately after the RF pulse, then the solution to the differential equation is given by

$$M_T(t) = M_T(0)e^{-t/T_2} = M_0 \sin(\alpha)e^{-t/T_2} \tag{2.17}$$

T_1 is the time required to return to equilibrium and recover longitudinal magnetisation and T_2 governs the time required for transversal magnetisation to decay. Energy exchange between spins and the lattice will affect both the transverse and longitudinal components of the angular momentum of the spins, leading to a reduction of phase coherence. Hence, any process causing T_1 relaxation will also result in T_2 relaxation. However, an analytical description of the relationship between the two does not exist. If the system reaches equilibrium, the net magnetisation will be in z-direction and there will be no transversal component. Thus, it can be established that $T_2 <= T_1$ for all practical cases in MRI.

In addition to loss of phase coherence due to changes in the magnetic environment of the nuclei through Brownian motion, spins can lose coherence due to differences in the local distribution of B_0 through the sample. The dephasing induced by local inhomogeneities, ΔB_0, is given by $T_2' = \frac{2\pi}{\gamma \Delta B_0}$. Local inhomogeneities are considered not to vary over time, and hence, in the absence of spin motion, they lead to a static dephasing. The combined decay is given by

$$R_2^* = \frac{1}{T_2^*} = \frac{1}{T_2} + \frac{1}{T_2'} \tag{2.18}$$

It follows that $T_2^* <= T_2$. In biological tissue, B_0 differences arise from susceptibility differences between tissue types and structures, such as bone or air cavities. In fMRI, the susceptibility differences that arise from vascular structures with different oxygenation levels are especially relevant.

	T_1[ms]			T_2[ms]		
	1.5 T	**3 T**	**7 T**	**1.5 T**	**3 T**	**7 T**
CSF	4500	4300	4360	2200	1442	125
Grey Matter	950	1209	2000	100	90	50
White Matter	600	832	1300	80	80	36
Venous blood	1540	1623	2600	41	18	9
Arterial blood	1540	1623	2600	100	50	20

Table 2.1: Different tissues and blood compartments in the brain and their relaxation times from *Crémillieux et al.* (1998); *Poser* (2009); *Uludağ et al.* (2009), and references therein.

The Bloch Equations

The full dynamics of the magnetisation are described by the Bloch equations in which the spin relaxations given in the Equation 2.14 and 2.16 are combined with the motion of the magnetisation:

$$\frac{dM_x}{dt} = (M \times \gamma B)_x - \frac{M_x}{T_2}$$
$$\frac{dM_y}{dt} = (M \times \gamma B)_y - \frac{M_y}{T_2} \qquad (2.19)$$
$$\frac{dM_z}{dt} = (M \times \gamma B)_z - \frac{M_z - M_0}{T_1}$$

As transverse magnetisation, M_T, is given as: $M_T = M_x + iM_y = M_T e^{-i\omega_0 t}$, it follows

$$\frac{dM_T}{dt} = -i\gamma M_T B_z - \frac{M_T}{T_2}$$
$$\frac{dM_z}{dt} = (M \times \gamma B)_z - \frac{M_z - M_0}{T_1} \qquad (2.20)$$

2.2 Basics of Magnetic Resonance Imaging

The NMR signal needs to be localized in space in order to obtain images. As seen in the previous section, the precession frequency of a nucleus depends on the surrounding magnetic environment. Therefore, if the magnetic field is varied as a function of spatial location, it should be possible to localize the origin of the signal by determining the precession frequency. This spatially dependent variation of the magnetic field is done by generating *magnetic field gradients*. These field variations are created by 3 pairs of coils, one per x, y and z direction in space, that generate an (ideally) linear field change. Hence, the strength of the magnetic field, and the precession frequency, become position dependent

$$\omega(r) = \gamma(B_0 + rG) \qquad (2.21)$$

where $r(x, y, z)$ is the position vector and $G(G_x, G_y, G_z)$ is the gradient vector. Typical gradient magnitudes are of the order of mT/m, about two orders of magnitude weaker than the B_0 field but considerably larger than field variations due to field inhomogeneities.
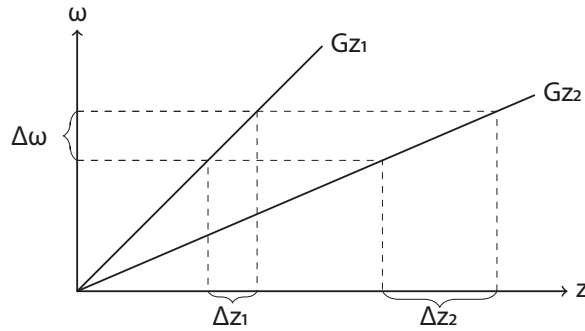
Figure 2.2: The principle of slice selection. An RF pulse with bandwidth $\Delta\omega$ is applied together with the slice select gradient G_z and only spins that meet the resonance condition are excited. The gradient strength defines the slice thickness, whereas the slice profile is defined by the RF pulse shape. Weaker gradients, e.g. G_{z2}, excite a thicker slice, stronger gradients, e.g. G_{z1}, a thinner one.

2.2.1   Image encoding

In this section, image encoding, the way spatial variations of the magnetic field lead to an MRI image is described first. Afterwards, the k-space formalism and the constraints that have to be met by the applied field gradients to avoid aliasing artefacts or considerable blurring in the image are explained.

Slice selection

Slice selection consists of the process of spatially localizing the spins that will be excited by the RF pulse that is played out. This is achieved by simultaneously applying a field gradient and an RF pulse. By convention, the field gradient is assumed to be in z-direction, but it can be applied in any direction. The RF pulse has a carrier frequency ω_c, and a bandwidth, $\Delta\omega$. As shown in Figure 2.2, for a fixed gradient strength, the position, z_0, is determined by the carrier frequency of the RF pulse (Equation 2.22) and the slice thickness, Δz, by the bandwidth of the pulse (Equation 2.23).

$$z_0 = \frac{\omega_c}{\gamma G_z} \tag{2.22}$$

$$\Delta z = \frac{\Delta\omega_c}{\gamma G_z} \tag{2.23}$$

The application of the slice gradient is necessary for slice selection but induces a position dependent phase accumulation in the slice direction that leads to a signal

loss in the transverse plane because spins dephase. In order to obtain a signal, the slice selection gradient needs to be followed (or less commonly preceded) by a rephasing lobe. For slice selection gradients with RF pulses symmetric about the centre of the gradient lobe, the 0th moment of the rephasing lobe needs to be half of that of the slice selection gradient (see Figure 2.3a).

The envelope of the RF pulse determines the slice profile that can be achieved. For flip angles smaller than $30°$, the small flip angle approximation holds and the transversal magnetisation, M_T in Equation 2.20, is the Fourier transform of the temporal waveform of $B_1(t)$.

The ideal slice profile would be a perfect rectangle, the Fourier transform of which is an infinitely long sinc function. As it is not physically feasible to have an infinitely long pulse, the sinc function is truncated and only the main lobe with a number of sidelobes is played out. To reduce Gibbs ringing artefacts, the B_1 waveform is sometimes multiplied with a smoothing window (e.g. Hann, Hamming) to ensure a smoother transition to zero. Waveforms with more sidelobes result in slice profiles closer to the ideal rectangular shape. If the duration of the pulse is fixed, the number of sidelobes played out is increased by increasing the bandwidth of the pulse, which needs to be accompanied by an equivalent increase in gradient strength so that the slice thickness is unaltered. This can potentially hit two limits: gradient strength limits and Specific Absorption Rate (SAR) due to the increase in bandwidth.

Frequency encoding

By convention, frequency encoding is applied in x-direction and is often referred to as read-out gradient encoding because it is applied while signal is being acquired (see Figure 2.3a). When the gradient G_x is applied, following Equation 2.21 the precession frequency of the spins will be depend on the position in the x-direction. The strength of the applied gradient determines the range of frequencies contained in the MR signal. The signal received in the receive coil at time t, $S(t)$, is the sum over the whole object:

$$S(t) = \int_x \rho(x) e^{-i\gamma \int_0^t G_x(t)x dt} dx \tag{2.24}$$

where $\rho(x)$ is the spin density along the x-direction. As the gradient does not usually vary over time, the expression is simplified to:

$$S(t) = \int_x \rho(x) e^{-i\gamma G_x x t} dx \tag{2.25}$$

Equation 2.25 shows that the time-varying signal recorded is the Fourier transform of the projection in the x-direction of the spin density, ρ.

Phase encoding

Phase encoding is the process in which signal is spatially encoded in the remaining orthogonal direction in space, the y-direction. The end-result of the phase encoding is mathematically analogous to the frequency encoding, but the way this is achieved differs substantially. Phase encoding consists in applying a gradient in the y-direction for a certain amount of time that dephases the signal prior to acquisition (see Figure 2.3a).

$$\Delta\varphi(y) = \gamma \int_0^{t_{PE}} y G_y(t) dt \tag{2.26}$$

where $\Delta\varphi$ is the phase accrued and t_{PE} is the duration of the gradient. As the applied gradient is usually constant over time, the above expression is reduced to $\Delta\varphi(y) = \gamma G_y t_{PE} y$. The phase accrued depends on the position y along the y-axis, but there is no frequency dependence in this direction. Hence, it is not possible to localize the origin of the signal after applying the phase encode gradient only once. That is why, this process is repeated varying the amount of dephasing induced until all required samples in y-direction are acquired. This is, the phase change is encoded over time, which is mathematically equivalent to frequency encoding. For practical reasons, the induced phase variation at each repetition is modulated varying the gradient intensity, G_y, and not the gradient duration, t_{PE}.

Once all the samples have been acquired, the obtained signal can be expressed as

$$S(t, G_y) = \int_y \int_x \rho(x, y) e^{-i\gamma(G_x x t + G_y y t_{PE})} dx dy \tag{2.27}$$

where $\rho(x, y)$ is the spin distribution in the sample.

3D Imaging

If the slice profile is limited by timing and gradient requirements, 3D image would be an alternative. Instead of individually exciting a slice, a volume/slab is excited and the z-direction is encoded through phase encoding, as explained in the previous section. The signal acquired is described by an equation similar to Equation 2.27, but with two phase-encoded directions instead of one.

$$S(t, G_y, G_z) = \int_z \int_y \int_x \rho(x, y, z) e^{-i\gamma(G_x x t + G_y y t_{PE_1} + G_z z t_{PE_2})} dx dy dz \tag{2.28}$$

where t_{PE_1} and t_{PE_2} are the durations of the phase encoding gradients in the y and z directions, respectively.

This image encoding scheme does not suffer from slice profile problems, it can easily be accelerated in both phase encoding directions and, everything else kept equal, the SNR increases with $\sqrt{N}$. In practice, though, the increase in SNR is reduced because the time between successive RF pulses that excite the whole slab is shorter and the available magnetisation is reduced as it becomes saturated.

K-space formalism

Equation 2.28 shows that the signal acquired in MRI is the Fourier transform of the spin distribution of the object (neglecting any contrast differences due to different relaxation times across the object). The expression is simplified if the k-space formalism is adopted. In k-space, the spatial encoding terms are transformed into spatial frequencies by converting them to wave numbers, k, a measure of cycles per unit distance:

$$\mathbf{k}(t) = \frac{\gamma}{2\pi} \int_0^t \mathbf{G}(t')dt' \tag{2.29}$$

The k-space formalism is a useful tool to understand image acquisition in MRI. It shows that the k-space point acquired depends on the magnitude of the gradient applied and the time elapsed from the start of the gradient to the time at which the k-space point is acquired. This is, the 0th moment of the gradient in each of the directions at time-point t will determine the k-space point that is acquired. Equation 2.28 can be re-written as:

$$S(k_x, k_y, k_z) = \int_z \int_y \int_x \rho(x, y, z)e^{-i(k_x x + k_y y + k_z z)}dxdydz \tag{2.30}$$

As mentioned earlier, Equation 2.30 corresponds to the Fourier transform of the real object $\rho(x, y, z)$. Following the properties of the Fourier transform of a real signal, the acquired k-space data is conjugate symmetric. This implies that acquiring half of k-space would be enough to be able to reconstruct the image. In practice, though, it is necessary to acquire at least a little bit more than half of k-space in order to reconstruct the data. Nonetheless, this redundancy in the acquired signal can be exploited to speed up acquisition (i.e. *Partial Fourier* acquisition).

Sampling and gradient requirements

In the previous section, it was assumed that sampling in k-space is infinite and continuous in time. In practice, of course, this is not the case and gradients have to fulfill some requirements to avoid artefacts related to discrete sampling.

The Nyquist theorem states that a signal needs to be sampled at twice the rate of the highest frequency contained in the signal, if it is to be reconstructed unambiguously. Hence, if τ is the time between two acquired samples, the highest frequency that it will be possible to distinguish will be $1/2\tau$. In practice, MR signals are acquired using quadrature detection, acquiring two samples per time point, one for the real and for the imaginary component. Hence, it is possible to distinguish a range of frequencies between $-1/2\tau$ and $+1/2\tau$, which effectively yields a bandwidth, BW, of $1/\tau$. As the read-out bandwidth and the bandwidth

of the analog to digital converter are matched, this means that the gradient in x direction, G_x, has to be

$$G_x = \frac{BW}{FOV_x} = \frac{1}{\tau FOV_x} \qquad (2.31)$$

where FOV_x is the field of view in x-direction. The requirements for the phase-encoding direction is that the weakest gradient applied, i.e. the first gradient step ΔG_{PE} ,that corresponds to the first wavenumber, has to induce a change of 2π between the edges of the FOV_y:

$$\Delta G_{PE} = \frac{2\pi}{\gamma \tau_{PE} FOV_y} \qquad (2.32)$$

If Δk_x is the difference between two points in x-direction in k-space given by $\Delta k_x = \tau G_x$, then, from Equation 2.31:

$$FOV_x = \frac{1}{\Delta k_x} \Leftrightarrow \Delta x = \frac{1}{FOV_{k_x}} \qquad (2.33)$$

This is, the field of view is determined by the sampling density of the k-space, Δk_x. Similarly, image resolution, Δx, is determined by the k-space coverage in that direction, i.e. by the largest frequency encoded. The subscripts in Equation 2.33 refer to the x-direction, but this relationship also holds for the phase encoding direction. In practical terms, though, there is a difference between the two. If the scanned object is larger than the FOV in the read-out direction, the parts that are not in the FOV can be filtered out in the acquisition by applying a bandpass filter that will filter out any signal that originates outside the FOV. In the phase encoding direction, however, this is not an option as the individual acquisitions do not have any frequency components. Therefore, the FOV_{PE} has to be larger than the scanned object in that direction, otherwise signal from outside the FOV will be wrapped around into the FOV.

Image Point Spread Function

According to the properties of the Fourier transform, the frequency spectrum of a finite image can be of infinite length. However, the k-space is limited and therefore, the spectrum of the image is truncated. Mathematically this is equivalent to having the original spectrum multiplied by a rectangular or box-car function

$$S'(\boldsymbol{k}) = S(\boldsymbol{k})rect\left(\frac{\boldsymbol{k}}{\boldsymbol{k_{max}}}\right) \qquad (2.34)$$

with Fourier transform,

$$I'(x) = I(x) * \frac{sin(2\pi k_{max} x)}{\pi x} = I(x) * \frac{sin(\pi x / \Delta x)}{\pi x} \tag{2.35}$$

Equation 2.35 shows that the obtained image is the actual image convolved with the sinc function. Hence, due to truncation of k-space, a point in the image will spread across the image. This is referred to as the *sampling PSF*.

In the discussion about image encoding in MRI, it was assumed that signal relaxation was negligable during the acquisition of k-space. In sequences that acquire several k-space lines after a single excitation, this assumption might be invalid. In these cases, T_2 relaxation across the phase encoding direction will be present and k-space will be further weighted by an exponential term: e^{-t/T_2}. The Fourier transform of an exponential is a Lorentzian. Therefore, another convolution term will have to be added to the equation above. However, as long as the blurring induced by the Lorentzian is smaller than the BW/pixel, T_2-relaxation will not result in additional blurring. This is the case if the BW/pixel is larger than $1/\pi T_2$. This constraint holds also if relaxation is governed by T_2^* decay.

2.2.2   Pulse sequences

RF pulses are necessary to obtain an NMR signal and controlled variations of the magnetic field are applied to obtain an image that is a realistic representation of the object. The timing, magnitude and shape of the RF and gradients are written into the pulse sequences that are played out by the MR scanner. Two important timing parameters are: the *time of repetition*, *TR*, the time between two adjacent excitation pulses, and the *echo time*, *TE*, which corresponds to the time elapsed between the excitation RF pulse and the centre of the acquisition of the signal (unless asymmetric acquisition is used). These times determine to a large extent the signal to noise ratio (SNR) and the contrast of the image, i.e. if the image contrast is based on differences in T_1, T_2 and proton density properties among different tissues. For instance, if differences in T_1-times between different tissue types are the source of the contrast, it is referred to as a T_1-weighted acquisition/image.

MR sequences can be represented in diagrams, which are helpful for users and developers to understand the said sequence. These diagrams often only show the RF pulse(s) and gradient waveforms that correspond to one repetition period. It is implicit that this sequence will be repeated with the corresponding changes in the encoding gradients and (if necessary) in the RF pulses as many times as required to fill out all the points in k-space.

Spin Echo Sequences

The spin-echo (SE) sequence consists of a 90° pulse followed by a 180° pulse. The SE diagram shown in Figure 2.3 corresponds to a 2D image encoding scheme, where localization in the slice direction is performed by slice selection. The excitation pulse used is symmetric and located in the centre of the slice selection gradient lobe. Hence, this gradient lobe is followed by another with the opposite sign and half the area (0th moment) to rephase the dephasing across the slice induced by the slice select gradient. The slice selective 180° pulse does not have such a lobe because the phase dispersion accrued in the first half of the pulse is rephased during the second half.

The way the gradients are played out for in-plane image encoding determines how the k-space data are acquired. The first gradient lobe in the read-out direction dephases spins and brings them to the $+k_{x,max}$. The refocusing pulse induces a 180° phase shift, which brings the magnetisation to the $-k_{x,max}$ position in k-space. Subsequently, prior to acquisition, the phase encoding gradient is applied. The phase accrued during the phase-encoding gradient moves the magnetisation vector in y-direction in k-space. Signal is acquired during the read-out gradient. The total area under this gradient is twice as large as the dephasing lobe applied earlier in this direction, so k-space is traversed from $-k_{x,max}$ to $+k_{x,max}$. Usually, the read-out gradient is timed such that the centre of the echo formed due to the combination of the 90° and 180° pulses falls in the centre of the gradient and therefore k-space. This process is repeated until all lines in k-space are acquired.
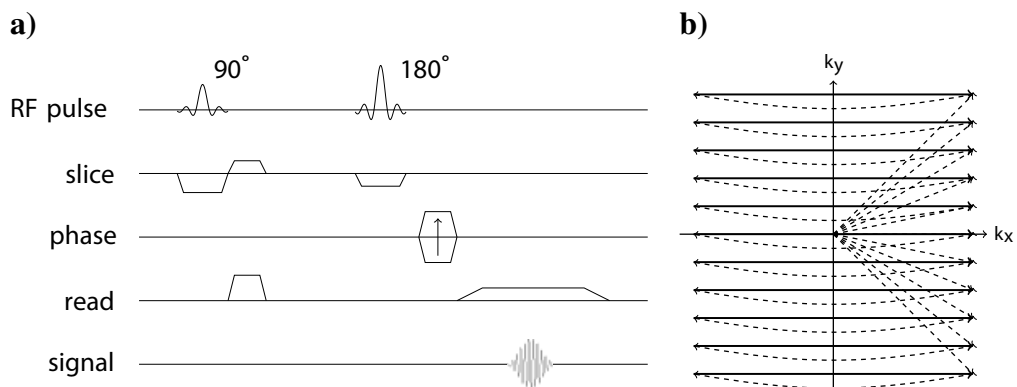

Figure 2.3: **a)** Sequence diagram of a spin echo sequence and **b)** navigation through k-space.

In practice, the acquisition of SE images is often accelerated by acquiring a number of k-space lines after a single excitation pulse by applying successive 180° pulses and varying the phase encoding gradient. This technique is known under
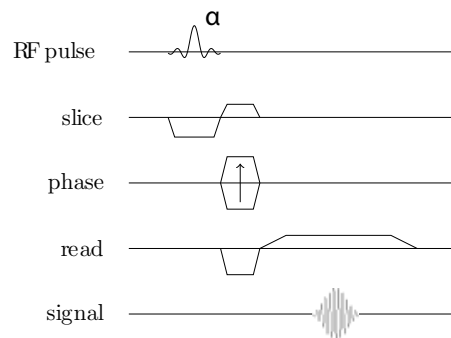
Figure 2.4: Sequence diagram of a gradient echo sequence.

different names, such as rapid acquisition with relaxation enhancement (RARE), turbo spin echo (TSE) or fast spin echo (FSE). Alternatively, acquisition can be further accelerated if the entire image is acquired in a single shot. In order to do this, the acquisition has to be faster than the relaxation time T_2. This can be achieved with the acquisition scheme mentioned earlier but acquiring only the minimum necessary portion of k-space (i.e. half Fourier acquisition single-shot turbo spin echo, HASTE) or by combining it with an echo planar image encoding method (see section below).

Gradient-Echo Sequences

The gradient echo (GE) sequence has a single excitation pulse that tips magnetisation by a flip angle (FA) α, which is in general smaller than 90°. Signal is then acquired as soon as allowed by gradient timing constraints. Note, that as opposed to the SE sequence, the dephasing lobe in the read-out direction needs to have the opposite polarity to the read-out lobe, because there is no 180° pulse that will reverse the polarity.

The relationship between TR and T_2 determines the characteristic of the GE signal:

- TR»T_2: *Conventional GE*. Transversal magnetisation is fully dephased by the time the next RF pulse is applied. Therefore, RF pulses will only excite the longitudinal signal component, which after some repetitions will reach steady state.

- TR<T_2: *Fast GE*. Transversal magnetisation has not fully dephased at the time of the following RF pulse and it will appear as a stimulated echo at a later stage. There are two ways of dealing with this:

– Approach 1: Make sure that the transversal magnetisation does not contribute to the signal acquisition in later repetitions. This can be achieved by RF spoiling or using crusher gradients after read-out. This way, the signal acquired after each RF pulse is only the result of the FID generated after the pulse and will be purely T_2^* weighted (T_2^*-w FLASH).

– Approach 2: Allow that the residual transversal magnetisation coherently adds in the form of stimulated echoes to later signal acquisitions. These types of sequence are called *Steady State Free Precession (SSFP)* sequences. They have the advantage of having a better SNR, but are more prone to motion artefacts. There are two main groups within the SSFP sequence family.

* *Non-balanced SSFP*: The net gradient within a TR is not zero. These sequences give rise to two signals: the S1 or FID signal right after the excitation pulse, and the S2 or spin echo signal right before the following excitation pulse. In fact, the spin echo signal appears at the time in which the RF pulse is applied, but as it is not possible to transmit and receive at the same time, signal is acquired right before the RF pulse is applied by playing out a rewinding gradient. Hence, the S2 signal is not a pure spin echo and will have some T_2' weighting in it. Sequences can be tuned to acquire only the S1 (with multiple repetitions if desired), only the S2 or both S1 and S2 signals.

* *Balanced SSFP*: The net gradient moment is zero in all gradient directions. In this case, the signal acquired is the sum of the S1 and S2 signal. It presents the best SNR from all the fast gradient echo sequences, but it is very sensitive to susceptibility differences across the imaging volume, which, if that is the case, gives rise to banding artefacts in the image.

• *Ultrafast GE*: there are mainly two subgroups in this category. Those that acquire an image encoding line after each excitation with very low FA and TR, but have a contrast preparation module before the image encoding starts (for example, Turbo-FLASH). The second group is the echo-planar imaging (EPI) technique, in which several image encoding lines are acquired after an RF excitation pulse by means of fast switching of the gradients.

In GE, the TR is considerably shorter than T_1. Therefore, longitudinal magnetisation will not have recovered and a 90° excitation pulse will in general not be the FA that will lead to the maximum amount of signal and SNR possible. For conventional and fast-gradient echo approaches without residual transverse magnetisation at the end of the repetition, the FA that will lead to the largest amount of magnetisation is given by the Ernst angle (θ_E):

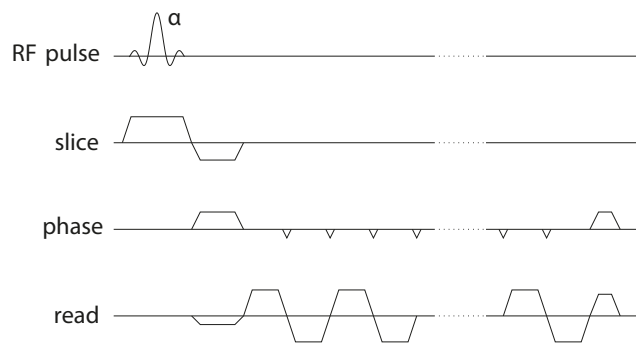$$\theta_E = arccos(e^{-TR/T_1}) \tag{2.36}$$

Figure 2.5: A gradient echo sequence with echo planar image encoding.

Echo Planar Imaging

Echo Planar Imaging (EPI) is an image encoding method for accelerating image acquisition. After a preparation module, for example, a single RF pulse (GE-EPI) or a 90°-180° pair of pulses (SE-EPI), several k-space lines are acquired by rapid switching of the image encoding gradients. A strong dephasing in the phase encoding direction is applied to subsequently traverse k-space from one line to the next by applying gradient blips, which induce a small phase increment each time (Figure 2.5). A further difference to the image encoding explained earlier is that adjacent k-space lines are acquired with reversed polarity; if k-space is traversed from left to right in one line, the next line is acquired from right to left. Hence, alternating lines need to be reversed prior to reconstruction. This image encoding scheme allows to acquire a whole brain image in a few seconds with a resolution in the order of a few millimetres. Therefore, it is a popular technique to measure dynamic processes, such as brain function.

The gain in speed comes at the cost of a number of image artefacts. The rapid switching of (potentially strong) gradients leads to some undesired effects in the scanner hardware, such as Eddy currents. Modern scanners compensate for Eddy currents by introducing pre-emphasis in the gradients. However, there remain residual phase differences between alternating k-space lines that lead to a FOV/2 image displacement in the phase-encoding direction, the so-called Nyquist ghosting artefact. In order to correct for this, EPI acquisitions are preceded by the acquisition of at least two k-space lines with no phase encoding, one in each read-out polarity. The phase difference between the two is used to correct the phase difference of alternating lines during image reconstruction.

The other main group of artefacts in EPI are drop-out and distortion artefacts, both related to the combination of macroscopic field inhomogeneities and the long acquisition trains in EPI (see *Schmitt et al.* (1998) for a thorough description). If there is a field gradient along the slice-direction, signal in the voxel will dephase, leading to signal attenuation or drop-out. This effect increases with echo time and

field strength, as signal will have more time to dephase and will dephase, faster, respectively. Drop-outs are not a problem in SE-EPI as the signal is rephased at the centre of k-space.

If the field gradients are in plane, the acquired image will be distorted. In the read-out direction, there will be an extra phase accumulation that will not be rephased between successive lines, leading to a skewed acquisition of k-space that will manifest as a sheared image in the image domain. If the field gradient in the phase-encoding direction it will lead to image stretching (if the field gradient re-inforces the phase encoding gradient) or compression (if the field gradient opposes the phase encoding gradient) in the PE-direction. In-plane artefacts are usually noticed only in the phase-encoding direction because the BW/pixel is much smaller in this direction (*Schmitt et al.*, 1998).

Reducing the acquisition time in EPI reduces the image artefacts related to field inhomogeneities. Acquisition time reduction can be achieved by splitting the acquisition into a number of segments with a short enough acquisition time or accelerating the acquisition using parallel acquisition techniques. Parallel techniques reduce the acquisition time by omitting some k-space lines. The missing information will be estimated in post processing relying on the fact that signal from the same object is acquired in each of the coils (referred to channels) and that each of these coils have a different spatial sensitivity. Hence, these techniques can only be applied if multiple coils are used for acquisition. There are a number of techniques available to estimate the missing data. SENSE-like techniques perform image reconstruction in image-space while GRAPPA and SMASH do this in k-space. The acceleration factor, R, is a measure of how much the acquisition time is reduced. Image SNR decreases with $\sqrt{R}$ and there is a g-factor, geometry factor, penalization that leads to noise amplification in the centre of the FOV, where the coil sensitivities are weakest in multi-channel head coils.

Chapter 3

Physiological basis of functional MRI

The understanding of the functional MRI signal requires a basic knowledge of brain anatomy and physiology. In this section, first a general overview of the functional organization of the brain, including the role of cortical layers, is given. Thereafter, the cortical vasculature, the source of signal contrast in current functional MRI techniques, is discussed. Lastly, the neurovascular coupling, the link between neuronal activity and the vascular response, is briefly described.

3.1   Functional organization of the brain

3.1.1   The neuron

The neuron is the basic processing unit of the brain (see Figure 3.1). The soma or cell body integrates the signal coming from the tens or hundreds of dendritic terminations around it. If the result of that integration is above a certain threshold, an impulse response will be generated and transmitted via the axon to the synaptic terminations. These will release neurotransmitters into the synaptic cleft, which will be captured by a dendritic termination of the soma of another neuron.

The cell membrane, a lipid bilayer, maintains a resting potential of -60mV. This potential is achieved by means of ion concentration gradients in the internal and external environments. Resting neurons have a higher concentration of K^+ inside the membrane, whereas the concentration of Na^+, Ca^{2+} and Cl^- is higher outside. The resting potential is modified through neurotransmitters that reach the synapse that selectively open ion channels, leading to a change in ion concentrations across
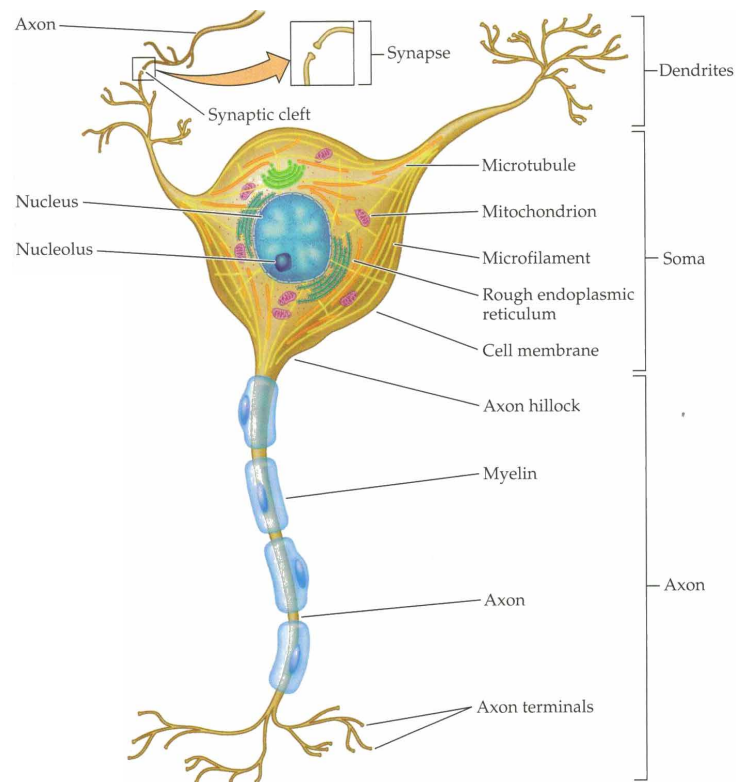
Figure 3.1: A representation of a neuron with its most relevant parts. Picture taken from *Huettel* (2004).

the membrane. The resting potential can be restored by the sodium-potassium pump, which requires energy.

Neurons are classified into excitatory and inhibitory neurons, based on the effect they have on the activity of other neurons. Excitatory neurons release neurotransmitters, e.g. glutamate (Glu), that contribute to the depolarization of the cell membrane of the receiving neuron. If the cell membrane is depolarized, then an action potential propagates through the axon and neurotransmitters will be released at the end of it. Inhibitory neurons release neurotransmitters that hyperpolarize the cell membrane, such as gamma-aminobutyric acid (GABA). Hence, inhibitory neurons prevent the generation of an action potential in the receiving neuron. Repolarizing the cell membrane after the release of an action potential is the process with the highest energy cost in the brain. Hence, excitatory activity is energetically the most demanding activity and inhibitory synaptic activity is likely to have a much lower energy cost.

80% of the neurons in the cortex are excitatory, mostly pyramidal neurons. These neurons are named after their pyramidal shape, with the apical vertex pointing usually towards the cortical surface. Inhibitory neurons are fewer in number (around

20%), but much more diverse in shape and function than their excitatory counterparts.

In this section the basic functioning of the neuron is described, the interested reader can refer to *Buxton* (2009) or *Huettel* (2004) for an extended description.

3.1.2 Subdivisions of the brain

Macroscopically, there are three subdivisions of the brain that are relevant for fMRI:

1. Cerebrospinal fluid (CSF): this is a plasma-like fluid located around the brain (between the neo-cortex and the skull) and in the brain cavities, such as the ventricles (see Figure 3.2). It serves various purposes, among which are protecting the brain against mechanical shocks, waste clearance and blood flow regulation.

2. Grey matter (GM): contains the soma of neurons where signal integration and processing take place. Sub-cortical grey matter can be found in the structures in the ventral side of the brain, such as basal ganglia, hippocampus or substantia nigra, among others. GM in the outer part of the brain is known as the neo-cortex, and consists of a thin sheet of neurons located between CSF and WM. The neo-cortex is highly convoluted in humans and the thickness of the GM varies between 1-5 mm depending on cortical region and local curvature.

3. White matter (WM): contains the axons of the neurons over which the electrical impulse (also known as action potential or spike) travels from the soma to the synapses from one cortical region to another. Axons are covered by myelin, a lipid rich substance forming an electrically insulating layer that protects the axon.

3.1.3 The Grey Matter

The most relevant brain compartment in functional MRI is grey matter because the core of the neural processing takes place here. The grey matter is a densely packed sheet of brain cells, mostly the soma of the neurons, but also axons making local connections, astrocytes and other glia cells. Based on the features and density of the cell bodies measured by Nissl staining, in 1909 Brodmann distinguished 52 different regions in the human neocortex. This classification is still in use nowadays, as research has shown that these areas largely correspond to functional areas. For example, Brodmann Area number 17 (BA-17) corresponds to the primary visual cortex (also known as V1), the region in the neocortex that receives via the LGN (Lateral Geniculate Nucleus) the visual input originating from the retina.
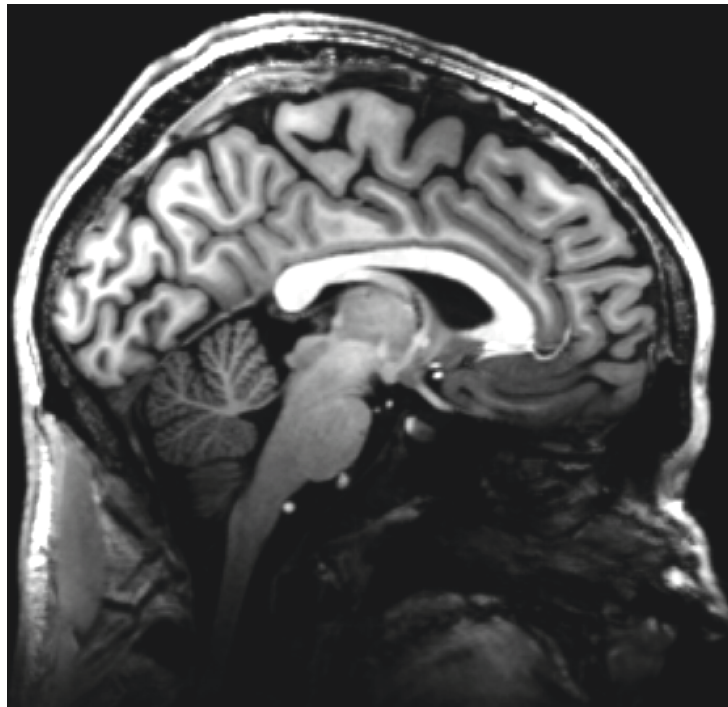
Figure 3.2: Sagittal view of a T_1-weighted MR scan. The grey matter in the neocortex, in the outer rim of the brain, is easily distinguished from the white matter located just below. CSF appears black in this image, as shown by the lack of signal from the cavity in the middle of the brain.

3.1.4   Functional hierarchy in the brain

The study of information flow in the sensory-motor areas has shown that information flow follows a hierarchical structure. In sensory processing, the sensory input goes first to subcortical areas (such as the thalamus), then to primary cortical areas (such as the primary visual cortex) and then to other higher order Brodmann areas where the information is combined with that of other regions and decisions on the response to the stimulus are taken. This pattern describes the bottom up driving flow of information, which is also called a feed-forward or ascending pathway. However, the information flow has a feed-back or descending pathway by which areas higher up in the hierarchy communicate with lower order areas modulating the driving signal. Feedback modulatory mechanisms can be conditioned for example by attention or expectation. While excitatory neurons are the main agents in the feed forward pathway, inhibitory neurons are most relevant in the feedback modulatory pathway (*Rockland*, 2017).

3.1.5   Laminar structure of the cortex and cortical processing

Within a Brodmann region, the distribution of cells is not homogeneous. The cell type and density vary following a laminar structure parallel to the cortical

surface (see Figure 3.3). Most neocortical regions have six distinct layers, based on features of the cytoarchitecture. The layers are numbered from I (closest to the pial surface) to VI (closest to WM). Layer IV is often called the granular layer, due to the grain like aspect it shows after ink staining. Layers between layer IV and the pial surface are then referred to as supragranular layers. Analogously, layers between the granular layer and the white matter are called the infragranular layer. An exception to the rule of the 6-layer structure is the primary motor cortex (M1), which does not have a granular layer. The neural composition and thickness of the layers varies across cortical regions. For example, the granular layer in V1 takes up almost 30% of the cortical thickness whereas in V2 it is only 15% (*de Sousa et al.*, 2010). Within a region, the grey matter and laminar thickness vary as a function of the cortical curvature following the equivolume principle as first observed by *Bok* (1926). The relative volume of the layers is preserved along the cortex over flat patches, gyri and crowns. Therefore, in a crown, superficial layers will be thinner as there is a larger surface to locate the brain cells that belong to it. Similarly, in a gyrus, the superficial layers will be thicker.

Felleman and Van Essen (1991) reported that cortical layers played distinct roles regarding information flow in the brain. Based on their reach (between or within regions) and nature (excitatory or inhibitory), laminar connections can be classified into five groups (*Rockland*, 2017):

Extrinsic connectivity:

- Extrinsic projecting neurons: These are the connections that occur from one region to other regions (see 'OUTPUT to' column in Figure 3.4). Although there is some variability between cortical regions, in general:

    - Layer I contains some inhibitory neurons and dendritic terminations of pyramidal cells from lower layers within the region. Neurons here do not project extrinsically.

    - Neurons in the supragranular layers (II and III) project only to other cortical regions.

    - Layer IV (granular layer) does not project to other regions.

    - The infragranular layers project both to other cortical regions and to subcortical regions (i.e.: thalamus, pons, . . .).

- Extrinsic connections: These are the connections to one region from other regions (see 'INPUT from' column in Figure 3.4).

– Layer I receives input from subcortical regions (i.e. amygdala, association thalamus and the zona incerta) and other cortical regions.

– Connections from non-cortical regions (such as the thalamus or the pulvinar region) tend to terminate in the middle zone of the cortex. For example, in V1, these connections terminate in upper layer IV and lower layer III.

– Layer IV receives the input from layer III from lower cortical regions.

– Infragranular layers receive the feedback input from higher order cortical regions. Layers V and VI are interconnected. The local circuitry is more strongly interconnected in Layer V than in layer VI. Layer VI is involved more in being a source and a target of extrinsic connections.
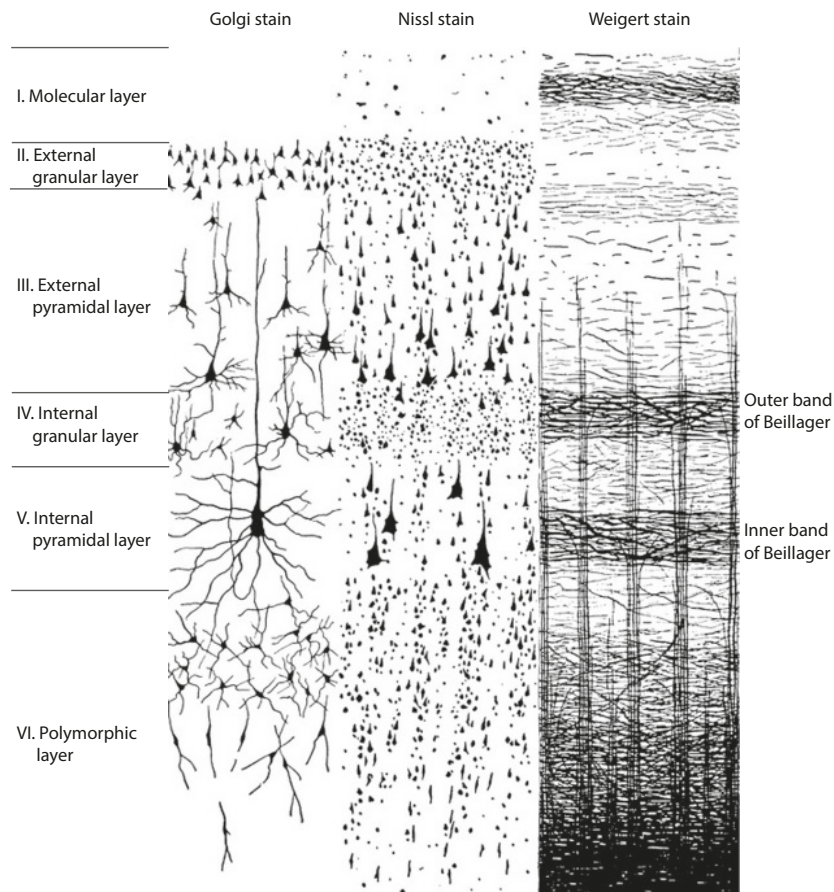
Figure 3.3: Cross section of neocortex stained by three different methods. The Golgi stain reveals the shapes of the arborizations of cortical neurons by completely staining a small percentage of them. The Nissl method stains the cell bodies of all neurons, showing their shapes and packing densities. The Weigert method stains myelin, revealing the horizontally oriented bands of Baillarger and the vertically oriented collections of cortical afferents and efferents.
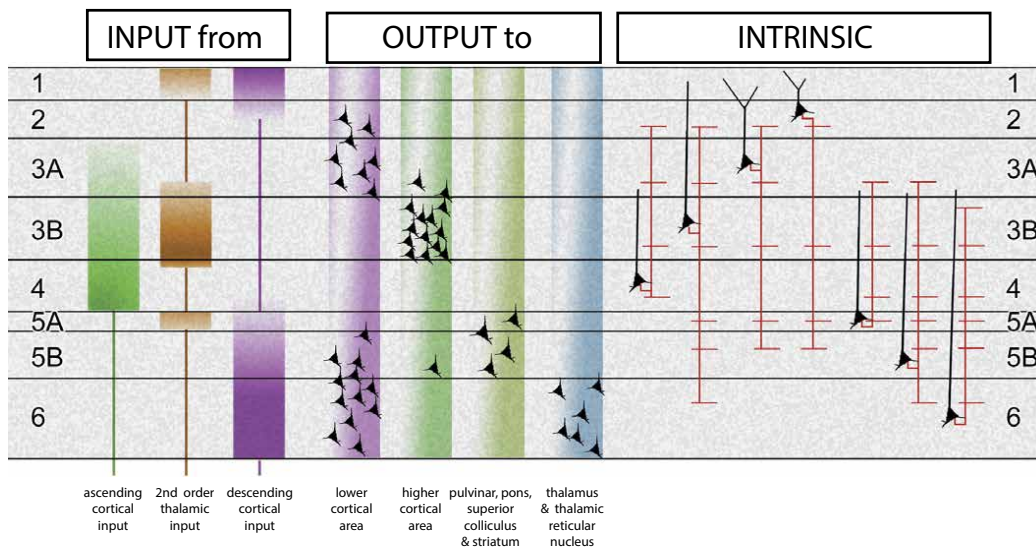
Figure 3.4: Summary of inputs, outputs and intrinsic excitatory connections of a generic, nonprimary visual area of primate cerebral cortex. Picture taken from *Shipp* (2007).

Extrinsic connections and projections above describe a general pattern in the inter-regional connectivity. However, there is some variability in these connections that depend on the regions involved and specially the so-called distance rule: regions that are closer to each other typically have denser connections that involve more layers. If the regions are further apart, connections are more localized to single layers and go from one anatomical layer to another (*Wang and Kennedy*, 2016).

In addition, apart from the direct connections described above, it is worth mentioning that there can be also an indirect pathway from one cortical region to another. For instance, from V1 to V2, there is the direct input from Layer III in V1 to Layer IV in V2, and the indirect pathway via Layer V in V1 to the pulvinar nucleus, to the natural geniculate nucleus and then to Layer III in V2.

Intrinsic connections:
Intrinsic connections are connections within a cortical region.

- Excitatory intrinsic connections: Intrinsic excitatory connections are more numerous than extrinsic excitatory connections and hence they are of great importance in functional inter-and intra-laminar integration. As mentioned earlier, pyramidal cells are the main type of excitatory neurons. Their dendritic terminations can expand several layers (see Figure 3.3), but it is considered that a neuron 'belongs to' the layer in which its soma is (*Shipp*, 2007). Excitatory connections within a region show a large degree of heterogeneity. Lateral connection can extend 2-3 mm from the parent soma, even up to 8 mm in layer VI in V1. In addition, collateral connections are not confined to a layer and can send branches to other (not adjacent) layers within the region.

- Inhibitory intrinsic connections: Inhibitory neurons make up 20% of the total number of neurons in an area. This is a very heterogeneous group of neurons, which suggest that they may be highly specific. Together with the external connections and internal microcircuitry they may enhance plasticity and flexibility of response (*Rockland*, 2017).

White matter neurons:
These are a group of excitatory and inhibitory neurons that can be found in superficial and deep white matter. These neurons are not densely distributed and are unlikely to be visible in MRI, but they are believed to interact with neurons in GM, and some of them are involved in neurovascular coupling (*Rockland*, 2017).

3.1.6   Columns in the brain

While the laminar organization of the cortex is observable with staining techniques across the whole cortex, cortical columns relate to the functional organization and are not distinguishable ex-vivo. They were first discovered in the somatosensory cortex (*Mountcastle*, 1957) and Hubel and Wiesel received the Nobel Prize in Physiology in 1981 for discovering their presence in the visual cortex (*Hubel and Wiesel*, 1959). Since then, analogous to orientation or colour sensitive columns in the visual cortex, frequency sensitive columns have been identified in the auditory cortex. The existence of the columns in the visual cortex is not pervasive among all mammals. Primates and cats have orientation sensitive columns, while rodents don't; but they can all decode orientation. This raises the question if columns are really required for visual processing. Columnar organisation is believed to be ubiquitous over grey matter. The fact that so far columns have only been identified in the somatosensory regions does not imply they don't exist in others, but rather reflects the difficulty of having a proper paradigm that would allow their identification.

3.2   Cortical vasculature

In comparison to the rest of the organs in the human body, the metabolic demands of the brain are remarkably high: even if it only makes up for 2% of the body weight, it accounts for 20% of the total energy use (*Shulman and Rothman*, 2005). As brain tissue lacks a means of storing energy, such as fat reserves or muscle, it requires a continuous blood supply. This section focuses in the vascular architecture in the neo-cortex, which is key to understand the laminar specificity of cortical activation as measured in fMRI.
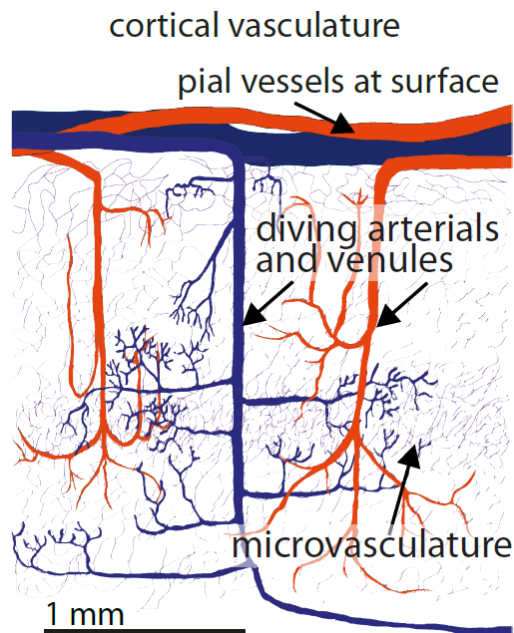
Figure 3.5: Schematic of cortical vasculature. Pial arteries and veins are located on the cortex. Diving arteries and venules branch out perpendicularly into the grey matter. These in turn branch out into arterioles and venules that split up into smaller vessels until capillaries are reached. Blood flows unidirectionally from the pial arteries into the diving arteries, arterioles, capillaries, venules, emerging veins to the pial veins. Figure modified from *Huber* (2014).

As described in *Duvernoy et al.* (1981) and shown in Figure 3.5, blood is supplied to the brain regions in the neo-cortex through pial arteries ($\varnothing$=40-280 µm), located on the cortical surface. Diving arteries ($\varnothing$=10-75 µm) branch out from the pial vessels into the cortex and run perpendicular to the cortical surface. Arterioles are smaller arteries that branch out, often perpendicularly, from diving arteries. Arterioles split repeatedly into smaller vessels until they reach the capillaries, which are on average 5 µm in diameter. The arterioles that are closer to diving arteries are called lower order branching arterioles, whereas those that are closer to capillaries are higher order branching arterioles. Blood flows from the capillaries to venules following a mirrored architecture to the one described in the arterial part: after a few combining (instead of splitting) steps, venules flow into larger intracortical veins ($\varnothing$=20-120 µm) that run perpendicular to the cortical surface. These veins have a larger diameter than their arterial counterparts. Intracortical veins drain blood from the cortex into large pial veins of ($\varnothing$=130-380 µm), located on the pial surface, which drain into the sinuses and then back to the heart.

Blood vessels smaller than 20 µm in diameter are typically referred to as microvascular vessels and those with a larger diameter, macrovascular vessels. Macrovasculature is composed of laminar venules and arterioles and diving arteries and
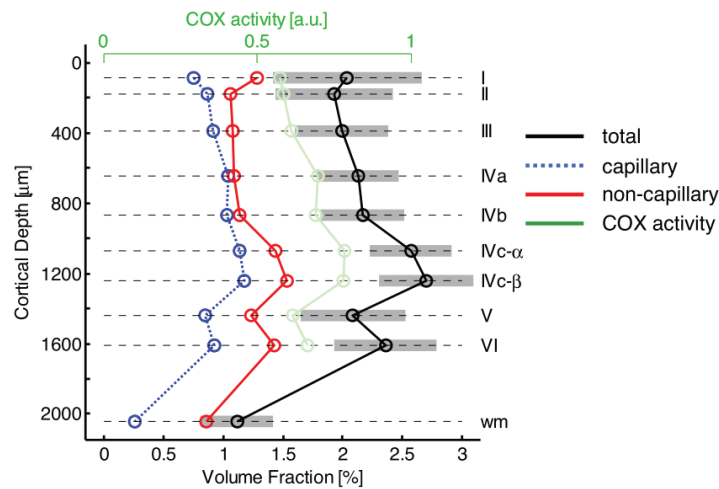
Figure 3.6: Lamina- and area-specific vascular density in visual area V1 of macaque monkey. Quantitative values of microvascular system across the cortical layers and cortical depths (μm from cortical surface) in the striate cortex. The black traces show the overall mean density (± standard deviation indicated with grey shaded bar). The blue trace shows the values for the capillaries and the red for the noncapillary vessels. The green trace shows the COX activity in arbitrary units. Modified from *Weber et al.* (2008).

emerging veins that run perpendicular to the cortical surface. The macrovascular vessel density increases with decreasing cortical depth as all diving arteries and emerging veins, regardless of the cortical depth they reach, stem from or lead to the pial surface.

Microvasculature is composed of capillaries and small laminar arterioles and venules. The microvascular volume profile across the cortex is rather flat compared to the macrovascular profile. The microvascular density shows a maximum towards the middle of the cortex (see Figure 3.6). This raises the question if the hemodynamic measures used for functional MRI reflect more the local vascular environment than the neural activity. As shown in Figure 3.6, cox staining has shown that the microvascular distribution across the cortex tightly follows the level of metabolic activity in the resting condition across the cortex and that it does not correlate with the synaptic density (*Weber et al.*, 2008). This indicates that hemodynamic measures that originate from microvasculature will reflect metabolic demands of the tissue and that they are therefore a good surrogate of neuronal activity.

fMRI literature reflected for many years the understanding that the substantial part of glucose and O_2 supply to the brain cells takes place in the capillaries. According to this, the oxygenation of the arteriolar side is fairly constant and close to 100%, oxygen is delivered to tissue in the capillaries and the oxygenation is rather constant in the venous side, around 60% at rest. The results shown in *Sakadžić et al.*

(2014) challenge this oxygenation distribution across the vascular tree based on *in-vivo* measurements of the mouse brain using two photon microscopy. According to these, there is an oxygenation drop from 95% in the first branching order arterioles to 75% in the precapillary arterioles. Hence, they argued that 50% of the O_2 delivery to tissue in the resting condition takes place in pre-capillary arterioles. Upon activation, however, most of the O_2 delivery to supply the increased demand takes place in the capillaries. Another surprising finding was that blood oxygenation was higher for lower order branching veins (those close to intracortical veins), according to the authors, possibly reflecting recaptured oxygen surplus in the tissue.

3.3 Neurovascular coupling and vascular response to activation

Neurovascular coupling refers to the relationship between neural activation and the changes in vasculature that follow. All cells need constant supply of energy to keep their homeostasis. Excitable cells, such as the brain cells, are said to be activated when the amount of information, signal from adjacent neurons, is larger than the baseline condition, regardless if as a result an action potential is released.

In the active state the metabolic needs of the cell are higher than in the resting state and the cerebral metabolic rate of glucose and oxygen, CMRGlc and $CMRO_2$, respectively, increase. In order to cover this increased demand, neurons release vasodilators, metabolites that act on the surrounding vasculature dilating them and increasing the cerebral blood volume (CBV) in the surroundings of the activation site. The increase in the vascular cross section decreases the vascular resistance, resulting in an increase in cerebral blood flow (CBF) to the region. As a consequence, the available oxygen and glucose, the two main components required by cells to cover their energy demand, increases. In fact, flow increases more than what is strictly required to cover the increased oxygen consumption. This leads to a local increase in blood oxygenation because there is more oxygen available.

Blood flow is regulated via two independent pathways. One of them is mediated by astrocytes, which have terminations on both the nerve cells and the endothelial muscles of the arterioles. Vasoactive metabolites are hence directly transported to the arteriolar surface leading to a local dilation of the vessel wall. This dilation propagates over the endothelial muscle to arteries upstream and blood flow to the region is increased. The second pathway is the one regulated via the pericytes. The vessel wall of the capillaries is formed by a sheet of single endothelial cells, not contractile muscle. Therefore, they cannot actively change their cross section to regulate blood flow. However, *Hall et al.* (2014) showed *in-vivo* that pericytes,

hook shaped cells surrounding capillaries, contract and dilate regulating capillary cross section, and hence blood flow. It is not clear yet which of the two pathways is the dominant mechanism for regulating blood flow.

The venous endothelium is not composed of contractile muscle, so they lack the ability to actively dilate or contract. There is a consensus that small veins of 10-20 μm of diameter change their volume passively following changes in blood flow. The response of veins larger than 20 μm in diameter is more heterogeneous and depends on the location, pial or parenchyma, and the stimulus duration. Veins within the parenchyma for stimuli shorter than 20 seconds do not dilate (*Hillman et al.*, 2007; *Kim et al.*, 2007) whereas for stimuli longer than 20 seconds venous dilation was observed (*Drew et al.*, 2011; *Huo et al.*, 2015; *Kim and Kim*, 2011).

The spatial specificity of blood regulation and the hemodynamic response will determine the spatial specificity achievable with fMRI. Optical imaging and 2-photon microscopy studies show evidence that blood flow regulation in response to sensory stimulation occurs at the level of capillaries and pre-capillary arterioles (*Goense et al.*, 2016) and that the capillary response is confined to a specific layer (*Tian et al.*, 2010), with an estimated spatial scale of less than 0.2 mm in rats (*Vazquez et al.*, 2013). This is in line with laminar CBV measurements carried performed in mice that show that the vascular changes evoked by the synaptic activity were laminar specific and that the spatial resolution limit might be 100-200 μm (*Poplawsky et al.*, 2017b, 2015).

Chapter 4

Biophysics of fMRI

There are a number of techniques available for measuring brain function, but this section focuses on the biophysical substrate of the blood oxygenation level dependent (BOLD) signal, the most widely used technique to measure brain function. After a general overview of measures of cerebral activity, the temporal dynamics and contrast mechanisms of BOLD are described. These are necessary to understand the spatial specificity and sensitivity of the BOLD signal. After that, noise distribution and functional contrast in BOLD-based fMRI are discussed, factors that are key for a successful design and interpretation of the functional scans. Lastly, the sequences available for BOLD-fMRI are briefly discussed, with the focus on the EPI sequence.

4.1   Measures of cerebral activity

As seen in the previous section, neuronal activity is accompanied by changes in ion fluxes, in glucose and oxygen metabolism and in the local blood flow and volume. Measurement techniques sensitive to any of these changes can be regarded as a direct or indirect measure of neuronal activity.

Electroencephalography (EEG) and magnetoencephalography (MEG) are techniques that measure changes in the electrical and magnetic field that are induced by electric currents across the neural membrane. These techniques have an excellent temporal resolution and can sample electrical activity in the brain, including ionic currents and and spiking activity, without aliasing. The spatial specificity and localization are in the range of centimetres and the measurements are confined to superficial parts of the cortex.

Positron Emission Tomography (PET) and Single Photon Emission Computer Tomography (SPECT) are neuroimaging techniques that require the injection of radiotracers, radioactive molecules, in order to measure brain activity. In PET, the most common radiotracer used is 18-FDG, which is an altered glucose molecule. This radiotracer is metabolized by cells and hence metabolic activity can be quantified and localized. In SPECT, changes in blood flow can be measured as the radiotracer Technicium is diluted in blood and the measurements are blood flow sensitive. These techniques have a good sensitivity to activation and the signal measured is quantitative (number of occurrences). The temporal resolution is in the order of minutes and modern scanners can achieve 3-6 mm voxel sizes. A disadvantage of these methods is that they are invasive, include ionizing radiation and that some radiotracers might not be available depending on the proximity of a cyclotron facility.

Brain activity can also be measured by MRI. There have been some early attempts on phantoms to measure changes in local magnetic field induced by changes in ionic currents (*Balasubramanian et al.*, 2016; *Truong et al.*, 2008), but their validity *in-vivo* has not been shown yet. The functional MRI techniques that have taken off with different degrees of success are related to the hemodynamic changes that follow neuronal activation that modify the MRI signal, i.e. flow changes, volume changes, changes in oxygen consumption and a technique that is sensitive to the three physiological changes just mentioned, Blood Oxygenation Level Dependent (BOLD).

The BOLD signal is not a quantitative measure of neuronal or vascular state. Yet, since the discovery that the MR signal was sensitive to this effect in the early 90's (*Ogawa et al.*, 1990), it has been the most widely used method in functional MRI due to its higher sensitivity to neuronal activation and simplicity to measure (*Huber et al.*, 2018). The seminal work by Logothetis showed that the BOLD response correlated well with the local field potentials, especially with the γ-frequency band (*Logothetis et al.*, 2001), which is a measure of the synaptic activity in a region. This indicates that the BOLD response is a valid surrogate of local neuronal activity.

4.2   The BOLD response

The magnetic susceptibility of blood depends linearly on its (de)oxygenation level because oxy-hemoglobin contains diamagnetic iron while iron in deoxyhemoglobin is paramagnetic. The perturbation of the magnetic field induced by blood vessels increases with increasing deoxyhemoglobin content, which results in a faster loss of spin coherence. Thus, the transversal relaxation time of a region
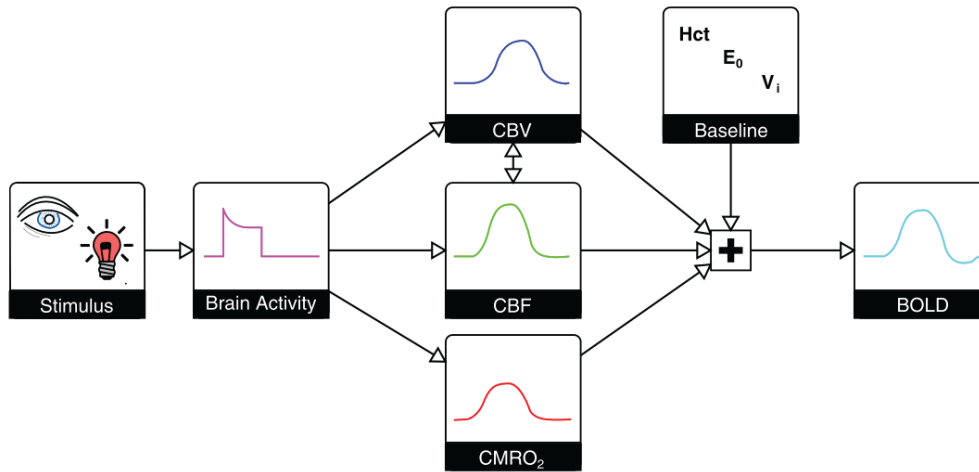
Figure 4.1: The sensory stimulus elicits a neuronal activity that leads to increases in CBV, CBF and $CMRO_2$. Increases in CBV and $CMRO_2$ lead to a decrease in the BOLD signal, but as the increase in CBF is larger, there is an increase in the BOLD signal. The magnitude of the signal depends on the baseline volume, hematocrit and oxygen extraction fraction. Figure taken from *Blockley et al.* (2013).

is blood oxygenation level dependent (BOLD). Consequently, changes in BOLD signal can be measured by T_2 or T_2^*-weighted MR sequences.

The change in the blood oxygenation level in a region depends on the interplay between changes in neuronal metabolic rate of oxygen consumption ($CMRO_2$); changes in cerebral blood volume (CBV) and cerebral blood flow (CBF), as seen in Figure 4.1. Changes in $CMRO_2$ and CBV will lead to a decrease in the measured MR signal, as if everything else is kept constant, the amount of deoxyhemoglobin in the region increases if more O_2 is consumed or if there is more deoxyhemoglobin in the voxel due to a larger CBV. However, as explained earlier when discussing functional hyperemia, CBF increases more than what is strictly required to cover the increased metabolic demands. This leads to an increase in the amount of oxyhemoglobin in the region, and hence to a net positive signal change. Baseline factors, such as, hematocrit, Hct, (volume fraction of red blood cells in blood), the oxygen extraction fraction at rest, E_0, and the resting blood volume in the region influence the magnitude of the BOLD signal.

Vasoactive metabolites change the cross section of surrounding vasculature, leading to a flow increase. Hence, it is intuitive that CBV and CBF changes are coupled. The coupling of these two measures is given by $\frac{\Delta CBF}{CBF_0} = \left(\frac{\Delta CBV}{CBV_0}\right)^\alpha$, where α is the Grubb constant. The seminal study performed in PET that established this relationship came up with $\alpha = 0.38$ (*Grubb et al.*, 1974). More recent work has suggested that BOLD-based fMRI measurements should use a value of $\alpha=0.23$ (*Chen and Pike*, 2009). Contrary to the PET measurements, in BOLD-based fMRI

venous contribution is larger than the arterial contribution, which dilate less than their arterial counterparts. Hence, the need to adjust the coupling parameter.

$CMRO_2$ and CBF/CBV changes are believed to be governed by different pathways and are uncoupled. The ratio between oxygen metabolic changes and flow changes is known as the neurovascular coupling constant $\left(n = \frac{\Delta CBF}{\Delta CMRO_2}\right)$ and it is between 2-3 in the healthy brain (*Griffeth et al.*, 2014). The neurovascular coupling can be altered in disease, but also if baseline conditions are modulated, for example by attention or by caffeine intake as it reduces resting CBF (*Buxton et al.*, 2014).

In summary, baseline conditions and hemodynamic changes following neuronal activation affect the magnitude of the BOLD signal, hence it is not a quantitative measure of neuronal activity.

4.2.1   The hemodynamic response function

The BOLD response to neural activation after a stimulus event follows a characteristic evolution over time known as the Hemodynamic Response Function (see Figure 4.2). The hemodynamic response evolves in the order of seconds, whereas the underlying neuronal changes happen in the order of milliseconds. Therefore, the measured MR signal is an averaged and temporally blurred response to the underlying neuronal activation (*Harel et al.*, 2006b).

Around 3 seconds after the stimulus onset, an initial-dip has been observed. This is a small decrease in signal that is believed to be associated with an increased O_2 consumption, before the CBF increase has taken place. As such, mapping this early BOLD decrease would be spatially specific as most of the O_2 extraction happens in the capillaries. However, the initial dip has been consistently reported in the optical imaging literature, but its presence in fMRI is more elusive (*Buxton*, 2001; *Hu and Yacoub*, 2012; *Uludağ*, 2010).

6-8 seconds after stimulus onset the lagged main response occurs. In this phase, there is still an increased $CMRO_2$ with respect to baseline, but the local vasculature has expanded increasing the CBV and CBF. As explained in the previous section, CBF is the dominant physiological change between the three, which leads to a large positive response.

Lastly, the post-stimulus undershoot can be seen 10-12 seconds after stimulus onset and it can take as long as 20 seconds until signal returns back to baseline. In the early days of fMRI, it was suspected that the post-stimulus undershoot was due to a period of increased CBV because of delayed vascular compliance, when $CMRO_2$ had already returned to baseline (*Buxton et al.*, 1998). However,
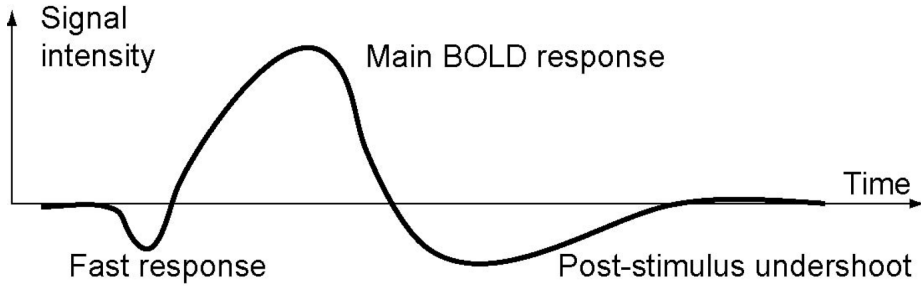
Figure 4.2: Temporal evolution of the BOLD response to an event-like stimulus, known as the hemodynamic response function (HRF). The hemodynamic response function describes the response to an event-like stimulus. If long stimuli of several seconds or short stimuli spaced more than 2 seconds apart are used, the system behaves like a Linear Time Invariant (LTI) System and the BOLD response obtained will be the stimulus duration convolved with the HRF just described. In these cases, the obtained response has a lengthened positive BOLD response and a better SNR than the response to event-like stimuli (*Goebel*, 2015).

evidence since has shown that there is an increased $CMRO_2$ or, at least, a smaller reduction in $CMRO_2$ than in CBF during this period, and that it correlates with electrophysiological activity (*Mullinger et al.*, 2013), leading to the conclusion that the post-stimulus undershoot is neuronal in origin.

The BOLD response described is sometimes referred to as the positive BOLD response, because the main response is positive. This response is the most common response following excitatory neuronal activity. However, the main BOLD response can also be negative, followed by a post-stimulus 'overshoot'. The mechanisms behind the negative BOLD response are less well understood but there is evidence to think that it is related to neuronal inhibition (*Goense et al.*, 2016).

4.3 BOLD Contrast Mechanisms

The spatial specificity and the sensitivity to neuronal activation of the measured BOLD signal are determined by the contribution from the tissue and vascular compartments, which vary depending on the acquisition sequence and parameters used.

The field perturbation induced by deoxyhemoglobin has an effect within and beyond the blood vessel itself, i.e. the magnetic field is perturbed in the intravascular and extravascular compartments. The total signal measured in the voxel will be a volume weighted average of the extravascular and intravascular contribution as shown in Equation 4.1 (*Van Zijl et al.*, 1998):

$$S = (1 - CBV) \cdot S_{ex} + \sum_i \Phi_i \cdot CBV_i \cdot S_{in_i} \qquad (4.1)$$

where *CBV* is the cerebro vascular volume in a voxel and S_{ex} and S_{in} represent the signal dephasing from the intravascular and extravascular compartments, respectively. The index *i* refers to the specific vascular compartment (i.e. large veins, venules, capillaries, arterioles, arteries) and Φ refers to the proton exchange rate between the vascular compartments and the surrounding tissue, mainly freely diffusing water molecules. For typically used echo times of tens of milliseconds, the proton exchange through vessel walls is considered negligible and this number is often considered to be 1.

The extravascular perturbation around a vessel can be approximated as the field perturbation created by an infinite cylinder (*Ogawa et al.*, 1993), which is given by:

$$\Delta\omega = 2\pi\omega_0 \, \Delta X \, (1 - Y) \, sin^2\theta \left(\frac{a}{r}\right)^2 \, cos2\phi \qquad (4.2)$$

where ω_0 is the larmor frequency, ΔX is the susceptibility difference between tissue and fully oxygenated blood (0.24 ppm), Y is the oxygenation of blood (i.e. the ratio of oxyhemoglobin to total hemoglobin), a is the radius of the vessel, θ is the angle between the vessel and B_0 and Φ is the angle in the plane perpendicular to the vessel orientation. This equation shows that the field perturbation around a vessel increases linearly with the amount of deoxyhemoglobin and that it decreases quadratically with the distance from the centre of the vessel. Equation 4.2 generates the dipolar field depicted in Figure 4.3.

Water molecules diffuse in tissue with an expected diffusion path $< s > = \sqrt{6Dt}$, where D is the diffusion constant ($D \sim 0.8 \ \mu m^2/ms$ in GM) and t is the diffusion time. The signal attenuation experienced by protons diffusing around blood vessels, will depend on the vessel size through the following mechanisms:

- Static dephasing: when the radius of the vessel is much larger than the expected diffusion path during the echo time, spins can be considered to be confined to a region with a given magnetic field, spins precess at a Larmor frequency that is position dependent (Figure 4.3). The loss of coherence between spins as magnetisation evolves at different locations leads to signal attenuation.

- Dynamic averaging: if the vessel radius is in the same order of magnitude as the diffusion path, spins randomly diffuse through a range of regions with different magnetic field between excitation and echo time (Figure 4.3). The dephasing experienced is not position dependent. As magnetisation evolves, spins lose coherence.

It is considered that for typical echo times used in MRI spins diffusing around vessels with a radius larger than 20 μm will be in the static dephasing regime and
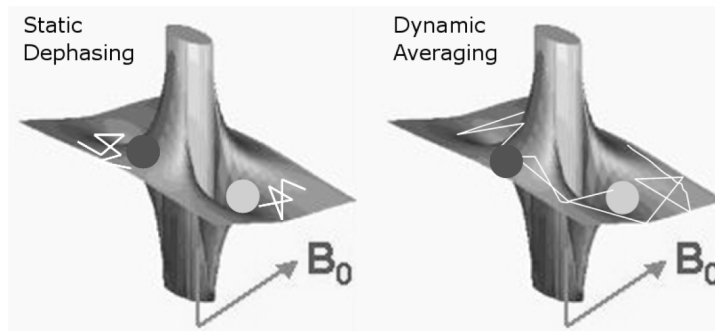
Figure 4.3: The distortion of the field about an infinitely long cylinder containing paramagnetic material is shown by means of distortion to the plane perpendicular to the axis of the vessel. The grey shaded circles represent diffusing spins.

those diffusing around vessels smaller than 20 μm, mostly capillaries, will diphase in the dynamic dephasing regime.

$$\Delta\omega = 2\pi\omega_0 \, \Delta X \, (1 - Y) \, (3cos2\theta - 1)/3 \qquad (4.3)$$

The equation is given in polar coordinates and the parameters have been explained after Equation 4.2. Equation 4.3 shows that the frequency within a vessel depends linearly on the amount of deoxyhemoglobin. Interestingly, the field perturbation will be nulled when the vessel has an orientation equal to the magic angle with respect to the main magnetic field. However, this fact is mostly anecdotal as in general, a voxel will contain many vessels, capillaries and veins, with a range of orientations with respect to the main magnetic field.

Again, a distinction between an intravascular contribution of the BOLD signal in the static and dynamic dephasing regime can be made:

- Static dephasing: A voxel contains various vessels with different baseline oxygenation levels and orientations with respect to B_0, which leads to different frequency offsets across the voxel (Equation 4.3) and to a loss of phase coherence. Alternatively, even if the voxel contained a single vessel, the fact that blood and tissue have different susceptibility values (and therefore Larmor frequencies) will result in a beating effect and an oscillation in the signal intensity as a function of TE (*Norris*, 2006).

- Dynamic averaging: There are two competing theories on the nature of the intravascular dynamic averaging that are difficult to prove. The first one describes a similar mechanism as the dynamic averaging around small vessels, but in this case, protons would be diffusing around deoxygenated hemoglobin molecules. The mechanism of the second theory giving rise to an intravascular dynamic averaging effect would be that of rapid proton exchange between regions with different magnetic susceptibility.

	Extravascular	**Intravascular**
Static dephasing	Spins have a Larmor frequency that is position dependent, which is the case when the vessel radius is considerably larger than the diffusion path. As magnetisation evolves, spins lose coherence.	Different offset frequencies between blood in vessels with different orientation, which leads to loss of phase coherence.
Dynamic averaging	Each spin experiences a range of susceptibility values during the echo time.	i) Water molecules diffusing around hemoglobin or ii) Rapid exchange of protons between sites with different magnetic susceptibility.

Table 4.1: Classification of BOLD contrast mechanisms.

4.4   Sensitivity and spatial specificity of the BOLD signal

The 180° pulse in spin-echo sequences will refocus the static dephasing component. Consequently, spin echo sequences are insensitive to the intravascular BOLD contribution arising from the different susceptibility of blood and tissue and to the extravascular contribution from large vessels (see Table 4.1). Therefore, compared to the use of gradient echo or T_2^*-weighted sequences, the sensitivity to detect activation is lower when spin echo or T_2-weighted sequences are used, but the spatial specificity is higher because extravascular dephasing around large veins distant to the site of activation will no longer contribute to the signal measured. At low fields the intravascular contribution is considerable, so the increased spatial specificity of spin echo becomes relevant at high fields, when the intravascular contribution to the BOLD signal is very small or neglectable.

The spatial specificity of SE-BOLD increases with B_0 because the T_2 of blood decreases and the intravascular contribution fades away; the dominating contrast mechanism is the extravascular dynamic contribution around microvasculature. Figure 4.4 shows that the microvascular contribution (black line) increases with increasing B_0, specially for SE. For SE, the macrovascular contribution (pink line) decreases with B_0 from 3 T onwards as the T_2 of blood fades away diminishing the intravascular contribution. For GE, macrovascular contribution increases steadily and is larger than the microvascular contribution at all fields.
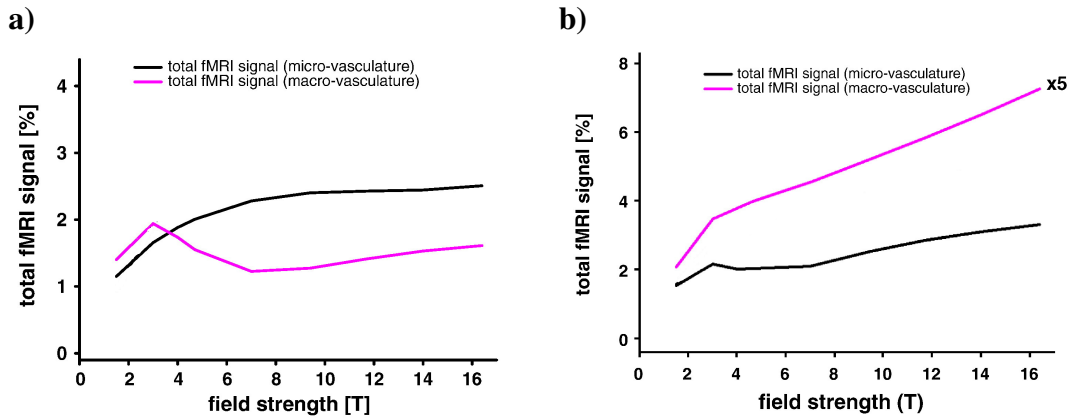
Figure 4.4: Microvascular and macrovascular contributions to BOLD signal changes across fields at the corresponding TE=$T_2^{(*)}$ per field for **a)** SE- and **b)** GE-BOLD fMRI. The curves are based on the simulation of a cortical voxel with a realistic vascular distribution. Graphs modified from *Uludağ et al.* (2009).

Nonetheless, macrovasculature in the voxel simulated in *Uludağ et al.* (2009) consisted in a large vein ($\varnothing = 200$ μm), oriented perpendicularly to B_0, which represents the worst case scenario in terms of microvascular to macrovascular contribution.

4.5 Noise and functional contrast in BOLD fMRI

4.5.1 Noise in fMRI

Any nuisance components to the temporal fluctuations that are not the result of neuronal activity changes induced by the stimulus are considered noise sources in task-based fMRI.

One of these sources is the thermal noise derived from random processes, such as the ionic current fluctuations in the electrically lossy body and losses in the RF detector and amplifiers. In a well-designed setting, losses in the body contribute over 90% to the noise at the input of the preamplifier (*Wald et al.*, 2015). Thermal noise is statistically independent, temporarily and spatially uncorrelated. As it is the result of different noise sources, following the central limit theorem, the temporal fluctuations of a voxel in a phantom follow a Gaussian distribution. The amount of thermal noise in a voxel increases with the square root of the acquisition bandwidth and the square root of the image acceleration rate. It is independent of the magnitude of the signal in a voxel and is therefore called additive noise. It can be measured by acquiring an image with a 0° RF pulse.

The time-course fluctuations of living samples are affected by a further source of non-thermal nuisance component. As it only appears in living samples, it is called physiological noise. This is a multiplicative noise that modulates the signal and is proportional to the voxel intensity. In the absence of signal, there is no physiological noise.

Based on its origin and behaviour, physiological noise is classified into two main groups (*Kruger and Glover*, 2001):

- BOLD-like noise: This is the modulation arising from blood flow and metabolism associated with resting state or spontaneous activity. In fact, this 'noise' is the signal of interest when performing resting state fMRI.

- Non-BOLD like noise: these are all the signal changes not related to neuronal activity, such as hemodynamic and B_0 changes associated with the cardiac and respiratory cycle and their changes, vaso-motion, CSF flow and rigid and non-rigid tissue motion. The signal modulation of all these confounds is complex, but not random in origin.

The physiological noise sources modulate signal intensity. An important difference between the two is that, while Non-BOLD like sources are only proportional to the signal magnitude, BOLD-like sources are proportional to the signal magnitude and echo time. This is important for understanding the TE-dependence of the functional contrast to noise ratio under different noise regimes (see next section).

Following the noise model in *Kruger and Glover* (2001), the total signal fluctuation of the voxel time-course is given by:

$$\sigma_t^2 = \sigma_0^2 + \sigma_B^2 + \sigma_{NB}^2 \tag{4.4}$$

where σ_t is the total fluctuation over time, σ_0 is the thermal noise, σ_B is the BOLD-like noise and σ_{NB} is the non-BOLD-like noise. The last two terms are the physiological noise level in the signal. Equation 4.4 assumes that physiological noise follows a Gaussian distribution, which is not the case but has proven to be a valid approximation (*Wald and Polimeni*, 2017).

4.5.2   Variation of noise distribution with varying magnetic field strength

The magnitude of the MR signal increases with B_0^2 for fully relaxed acquisitions, provided that comparable receiver coils and flip angle homogeneity are used. Thermal noise increases with B_0, due to losses related to signal dissipation in the body that are proportional to the frequency. Hence, in theory, image SNR, also referred to as SNR$_0$, will increase linearly with B_0 (*Gati et al.*, 1997; *Vaughan*
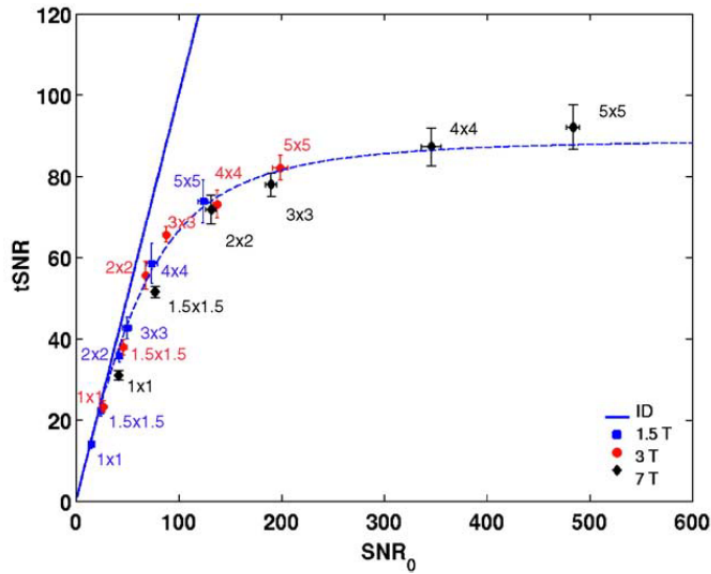
Figure 4.5: Time-course SNR (tSNR) as a function of image SNR (SNR$_0$) for gradient echo EPI acquired using volume coils at 1.5 T, 3 T and 7 T and parameters optimized for each field strength. Image SNR was varied by changing the in-plane resolution (slice thickness was 3 mm in all cases). The straight line corresponds to a unit slope and the dotted line to the analytical function that relates tSNR and SNR$_0$ fitted to the data. Figure taken from *Triantafyllou et al.* (2005).

et al., 2001). In standard experimental conditions SNR increases rather with $B_0^{1.65}$ (*Pohmann et al.*, 2016).

The relevant noise metric in functional MRI is the temporal SNR, tSNR. For a time-series, this is given by the average signal over the time-course divided by its temporal standard deviation ($tSNR = \frac{\bar{S}}{\sigma_t}$). It is a measure of the smallest signal change that can statistically be distinguished.

If everything else is kept constant, SNR$_0$ is proportional to the voxel volume, as signal is linearly proportional to the voxel volume and thermal noise is unchanged. Figure 4.5 shows that at high enough SNR$_0$, the tSNR is completely limited by physiological noise. This is, at a given field strength, increasing the voxels size will increase SNR$_0$, but not tSNR. Higher field strengths always improve tSNR, but the improvement is marginal for large voxels.

To date, functional MRI scans are acquired using head coils with several channels (e.g. 12 or 32 channels). When multi-channel reception is used, which increases the obtainable SNR, the physiological noise dominated regime is obtained for smaller voxel sizes than those shown in Figure 4.5 (*Triantafyllou et al.*, 2011).

4.5.3   Functional contrast

The functional contrast to noise ratio, *CNR*, is a measure of the signal changes induced by the activity of interest with respect to the signal fluctuations at rest:

$$CNR \; = \; \frac{\Delta S}{\sigma_t} \; = \; \frac{\Delta S}{\overline{S}} tSNR \tag{4.5}$$

where ΔS are the signal changes in the voxel between activation and rest, σ_t is the standard deviation over time of the image intensity of the voxel in the resting condition, $\overline{S}$ is the average over time of $S \; = \; S_0 e^{-TE/T_2^{(*)}}$ and $tSNR$ is the temporal noise as defined in the previous section.

The parameter optimization of the acquisition sequence will be targeted at maximizing the CNR. The obvious parameter set to maximize the contrast is the TE. A simple differentiation of Equation 4.5 with respect to TE shows that the optimum TE to acquire the signal is $\text{TE}=T_2^{(*)}$ and hence this is a TE often used in functional acquisition.

Nonetheless, this approach assumes that the noise is TE-independent. This approximation is valid when the dominant source of noise in an image is thermal noise, but not when physiological noise dominates. The latter case is not a rare case anymore, as hardware improvements have made modern fMRI acquisitions more physiological noise dominated than older acquisitions (*Triantafyllou et al.*, 2011, 2016). In these cases, if non-BOLD like noise dominates, the optimum TE for maximum CNR will be longer. If BOLD-like noise dominates, the CNR curve will be flatter around the optimum TE predicted for the case in which only thermal noise is present (*Van de Moortele et al.*, 2008; *Wald et al.*, 2015).

4.5.4   MR sequences used for BOLD-based fMRI

Sequences sensitive to changes in $T_2^{(*)}$ (SE-RARE/HASTE, GE-FLASH, EPI, non-balanced SSFP) or frequency shifts induced by differences in the magnetic environment between rest and activation (balanced SSFP) can be used for fMRI (*Norris*, 2015).

The vast majority of functional MRI acquisitions today use an EPI image encoding scheme because it allows the acquisition of one volume in the range of 1-3 seconds at most static fields. Thanks to receiver coils with multiple channels, it is possible to accelerate the image acquisition with tolerable penalties in SNR and achieve an image resolution of 2-4 millimetres.

In 3D-EPI, due to the volumetric acquisition, spin history effects (i.e. residual magnetisation effects of previous excitations due to through-plane motion of the spins during the scan) are almost entirely eliminated and slice time correction is not necessary. 3D EPI can be accelerated in both phase encoding directions and similar acceleration factors as in simultaneous multi slice 2D-EPI can be achieved without SAR or peak voltage considerations (*Marques et al.*, 2017). The main drawback of 3D-EPI is that it suffers from the combined effect of physiological noise and motion artefacts during volume acquisition. The correction of physiological artefacts poses a smaller problem in 2D-EPI, where slices have been acquired at different phases of the respiratory and cardiac cycles. In this case, each slice can be phase locked to the effect of the physiological BOLD fluctuations and as a result this effect can be removed more efficiently. If very thin slices are excited, 2D-EPI might run into SAR or gradient problems as very large bandwidths might be required to obtain sufficiently rectangular slices.

In this thesis, the less common GE-FLASH and non-balanced SSFP sequences have been used to measure high-resolution BOLD-based functional MRI, sacrificing temporal resolution. The motivation behind using GE-FLASH was to sample the T_2^* decay using a multi-echo FLASH acquisition, that would be distortion free to make a comparison of signal features across field strengths. The non-balanced SSFP was used to investigate if this were a proper approach to obtain T_2-like activation profiles.

Chapter 5

Layer specific fMRI

As described in Chapter 3, layers within a region have a distinct role in constraining the feedforward and feedback pathways between regions. Typical fMRI acquisitions with voxel sizes of 2^3 to 3^3 mm^3 cannot effectively resolve layer-dependent signal differences contributing to the BOLD signal; they require model based approaches, such as PPI or DCM (*Friston et al.*, 2003, 1997), to infer hierarchical relationship between regions. High resolution, layer specific measurements form the basis of a simple approach to this difficulty. With sufficient resolution, it is possible to compare the signal observed at different cortical depths, directly measuring the forward and backpropagating contributions to the overall signal.

In this section, a historical overview of laminar fMRI is given first. This presents mainly results from animal studies, as studies in humans are discussed in the scientific chapters in this thesis. Then, a brief comparison of the currently available methods for laminar fMRI in humans is provided, followed by the introduction of the interlaminar signal leakage problem in GE-BOLD. Thereafter, the requirements for laminar fMRI are presented.

5.1 Overview of laminar fMRI

5.1.1 Brief history of laminar fMRI

Early measurements of laminar fMRI were performed in smaller animals, such as rodents. Small animals are anesthetized during the scan; hence head motion is not an issue, which enables longer acquisitions. That is why, in combination with high static magnetic fields and local coils, high resolution and high sensitivity could be achieved. As the cortex of these animals is not strongly convoluted, it

was possible to integrate signal at a given cortical depth over a relatively small patch of cortex to obtain laminar activation profiles with good resolution and little risk of partial volume effects.

Much of this early work focused on the origin of the layer-dependent signal, combining fMRI with invasive measures of neuronal activity to study its neurovascular properties. For example, it was shown that there is a good degree of co-localisation of calcium-dependent synaptic activity and CBF (*Duong et al.*, 2000) and that CBV is better localized than BOLD, as shown by Fos expression – a marker used to trace neuronal metabolic activity (*Lu et al.*, 2004).

Many of the studies that followed compared various fMRI methods and showed that CBV is better localized to grey matter than GE-BOLD (*Harel et al.*, 2006a), that the spatial localization of CBF is close to that of CBV (*Jin and Kim*, 2008a; *Zappe et al.*, 2008), and that SE-bold shows a greater similarity to CBV than GE-BOLD (*Goense and Logothetis*, 2006; *Harel et al.*, 2006a). More recent studies measured the laminar specificity of the vascular response and showed that CBV peak was specific to the layer of evoked synaptic activity (*Poplawsky et al.*, 2015) and that the spatial resolution limit might be 100-200 µm, sufficient for examining sublaminar circuits (*Poplawsky et al.*, 2017a).

Regarding timing differences between layers, it was found that the earlier activation measured by GE-BOLD happens towards the middle of the cortex in the somatosensory cortex, coinciding with the thalamic input (*Silva and Koretsky*, 2002; *Yu et al.*, 2014). Activation then spreads towards macrovasculature 1.2 seconds after stimulus onset and penetrating venules dominate the peak response even at lower layers (*Yu et al.*, 2012).

5.1.2 Currently available methods for laminar fMRI in humans

Laminar fMRI developed later in humans than in animals due to technical difficulties related to measuring mesoarchitectural structures in the strongly convoluted cortex. The core findings from the animal literature apply also to findings in human studies. These studies are discussed in the scientific chapters in this thesis and omitted here in order to avoid repetition. Here, following the review by *Huber et al.* (2017a), the strengths and weaknesses of laminar fMRI methods currently available in humans are discussed in terms of signal specificity, sensitivity and quantifiability and the efficiency, availability and invasiveness of the acquisition method (see summary in Figure 5.1).

CBF is expected to be the most laminar specific as the signal measured with Arterial Spin Labelling (ASL) arises from the cortical depth specific permeable capillaries (*Golay et al.*, 2004). It is a quantitative technique, by means of which

absolute and relative changes in CBF can be measured. However, this technique presents a poor temporal efficiency. Due to the waiting time in the sequence, it is an inherently slow sequence (~2 s) and each measurement needs a label and control acquisition (~4 s per measurement). In addition, compared to GE-BOLD the sensitivity is 10%-20% (*Ivanov et al.*, 2016).

The signal measured using the Vascular Space Occupancy (VASO) sequence is proportional to the vascular volume in the voxel (*Lu et al.*, 2003). When used for fMRI, it measures the differences in vascular volume between rest and activation. The largest contribution to the blood volume change arises from the capillaries, but the laminar specificity of CBV measurements will be poorer than CBF's, as part of the volume changes will arise also from diving arteries and pial vessels, which will lead to a poorer laminar specificity with decreasing cortical depth. This technique measures relative changes in CBV (%), assuming a resting CBV. The temporal efficiency is not a strength of this technique due to the necessity to wait for the blood nulling time (around 1.5 s at 7 T). In addition, if an extra untagged image is acquired to correct for BOLD contamination (*Huber et al.*, 2014), the acquisition of a volume can be ~3 s at 7 T. Compared to GE-BOLD the sensitivity is 40%-60% and at the time of writing this thesis it is available in less than 10 labs around the world.

$CMRO_2$ activity is highly specific to the site of neuronal activation, but its measurement with MRI requires i) BOLD and CBF and/or CBV measurements, ii) a signal model (the Davis model) and iii) breathing of an innocuous gas mixture (usually carbogen or oxygen) that changes the vascular state without altering neuronal activity (calibrated fMRI (*Davis et al.*, 1998)). Hence its laminar specificity is conditioned by that of the BOLD/CBV/CBF measurements and the validity of the model and its parameters at the laminar level. Its temporal efficiency is poor, 3-8 s when functional steady state is reached and some subjects might experience the setting for gas inhalation unpleasant. 3-7 labs around the world have the equipment to measure calibrated fMRI.

The most straightforward approaches to measure brain activity are BOLD-based techniques. As seen in the previous chapter, SE-BOLD based measurements have a higher spatial specificity due to the lack of the extravascular contribution from large veins. Furthermore, the spatial specificity is expected to increase at higher fields as blood T_2 shortens and intravascular contribution becomes negligible at the TEs used. In this case, the laminar specificity would be similar to CBF. Nonetheless, SE at high fields at ultra-high resolution easily runs into SAR problems, especially if near full brain coverage is required. Besides, the temporal efficiency is lower than its GE-based counterpart's. The main weakness of GE-BOLD for laminar fMRI is its poor spatial specificity, which varies across layers.
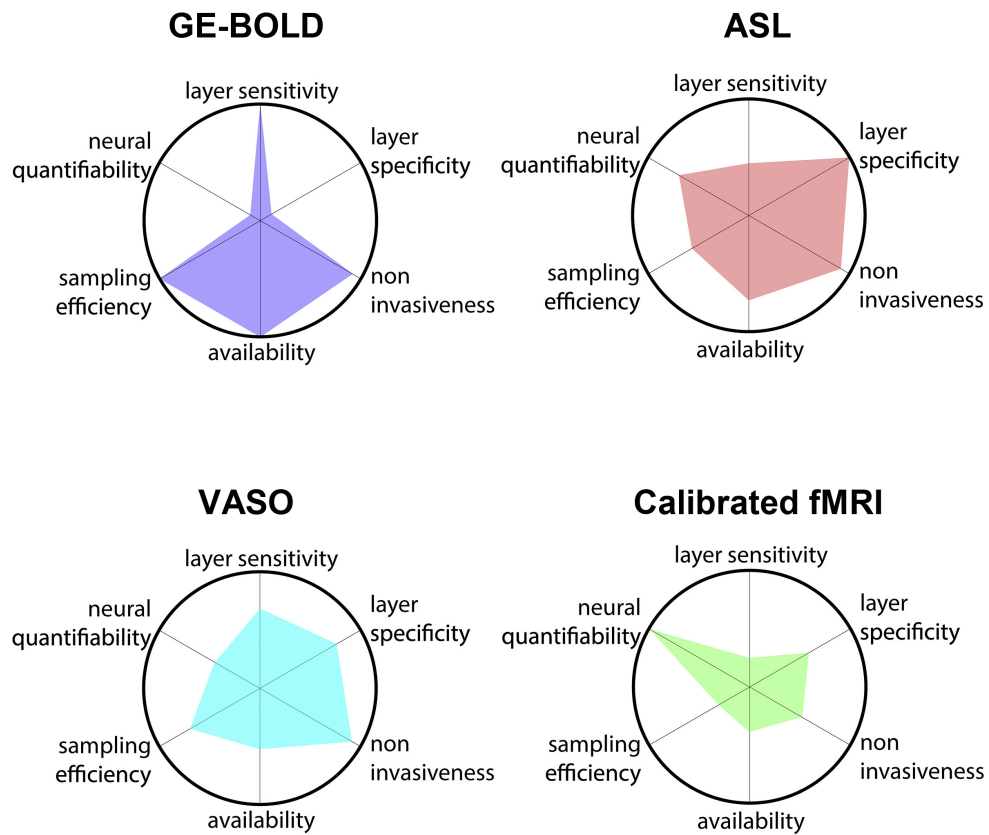
Figure 5.1: Summary of the most important quality features of BOLD, ASL, VASO and calibrated fMRI. All six compared parameters are normalized to the value of the fMRI method yielding the highest value. Figure modified from *Huber et al.* (2017a).

5.1.3   GE-BOLD based laminar fMRI: The interlaminar leakage problem

GE-BOLD outperforms the rest of the hemodynamic sensitive MR measurement approaches in terms of temporal efficiency and sensitivity to activation but has the poorest spatial specificity. The signal measured is the sum of small vessels (mostly capillaries) close to the site of neuronal activation and large vessels that can be located as far as a few millimetres from the site of neuronal activation. This gives rise to a signal leakage or signal spread problem. This problem is also present in standard resolution fMRI, the singularity of layer specific fMRI is that the signal leakage has a clear directionality: from lower layers to upper layers, as blood drains unidirectionally this way.

Approaches based on GE acquisition that deal with the interlaminar leak-age problem include using a differential approach (*Kashyap et al.*, 2017;

Sánchez Panchuelo et al., 2015), by which the contribution of veins can be reduced, or measuring the early BOLD response to activation (*Siero et al.*, 2011, 2013, 2015), which, as shown in animal studies, arises from capillaries close to the site of activation. In this work, two approaches to deal with this interlaminar leakage problem are studied: the deconvolution with an estimated physiological Point Spread Function (Chapter 7) and the acquisition of the S2-SSFP signal (Chapter 8).

5.2 Requirements of laminar fMRI

Functional MRI assumes neuronal activity can be inferred on the basis of hemodynamic changes. Hence, the fundamental requirement for laminar fMRI is the laminar specific regulation of the hemodynamic response to activation. Evidence of this has been presented in this thesis in subsections *Neurovascular Coupling* and *Brief overview of laminar resolution fMRI*. Therefore, this section will address the technical requirements regarding the acquisition and segmentation.

5.2.1 Acquisition Considerations in Laminar fMRI

The resolution required for laminar work depends on the research question, analysis method and brain regions studied. The neocortical thickness varies between ~1 and 5 mm and is highly region dependent. As a general rule, a minimum of three voxels across the cortex is advisable to distinguish the granular, supragranular and infragranular laminar signal. Thus, in thinner regions such as the primary visual cortex (~2.2 mm) the maximum voxel size would be ~0.8 mm through cortex. Appropriate voxel geometry is also region dependent. As the primary visual cortex is strongly curved in all three spatial dimensions, the voxels should be isotropic in order to avoid interlaminar contamination. Less curved areas, such as the primary motor cortex, can accommodate anisotropic voxels, but the slice orientation must be appropriately set, with the largest voxel dimension along the uncurved dimension of the region.

If everything else is kept unaltered, small voxel sizes come with two drawbacks: SNR will be reduced and acquisition time will be increased. The increased acquisition time does not severely affect the measurement of the hemodynamic changes measured in laminar fMRI, these happen in the order of seconds instead of tens of milliseconds, but it decreases the efficiency of the sequence.

5.2.2   Segmentation and co-registration

In order to process laminar activation, it would be optimal to have a good anatomical segmentation of grey matter and layers therein. Unfortunately, layers, with the exception sometimes of layer IV in the primary visual cortex (stripe of Gennari) are not visible in $T_2^{(*)}$-weighted fMRI. Therefore, functional scans are accompanied by an additional anatomical scan with good WM/GM contrast. The laminar division of the cortex is done on the anatomical scan based on local cortical depth (equidistant approach: *Koopmans et al.* (2011); *Polimeni et al.* (2010)) or, following the Bok principle, based on cortical depth and local curvature (equivolume approach: *Kemper et al.* (2017); *Kok et al.* (2016); *Waehnert et al.* (2013)). Equivolume sampling yields a slight advantage over equidistant sampling given the current limitations of fMRI voxel size, participant motion, coregistration and segmentation (*Kemper et al.*, 2017).

Functional data, including high-resolution functional scans, are usually acquired using echo planar imaging, which suffers from drop-out and distortion artefacts. MPRAGE and MP2RAGE are sequences commonly used to obtain anatomical scans, from which segmentation can be straightforward. These scans do not suffer from the typical EPI distortions of the functional scan; therefore, a distortion correction step has to be performed. The final results depend on the success level of the distortion correction. Recently, distortion matched acquisitions, EPI with inversion recovery, have been proposed to overcome suboptimal segmentation of the functional data (*Huber et al.*, 2016; *Kashyap et al.*, 2016; *van der Zwaag et al.*, 2018).

Chapter 6

A cortical vascular model for examining the specificity of the laminar BOLD signal

Abstract

Blood oxygenation level dependent (BOLD) functional MRI has been used for inferring layer specific activation in humans. However, intracortical veins perpendicular to the cortical surface are suspected to degrade the laminar specificity as they drain blood from the microvasculature and BOLD signal is carried over from lower to upper cortical layers on its way to the pial surface. In this work, a vascular model of the cortex is developed to investigate the laminar specificity of the BOLD signal for Spin Echo (SE) and Gradient Echo (GE) following the integrative model presented by *Uludağ et al.* (2009). The results of the simulation show that the laminar point spread function (PSF) of the BOLD signal presents similar features across all layers. The PSF for SE is highly localised whereas for GE there is a flat tail running to the pial surface, with amplitude less than a quarter of the response from the layer itself. Consequently, the GE response at any layer will also contain a contribution accumulated from all lower layers.

6.1   Introduction

The human neocortex is a convoluted 2-3 mm thick neuronal sheet that is divided into six histological layers in most cortical areas. These layers have a generic pattern of feed-forward connections to higher order brain regions or feedback connections to lower order cortical or subcortical regions (*Douglas and Martin*, 2004; *Thomson and Bannister*, 2003). Layer specific functional activation patterns could hence improve the current understanding of within and between region connections at rest and activation.

Blood Oxygenation Level Dependent (BOLD) measurement by Magnetic Resonance Imaging (MRI) is the most commonly used non-invasive technique for measuring brain activation. The Spin Echo (SE) BOLD signal is generally considered to be less sensitive than the Gradient Echo (GE) BOLD signal, because the 180° refocusing pulse applied rephases the contributions in the static dephasing regime, i.e. the dephasing that results from the intravascular frequency offset (vascular dephasing) and the extravascular dephasing around vessels larger than 20 μm (*Ogawa et al.*, 1993). However, if the intravascular dephasing contribution can be neglected because of a very short intravascular T_2-value, then the SE-BOLD signal is expected to be more spatially specific (*Lee et al.*, 1999) because the remaining dynamic averaging contribution will be driven by smaller vessels that are closer to the site of neuronal activation (*Boxerman et al.*, 1995). The GE-BOLD signal, on the contrary, will have a strong contribution from larger veins (*Barth and Norris*, 2007) and will therefore be more sensitive to changes in blood oxygenation but less spatially specific (*Sánchez Panchuelo et al.*, 2015).

These differences in BOLD sensitivity between SE and GE sequences are particularly relevant for layer specific BOLD. The cortical vasculature has a distinct arrangement by which a tangled microvascular network is drained by intracortical veins (ICV). These veins run perpendicular to the surface, drain blood along their way and flow into pial veins on the cortical surface (*Duvernoy et al.*, 1981). Therefore, activation in a lower cortical layer will have an effect in upper layers as blood is carried through the cortex on its way to the pial surface. GE-BOLD data is expected to be more affected by this carry-over effect as it is more sensitive to larger vessels. To date, laminar BOLD measurements have been performed using both SE (*Goense and Logothetis*, 2006; *Harel et al.*, 2006a; *Zhao et al.*, 2004) and GE (*Chen et al.*, 2013; *De Martino et al.*, 2013; *Koopmans et al.*, 2009, 2011; *Polimeni et al.*, 2010), yielding a range of BOLD profiles across the cortex for both types of MR sequences. The interpretation of these profiles remains problematic without some measure of the spatial point spread function for the BOLD response in differing experimental situations. Unlike conventional BOLD imaging which can utilise retinotopic mapping to obtain a measure of the spatial PSF (*Engel et al.*, 1997) analogous experiments have not been established for laminar fMRI. Hence,

modeling approaches remain as the sole possibility of better understanding the excitation profiles obtained experimentally.

In this paper a simple model of cortical vasculature is developed. The model is based on histological observations and captures the vascular differences across cortical layers in the human primary visual cortex (V1). Based on the local vascular features, the static BOLD response to equal neurovascular response across the cortex is predicted following the two compartment BOLD signal model proposed by *Uludağ et al.* (2009). This model is then applied to analyse the laminar/ICV contributions to the total BOLD signal across the cortex; estimate the depth dependent laminar specificity of the BOLD signal and the laminar physiological point spread function (PSF) for both GE and SE.

6.2 Model and simulations

6.2.1 Vascular model of the cortex

In order to examine the laminar specificity of the BOLD signal, the cortical vasculature is divided into two parts in this work: 1) the intracortical veins (ICV) that run through the cortical layers perpendicular to the cortical surface, and 2) the part of the vasculature, which is composed of tangled, randomly oriented venules, capillaries and arterioles, called the laminar network here. The vascular model of the human primary visual cortex proposed is developed by combining the known volume and vessel distribution of the laminar network (*Boas et al.*, 2008; *Weber et al.*, 2008) with the density and features of ICVs (*Duvernoy et al.*, 1981; *Park et al.*, 2005b) in order to obtain the number and diameters of the ICVs required to drain the blood in the modeled cortical region. Arteries are not considered in this vascular model because it has been shown that their contribution to the BOLD signal at higher fields is negligible (*Gagnon et al.*, 2015). For simplicity, pial veins are not part of this model, but their effect on the BOLD signal in the parenchyma will be discussed.

The laminar network

The vascular volume of the laminar network varies across the cortex between 2 and 2.7% and is on average 2.3% in the macaque V1 (*Weber et al.*, 2008). The vascular compartment distribution of the laminar network in this model is 21% arterioles, 36% capillaries and 43% venules, which is derived from the Vascular Anatomical Network (VAN) proposed by *Boas et al.* (2008). This VAN is a vascular model that branches from one arteriole through 2^6 capillaries to one draining venule. In each of the six branching steps, a vessel splits into (arterial side) or

reconnects (venous side) two vessels of a smaller diameter. Arterioles have a diameter between 10 and 30.5 µm, capillaries have a diameter of 8 µm and venules have a diameter between 12 and 36.6 µm. Between branching steps, all vessels are 100 µm long, except for the capillaries, which are 250 µm long.

Intracortical veins

Intracortical veins are perpendicular to the cortical surface and flow into large pial veins on the cortex. *Duvernoy et al.* (1981) provides a thorough description of ICVs and classify them in five groups based on their diameter and reach: V5 veins have an average diameter of 120 µm and emerge from white matter. Veins from groups V4, V3, V2 and V1 have average diameters of 60 µm, 45 µm, 30 µm and 20 µm and originate in histological layers VI, IV, II/III and I, respectively (see Figure 6.1). Intracortical veins drain all the layers they pass through and their diameters increase as they approach the surface because they are swollen by incoming laminar venules (*Turner*, 2002). The cortical layer boundaries of human V1 in the model were fixed following *de Sousa et al.* (2010) and *Burkhalter and Bernardo* (1989): Layer VI, 20%; Layer V, 10%; Layer IV, 40%; Layer II/III, 20%; Layer I, 10% (values rounded to the closest multiple of 10). Hence, as the average cortical thickness of the primary visual cortex is 2.5 mm (*Fischl and Dale*, 2000), the thinnest cortical layers (layers V and I) are roughly 0.25 mm thick. In this work, the cortical vascular model comprises 10 voxels, with a base of 0.75 x 0.75 mm^2 and a height of 0.25 mm expanding from the WM/GM boundary to the cortical surface. Hence, the thinnest layers are one voxel thick and thicker layers extend over an integer number of voxels. However, the voxel size simulated is about three times smaller than the smallest voxel volumes used in experimental high-resolution fMRI studies in humans. To allow a better comparison with experimentally obtained profiles, the BOLD signal across the cortex obtained using the 10 voxels is convolved with the smoothing kernel calculated in *Koopmans et al.* (2011). This kernel was calculated by projecting onto a line an isotropic voxel averaged over all possible orientations, to account for the blurring introduced by generating laminar profiles by integrating over extended patches of cortex, obtaining a FWHM of 87% of the voxel size.

Duvernoy et al. (1981) found that vessels are organised in a circular pattern on the cortical surface. Along the axis of each venous unit runs either one principal vein (ICV of group V5) or two intermediate size veins (ICVs of group V4 or V3). The diameter of a unit centred on intermediate size veins was 0.75-1 mm, whereas the diameter of those centred on a principal vein ranged from 1 to 4 mm. In line with the model voxel area given above, the vascular model developed is centred on two intermediate veins. This way, all model voxels belong to the same venous unit and partial voluming between adjacent venous units is avoided.

Regarding the intracortical vessel density across the cortex, MR-venography in the somatosensory cortex of rats and in the visual cortex of cats showed that ICV
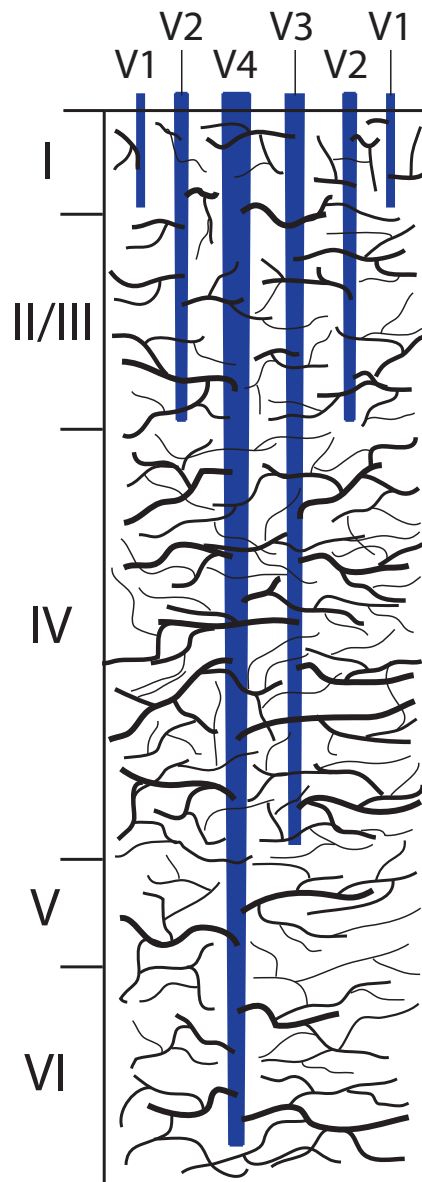
Figure 6.1: Schematic representation of the vascular model developed. Intracortical veins (in blue) run perpendicular to the cortical surface and drain blood from all layers they pass through. The microvascular density is highest in layer IV.

density increases roughly linearly from the lower part of the cortex (1 vein/mm²)
to the surface of the cortex (6 veins/ mm²) (*Park et al.*, 2005b). These magnitudes
do not vary much between the two species and brain regions considered, hence
they are considered valid for human V1 too.

Once the characteristics of the ICVs are known, their diameters at each depth are
calculated based on the laminar flow that needs to be drained, i.e. the total cross
sectional capillary flow. Following *Zweifach and Lipowsky* (1977) the velocity of
blood through the vessels is roughly proportional to their diameter and therefore,
as stated in *Turner* (2002), Murray's law applies, by which the sum of the cubes
of the average radii of all capillaries in the layer and the radii in the entering layer
boundary of the ICVs equals the sum of the cubes of the radii of the ICVs in the
exiting layer boundary (Equation 6.1):

$$\sum_i r^3_{ICVout_i} = \sum_j r^3_{ICVin_j} + \sum_k r^3_{capLayer_k} \tag{6.1}$$

where *i* runs over the ICVs emerging from a layer, *j* over the ICVs entering that
layer and *k* over the capillaries in the layer. The number of capillaries is obtained
by dividing the capillary volume in a layer by the volume of one capillary. As the
capillary volume across the cortex is known, iteratively applying Equation 6.1 for
each voxel starting from the voxel closest to the GM/WM boundary, the diameters
of the ICVs across the cortex are obtained. It is assumed that laminar flow is
equally distributed among the draining ICVs present in the voxel. The number of
the V2 and V1 ICVs was chosen such that the number of ICVs increased roughly
linearly and that the diameters obtained on the cortical surface were close to the
observations in *Duvernoy et al.* (1981), as explained earlier.

Following the steps described here, a vascular model is obtained in which the
arteriole, capillary, venule and ICV volume density vary across the cortical depth.
A schematic illustration of the main features of the vascular model is shown in
Figure 6.1. Based on these vascular features, the depth dependent BOLD signal
can be predicted applying the BOLD signal model.

6.2.2   BOLD signal model

The static BOLD signal at rest is modelled as the volume weighted sum of the in-
travascular and extravascular BOLD signal (Equation 6.2), following *Obata et al.*
(2004) and *Uludağ et al.* (2009):

$$S = (1 - CBV) \cdot S_{EV} + \sum_i CBV_i \cdot S_{IV_i} \tag{6.2}$$

where *CBV* is the cerebrovascular volume, S_{EV} and S_{IV} are the BOLD signals arising from the extravascular and intravascular compartments, respectively, and subindex *i* refers to the different vascular compartments (i.e. arterioles, capillaries, venules and intracortical veins). Activation of the cortical region leads to vascular dilation and changes in deoxyhemoglobin content, altering the intravascular and extravascular signals and the vascular volume in the region. The fMRI signal, $\Delta BOLD = \Delta S / S$, is given as the normalized signal difference between the activation and baseline states.

If T_1 relaxation can be neglected, the relaxation component of the MR signal can be described by a monoexponential function: $S_{EV,IV} = S_{0_{EV,IV}} \cdot e^{-\left(R_{2_{EV,IV}}^{(*)} TE\right)}$. The parameters of the signal model in this simulation are set following *Uludağ et al.* (2009). As the BOLD signal change is normalized to its baseline value, S_0 can be considered to be equal to the proton densities of the extravascular and intravascular compartments, which, for simplicity, are considered to be equal in this work. The transversal relaxation rate $R_2^{(*)}$ can be given as the sum of the intrinsic, $R_{2,0}^{(*)}$, and deoxyhemoglobin dependent, $R_{2,dHb}^{(*)}$, relaxation rates: $R_2^{(*)} = R_{2,0}^{(*)} + R_{2,dHb}^{(*)}$. Based on own or published *in-vivo*, ex-vivo and simulated data, Uludağ and colleagues provide a comprehensive compilation of intrinsic and oxygenation dependent relaxation rates for a range of field strengths between 1.5 and 16.1 T, blood oxygenation levels or vessel size and orientations both in the extravascular and intravascular compartments for SE and GE sequences (B_0: 1.5, 3, 4, 4.7. 7, 9.4, 11.7, 14 and 16.1T and echo times for each simulated field of 96, 77, 65, 60, 50, 41, 33, 29 and 26 ms for SE and 66, 48, 41, 37, 28, 22, 19, 17 and 15 ms for GE).

The hemodynamic response to neural activation is modeled as an increase in the vascular volume and the blood oxygenation. Microvascular vessels, i.e. arterioles, capillaries and venules smaller than 20 μm in diameter, increase their volume by 16%, which under Grubb's law corresponds to a 50% increase in blood flow. Venules larger than 20 μm in the laminar network and ICVs are considered not to dilate as shown by *Hillman et al.* (2007). Regarding blood oxygenation, oxygen saturation, Y, increases from 60% to 70% in the postcapillary vessels, from 77.5% to 85% in the capillaries and from 95% to 100% in arterioles between the baseline and activated states.

The BOLD signal across the cortex is predicted on the basis of the number and diameters of the ICVs obtained from the vascular model and the known varying vascular density and distribution of the laminar network. The extravascular signal dephasing around the vessels depends, among other parameters, on their orientation with respect to B_0. Vessels in the laminar network can be considered to be randomly oriented, but intracortical vessels in a vascular unit are perpendicular to the surface and have a specific orientation. However, layer specific BOLD measurements in humans are often processed by integrating the laminar BOLD

signal along a convoluted patch of cortex. Along this integration line, the effect of ICVs can be considered to be that of randomly oriented, as their orientation with respect to B_0 will change with the curvature of the cortex. Thus, the results shown here are calculated by applying extravascular dephasing parameters calculated for randomly oriented vessels as given in *Uludağ et al.* (2009).

6.2.3   Analysis of the laminar BOLD signal

The vascular-BOLD model is implemented in MATLAB (2012a, The MathWorks, Inc.) and predicts the equilibrium BOLD response across the cortex to a continuous stimulus. These simulations assume equal net excitatory neuronal activity and neurovascular coupling across the cortex. Similarly, it is considered that the hemodynamic response spatially overlaps with the underlying neural activity and that it is laminar specific as suggested by the combination of depth dependent electrophysiological (*Jones et al.*, 2004) and BOLD signal (*Yu et al.*, 2014) onset time measurements to whisker pad stimulation in rats.

This work analyses the BOLD signal contributions of the laminar vasculature and ICVs in order to examine the laminar BOLD specificity and the carry over or signal leakage to more superficial layers. This unidirectional leakage (i.e. from the layer of activation towards the cortical surface) is obtained by calculating the downstream changes in oxygenation and blood flow for each layer. The Point Spread Function (PSF) of the BOLD signal is then calculated for each layer. These curves do not represent the activation of a point but rather of a small volume of activated cortex, i.e. the small voxel of 0.75x0.75x0.25 mm^3 used in the simulations, which is considered to be sufficiently small to analyse the variation of the PSF between layers.

The peak to tail ratio, is defined as the ratio between the magnitude of the peak of the laminar PSF and the average magnitude of the tail over all downstream layers. In order to illustrate how the underlying neurovascular response affects the physiological PSF, the peak to tail ratio is explored under different strengths of regional hemodynamic and metabolic responses for 3 T and 7 T. Experimental values for the regional blood flow-metabolism coupling constant, n $\left(n = \frac{\%\Delta CBF}{\%\Delta CMRO_2} \right)$ were taken from *Griffeth et al.* (2014), where n was measured for visual stimuli that consisted of flickering checkerboards with 10% and 40% contrasts and of a movie. It is assumed that the hemodynamic response scales equally in all layers with these reported regional variations and the oxygen saturation Y in the vasculature is obtained applying Fick's principle (*Kim et al.*, 1999).

Given that high (sub-millimetre) resolution fMRI benefits especially from the increase in MR sensitivity at 7 T (*Triantafyllou et al.*, 2005) and following recent laminar fMRI studies (*Koopmans et al.*, 2011; *Olman et al.*, 2012; *Polimeni et al.*,

2010; *Siero et al.*, 2013), laminar specificity comparisons between SE and GE are given at this field strength for simplicity. The features of the physiological point spread function are given for a range of field strengths between 1.5 T and 16 T to assess the variation of the laminar specificity across fields.

6.3   Results

6.3.1   Intracortical veins and vascular volume

The diameters of the intracortical veins obtained are in line with the average values reported by *Duvernoy et al.* (1981), as shown in Table 6.1. These results reflect the fact that the vascular territory drained by a single vessel has a cone-like shape, with its broad base in the lower layers. V4, for example, drains a larger territory in layer V, where it is the only type of vein present, than in Layer II/III, which is drained by several types of ICVs. According to (*Lorthois et al.*, 2011), the vascular territory drained by a vessel of 55 μm diameter will have a radius of 340 μm, which corresponds to the vascular territory drained by V4 in Layers V and VI in the model developed here.

The calculated vascular volume across the cortex of the laminar vasculature and ICVs, Figure 6.2, is in good agreement with the measurements related to the depth-dependent vascular density performed by *Cassot et al.* (2006) using confocal laser microscopy in excised and ink-injected sections of human cortex. The contribution of the laminar network to the total vascular volume is larger all across the cortical depth, even though ICV volume increases roughly from 0.2% to 1.5% as the cortical surface is approached.

	V4	V3	2xV2	2xV1
Layer VI	41.4			
Layer V	52.4			
Layer IV	59.1	39.1		
Layer II/III	63.6	48.4	24.6	
Layer I	64.6	50.1	30.2	19.0

Table 6.1: Average vessel diameters (in μm) of the intracortical veins across the cortex of a vascular unit centred around two smaller vessels of groups V4 and V3. The vascular unit has one vein of groups V4 and V3 and two veins of groups V2 and V1.
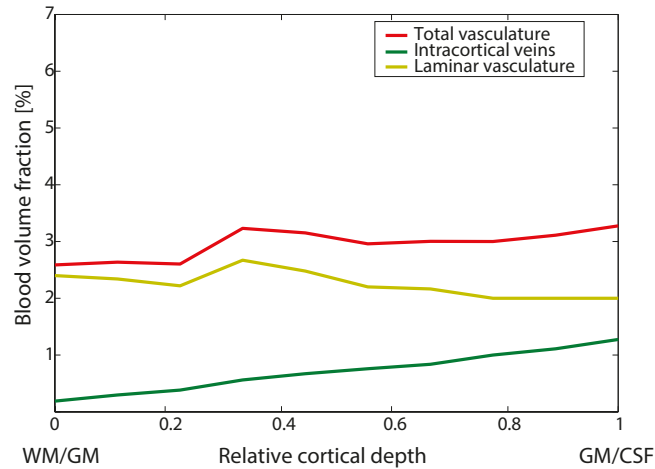
Figure 6.2: CBV volume fraction across the modeled cortex for the laminar network (yellow), intracortical veins (green) and the sum of the ICV and laminar network vascular volume (red).

6.3.2   BOLD response across the cortex

The intravascular and extravascular contributions to the BOLD signal changes are shown in Figure 6.3a,b. For the SE-BOLD response the EV contribution is almost twice as strong as the IV contribution and the BOLD profile has a maximum where the laminar vascular density is highest, which corresponds to histological layer IV. For GE, under the working assumption made in this paper following *Uludağ et al.* (2009), the IV contribution to the BOLD signal is neglected from 7 T upwards and hence the BOLD signal is entirely of extravascular origin. Note that pial vessels are not considered in this model, therefore the cortical GE-BOLD profile shown is the result of the decrease in vascular density from the cortical surface to the GM/WM boundary (Figure 6.2), especially due to the decrease in ICV density, and is not related to the long ranging effects of pial vessels at the cortical surface. Table 6.2 shows that the magnitude of the simulated BOLD responses are within the experimental ranges obtained in awake humans at 7 T.

As expected, the SE-BOLD signal is highly laminar specific as it is dominated by the laminar contribution at all cortical depths (Figure 6.3c,e). The GE-BOLD signal, on the other hand, is driven by ICVs for the most part of the cortex, especially in upper cortical layers, where the ICV density is also highest (Figure 6.3d). In this sense, it is apparent from Figure 6.3e,f that the laminar specificity of the BOLD signal decreases as the cortical surface is approached, most significantly for GE-BOLD. Under the current simulation parameters of equal metabolic and vascular response across the cortex, most of the GE-BOLD signal obtained in the upper layers is the result of activation in lower cortical layers.

	Simulation (manuscript)	Experimental studies (literature)
Spin Echo	1.5-2.3%	1-2% [f]
Gradient Echo	1.5-4%	2-4% [a,c,d]
		0.5-3% [b]
		1.5-5% [e]

Table 6.2: Quantitative comparison of simulated profiles with experimental values reported in the literature for 7 T in awake humans. The ranges in the table refer to minimum and maximum magnitude of the BOLD signal profile across the cortex. Experimental values were obtained in the visual[a,b,d,e,f] and motor cortex. a: *Polimeni et al.* (2010), b: *Koopmans et al.* (2011), c: *Huber et al.* (2015), d: *De Martino et al.* (2013), e: *Siero et al.* (2015), f: *Kemper et al.* (2015).

The laminar PSF of the BOLD signal for different layers are shown in Figure 6.4 a) and b), for SE and GE respectively. The laminar PSF for layer I is not given as ICVs here drain into pial veins on the cortex. These curves present two interesting features: first, the laminar spread function shows very little variation between layers, neither for SE nor for GE. As shown in Figure 6.3, the SE-BOLD data has very little contribution from ICVs, hence the SE-BOLD signal is highly laminar specific and spreads very little through the cortex (Figure 6.4a). GE-BOLD data, on the contrary, has a considerable contribution from ICVs, and hence a larger laminar spread, but this does not vary much between layers either. Second, the tail of the BOLD signal spread is rather constant through the layers downstream of the activation site. This occurs despite the fact that blood oxygenation in ICVs decreases as they approach the cortical surface and blood drained from the activated layer is diluted with blood from non-activated layers. The explanation for this apparently counter-intuitive phenomenon is that the diameters of the ICVs increase with decreasing cortical depth. The extravascular signal decay around randomly oriented vessels between 16-200 μm varies in a near linear fashion with both the oxygen saturation and the volume of the vessel (*Uludağ et al.*, 2009). This means that the expected decrease in BOLD signal difference due to the dilution effect is compensated by the increased volume of the vessels, and hence the tail of the BOLD signal spread remains nearly constant.

The ratio between the peak and the average magnitude of the tail is defined as the peak to tail ratio. Figure 6.5a shows the field strength dependence of this ratio for GE-BOLD data. The trend for SE-BOLD is not shown because it is high enough
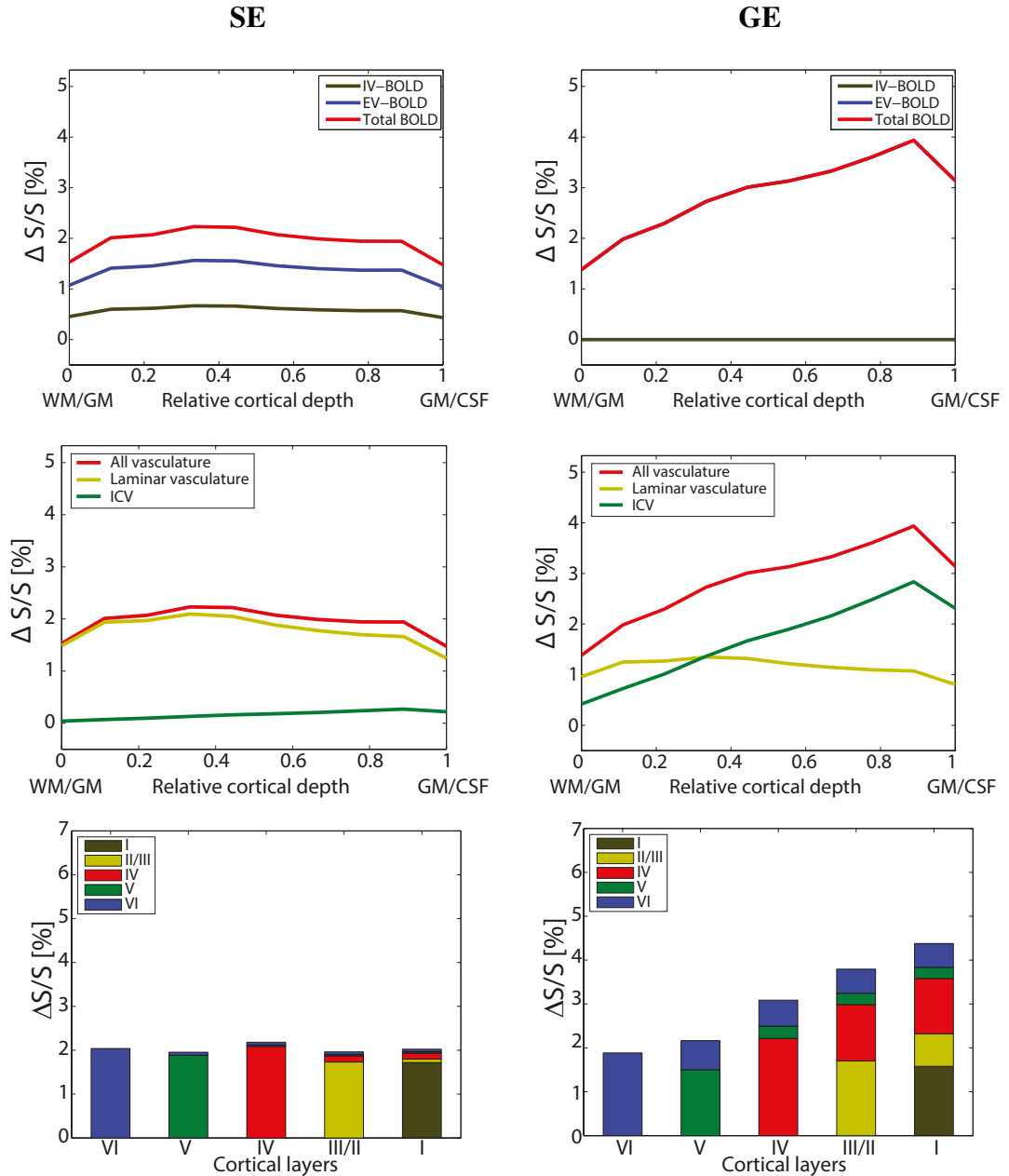
Figure 6.3: First row: total (red), intravascular (brown) and extravascular (blue) activation profiles across the cortex. Second row: laminar network (yellow), ICV (green) and total (red) activation profiles along the cortex. Third row: the BOLD signal broken down according to the contribution from the same layer and layers upstream. Note that all simulations were done using B_0=7 T, TE_{SE}=50 ms, TE_{GE}=28 ms and that the thickness and the total vascular volume of the layers is not equal. The left column refers to SE and the right column to GE.

a)   b)

Figure 6.4: The laminar BOLD PSF at 7 T for the activation of a 0.75x0.75x0.25 mm^3 voxel within a single layer located in layer VI (blue), V (green), IV (red) and II/III (yellow) for **a)** SE and **b)** GE .

to be considered laminar specific across all field strengths (the lowest value is obtained for 3 T and it is over 30). The average across lamina of the peak to tail ratio is between 4 and 7 for field strengths between 1.5 T and 16 T. It has a minimum at 7 T, the field strength at which our working hypothesis assumes that the IV contribution vanishes, and from here on it increases steadily with increasing B_0. In the presence of an IV contribution of 10% to the total BOLD signal at 7 T, for example, this ratio will be higher and the minimum will be shifted to lower field strengths. However, the curve is useful to give a notion of upper and lower bounds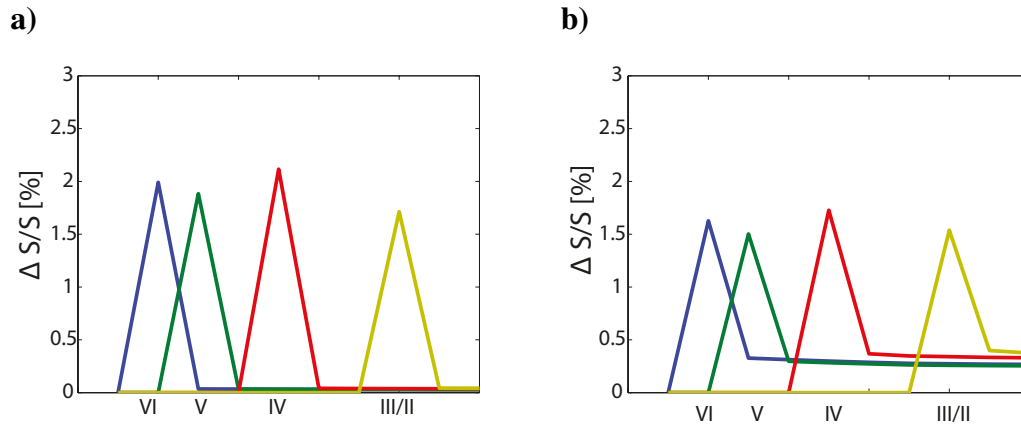 of laminar specificity across field strengths for GE-BOLD data. Further, in this work, the BOLD profiles after integrating over an extended convoluted patch of cortex are simulated, and hence ICVs are considered to be randomly oriented. However, if no such extended integration is performed, the peak to tail ratio will vary with the orientation of the cortex. For example, if ICVs are oriented perpendicularly to B_0, their contribution to the BOLD signal increases, and compared to the simulated peak to tail ratios at 7 T shown in this work, the peak to tail ratio will be reduced by about 25% (data not shown). The results shown in Figure 6.5b suggest that peak to tail variations based on changes of CBF follow a similar pattern across field strengths (results shown for 3 T and 7 T) and that the peak to tail ratio or the laminar specificity is comparable for low contrast visual stimuli.

6.4 Discussion

A vascular model of the primary visual cortex has been developed to examine the laminar specificity of the BOLD signal. The activation profiles through the cortex
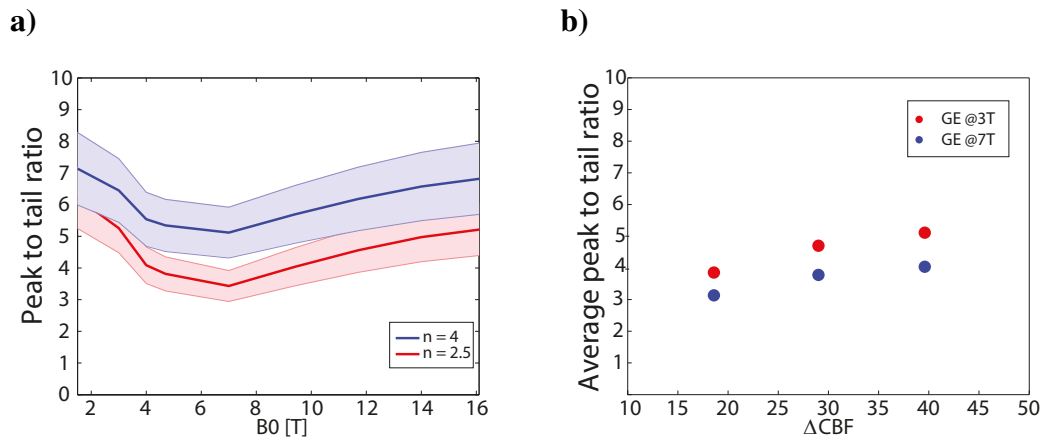
a)
b)

Figure 6.5: **a)** The average laminar peak to tail ratio across field strengths for GE-BOLD (the shaded region represents the standard deviation) for $n = 4$ (blue), as in *Uludağ et al.* (2009), and $n=2.5$ (red), average n in *Griffeth et al.* (2014). **b)** The average peak to tail ratio for GE-BOLD at 3 T (red) and 7 T (blue) for the regional CBF increases and blood flow metabolism coupling constant, n, reported in *Griffeth et al.* (2014) ($n=2.5\pm0.2$).

obtained in Figure 6.3a,b are similar to those obtained by *Goense and Logothetis* (2006); *Polimeni et al.* (2010); *De Martino et al.* (2013); *Zhao et al.* (2004); *Chen et al.* (2013). As expected, the results of the simulation show that there is BOLD signal leakage from lower layers to upper layers through the intracortical veins, Figure 6.3d,f.

6.4.1   Laminar specificity of SE- and GE-BOLD signal

Figure 6.3e,f show that SE-BOLD signal is highly layer specific whereas the laminar specificity of GE-BOLD signal decreases as the cortical surface is approached. In fact, for equal vascular and metabolic responses across all layers, the cumulative contribution from lower layers is higher than the laminar GE-BOLD signal in superficial layers. This carry-over effect implies that care must be taken when comparing activation strengths between the different lamina within a region, or inferring connectivity between more distant regions when GE sequences are used. The use of differential designs (i.e. subtracting BOLD signal profiles for tasks with different layer distributions), as in *Trampel et al.* (2012); *Olman et al.* (2012); *Sánchez Panchuelo et al.* (2015), can alleviate the carry over effect (see *Supplementary Information*).

The laminar PSF in Figure 6.4 shows some interesting features: the peak to tail ratio does not vary considerably between layers and the tail remains rather constant across the downstream layers. In addition, the peak to tail ratios are comparable for similar CBF-CMRO$_2$ coupling constants and varying CBF increase upon activation, Figure 6.5b. These properties of the laminar PSF could form the basis

for a deconvolution or forward model fitting approach that would facilitate the extraction of the laminar specific BOLD signal for GE-BOLD. It is interesting that the laminar BOLD signal change is stronger for SE than GE sequences at the commonly used echo times of 50 ms and 28 ms, respectively, (see laminar BOLD signal contributions, in blue, in Figure 6.3c,d). However, SE sequences are RF intensive, which results in a higher power deposition that, at the high field strengths and resolutions favoured for laminar fMRI, might hit SAR limits. Further, it is difficult to collect high resolution SE data over extended volumes of cortex with a reasonable TR and the lengthy read-out required, especially for SE-EPI, introduces a non-negligible T_2' contribution (*Goense and Logothetis*, 2006).

6.4.2 Neurovascular response across the cortex

In the simulation results presented here, the vascular response is assumed to be equal across the cortex. However, the vascular response is expected to vary with cortical depth as neuronal activity is not expected to be evenly distributed over the cortical layers. It has been shown that in response to visual stimulation, neural circuits within layer IV tend to consume more energy compared to other layers, reflecting laminar differences in glucose uptake (*Tootell et al.*, 1988), and that there are long-term changes in neuronal activity related to metabolic activity (*Horton*, 1984). The BOLD signal reflects the input and intracortical processing in a region more, as measured by the local field potential (LFP) (*Logothetis et al.*, 2001). Hence, cortical depth dependent electrophysiological recordings of LFP obtained with array probes could potentially be used as a measure of the underlying neural activity that drives the BOLD response.

6.4.3 Intravascular T_2 and signal relaxation during read-out

The parameters of the BOLD signal model have all been taken from the comprehensive article by *Uludağ et al.* (2009) and, following this work, the intravascular contribution to the GE-BOLD signal at 7 T (and above) has been neglected. However, *Donahue et al.* (2011) showed that in fMRI measurements using 3.5 mm isotropic voxels at 7 T, the EV-BOLD contribution to the total GE-BOLD signal was between 75 and 90%. Cortical GE-BOLD signal profiles and PSF with an intravascular contribution at 7 T of 10% and 23% are shown in Figure S6.1. The specificity of the laminar activation, which is measured as the peak to tail ratio in this work, increases with increasing intravascular contribution because the volume of laminar vasculature is higher than the volume of ICVs all across the cortex (Figure 6.2) and the higher SO_2 change in the ICV compared to arterioles and capillaries does not compensate for the differences in volume. Nonetheless, the BOLD profiles and shape of the PSF are similar with and without the presence of an intravascular contribution to the BOLD signal and its presence does not considerably change the conclusions of this work.

Further, T_2' weighting as a result of signal relaxation during readout in non purely SE sequences such as SE-EPI, has been neglected. Hence, the results here represent the highest attainable laminar specificity. As experimentally shown by *Budde et al.* (2014); *Goense and Logothetis* (2006), the longer the acquisition window used the larger the contribution from larger veins is in SE-BOLD data, because of the increase in the T_2' weighting of the acquired signal.

6.4.4   Validity of the simulations with regard to the duration of the stimulus

In this work, veins larger than 20 μm were assumed not to dilate, but it is worth discussing the stimulus condition that apply to this physiological response. There are a number of publications that investigated venous dilation with regard to the length of the stimuli used. It has been reported that venous dilation is negligible for stimuli shorter than 20 s (*Hillman et al.*, 2007; *Kim et al.*, 2007; *Kim and Kim*, 2011), whereas for stimuli longer than 20 s venous dilation was observed (*Drew et al.*, 2011; *Huo et al.*, 2015; *Kim and Kim*, 2011).

In this manuscript the static BOLD response to activation was simulated. As the transit time through the cortical vasculature (i.e. from pial arteries back to pial veins) is around 1 s, the cortex will be in steady state for stimuli longer than this duration. Therefore, the simulation conditions apply for stimuli in the range from 1 s to 20 s.

6.4.5   Effect of pial veins in the parenchyma

On average, three veins between 0.1-2 mm drain each side of the occipital lobe (*Andrews et al.*, 1989), but most of the central veins have a diameter between 280-380 μm and peripheral veins of 130 μm (*Duvernoy et al.*, 1981). Given the low number of 1 mm diameter veins, the strongest possible long ranging effect of a 380 μm pial vein was studied to assess the long ranging effects of pial vessels on the parenchyma (data not shown). In this situation the vessel has to be oriented perpendicularly to B_0, a lobe of the dipolar field has to be perpendicular to the cortical surface, and the pial vessel experiences the maximum oxygenation change upon activation considered in this model, which will occur as a consequence of the full activation of a circular cortical area 9.7 mm in diameter. Even when using this worst case scenario, the field dephasing induced across the first 250 μm from pial surface into the parenchyma (i.e. first simulated voxel) is only roughly a quarter of the intravoxel dephasing induced by the laminar network in this layer. As the long ranging effect decays with $1/r^2$, in the next 250 μm the dephasing is already negligible. Smaller pial veins can induce a stronger dephasing along the first 250 μm, but will be negligible for the rest of the cortical profile. Therefore,

in the absence of partial volume effects, the long range effect is confined to the superficial layer I. For a plausible voxel size for laminar BOLD signal, such as a 0.75 mm isotropic voxel and due to the convoluted cortex (effect of the pial veins will be randomized), integration would reduce these effects further.

6.4.6   Validity of the vascular model

The laminar vascular density across the cortex in this model follows the vascular density in macaque V1 reported by *Weber et al.* (2008). This distribution is in agreement with other works that report an increased vascular density in layer IV (*Duvernoy et al.*, 1981; *Zheng et al.*, 1991) and roughly corresponds to the description of vascular layers in *Lauwers et al.* (2008), in which authors show a profile that is slightly flatter and smaller in microvascular density for the human collateral sulcus. The microvascular distribution of venules, capillaries, and arterioles obtained following the VAN model proposed by *Boas et al.* (2008) is in line with *Weber et al.* (2008) in macaque V1.

The region modeled is the primary visual cortex of primates because there is extensive literature on histological and functional studies that focus in this region. By considering the regional vascular density, cortical thickness and layer distribution, similar models can be analogously developed for other brain areas. The combined vascular-BOLD model is deterministic and easy to implement. In this work, the static BOLD response is simulated, which makes the model simpler and computationally less demanding. However, as presented here, the model is not applicable to event-related measurements in which the temporal dynamics of blood flow along its draining path have to be considered.

6.4.7   Other approaches to obtain laminar BOLD

A number of approaches for obtaining laminar BOLD signal for GE acquisitions that do not involve the use of a vascular model have been reported. In *Fracasso et al.* (2014) the cortical GE-BOLD profile is separated into a strong linear component, which is assumed to be related to larger veins, and a weak linear component, which is believed to be related to the microvasculature in the laminar network. In *Chen et al.* (2013) the top 40% most activated voxels are removed, as they are considered to be venous voxels, and the laminar GE-BOLD signal is obtained considering only the remaining voxels. Lastly, *Yu et al.* (2012), show direct contributions of microvasculature and macrovasculature to the BOLD signal by measuring at high temporal and spatial resolution in a reduced FOV to investigate feed-forward and feed-back connections in rats.

6.5   Conclusions

This paper describes a model of cortical vasculature that is used to predict the static BOLD response across the cortex following the signal model as proposed by *Uludağ et al.* (2009). The model separates the contribution to the BOLD signal of different vascular compartments to investigate laminar specificity. The simulation predicts that, under equal neurovascular response across the cortex, SE-BOLD signal is highly laminar specific, whereas GE-BOLD signal is less specific as activation in a layer is carried over to layers downstream through intracortical veins. The laminar specificity of the GE-BOLD signal decreases with increasing ICV volume as the cortical surface is approached. The features of the laminar point spread functions, however, are rather similar across layers and could potentially be used in a forward model or deconvolution to extract the laminar BOLD signals free of BOLD signal leakage from layers upstream.

6.6   Acknowledgements

6.7 Supplementary Information
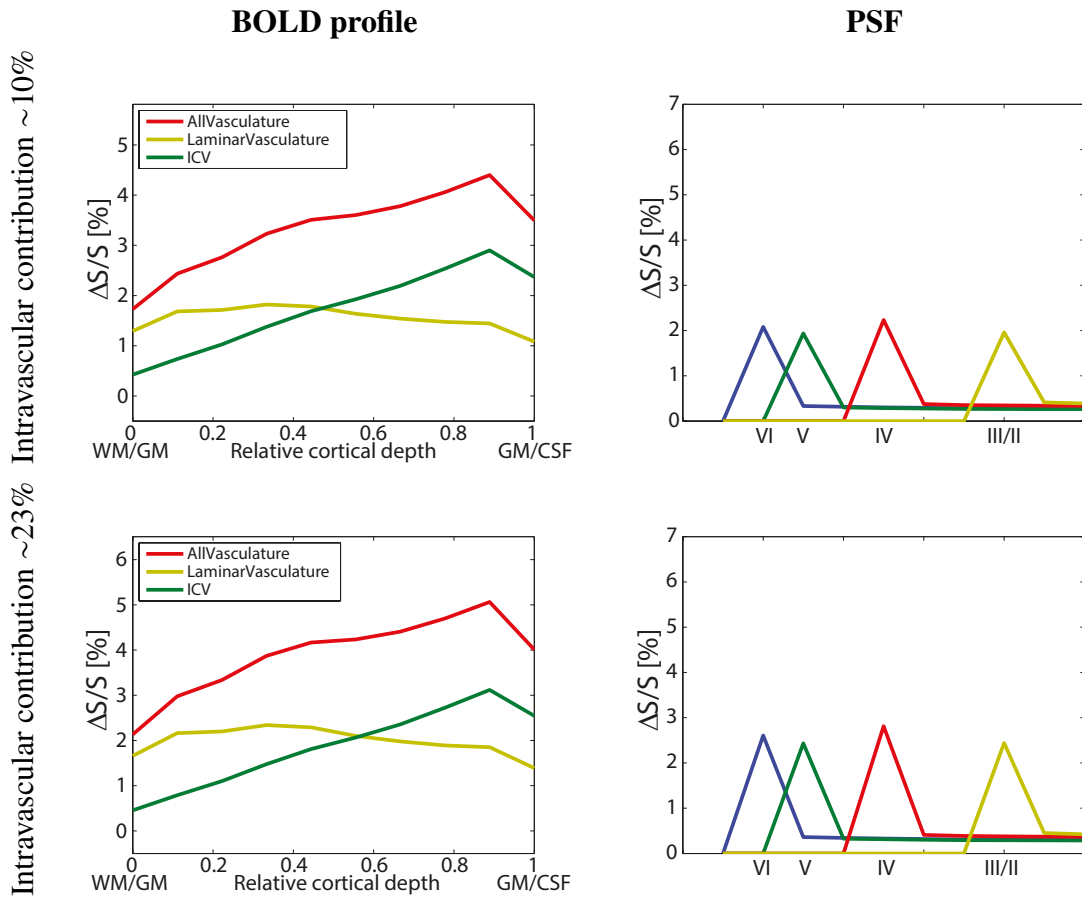
Figure S6.1: GE-BOLD signal profiles (left) and PSF (right) at 7 T for TE=28 ms with an intravascular contribution of ~10% (first row) and ~23% (second row).

Differential paradigms as a means to extract laminar differences in activation with GE-BOLD

The response to a differential paradigm was simulated by predicting BOLD profiles to two conditions:

(A) The strength of the hemodynamic response is equal across the cortex and corresponds to the hemodynamic response used in the simulations in this chapter (i.e. 100% hemodynamic response)

(B) A weaker hemodynamic response in the granular layer than in the agranular layers. Overall, the response is weaker than in condition a) to illustrate differential paradigms in which the average BOLD response is markedly lower in one of the conditions, following *Trampel et al.* (2012). The flow increase in Layers I, II/III, V and VI is 40% of the flow increase experienced in a), whereas in layer IV it is 25%.

The neurovascular coupling is equal in conditions (A) and (B).

The individual BOLD profiles for conditions (A) and (B) and the differential profiles are shown in Figure S6.2. The profiles obtained for the two conditions are normalized to themselves and then subtracted from one another to obtain the differential activation profile. Under the conditions simulated here, the differential profile correctly shows that in the second condition the response in layer IV is weaker compared to the other layers. The differential approach is not quantitative and can have a residual leakage, but it gives a qualitative measure of the relative responses between layers.

Contribution of layers upstream **Laminar and ICV contribution**

$$Differential profile = \frac{Condition(B)}{mean(Condition(B))} - \frac{Condition(A)}{mean(Condition(A))}$$
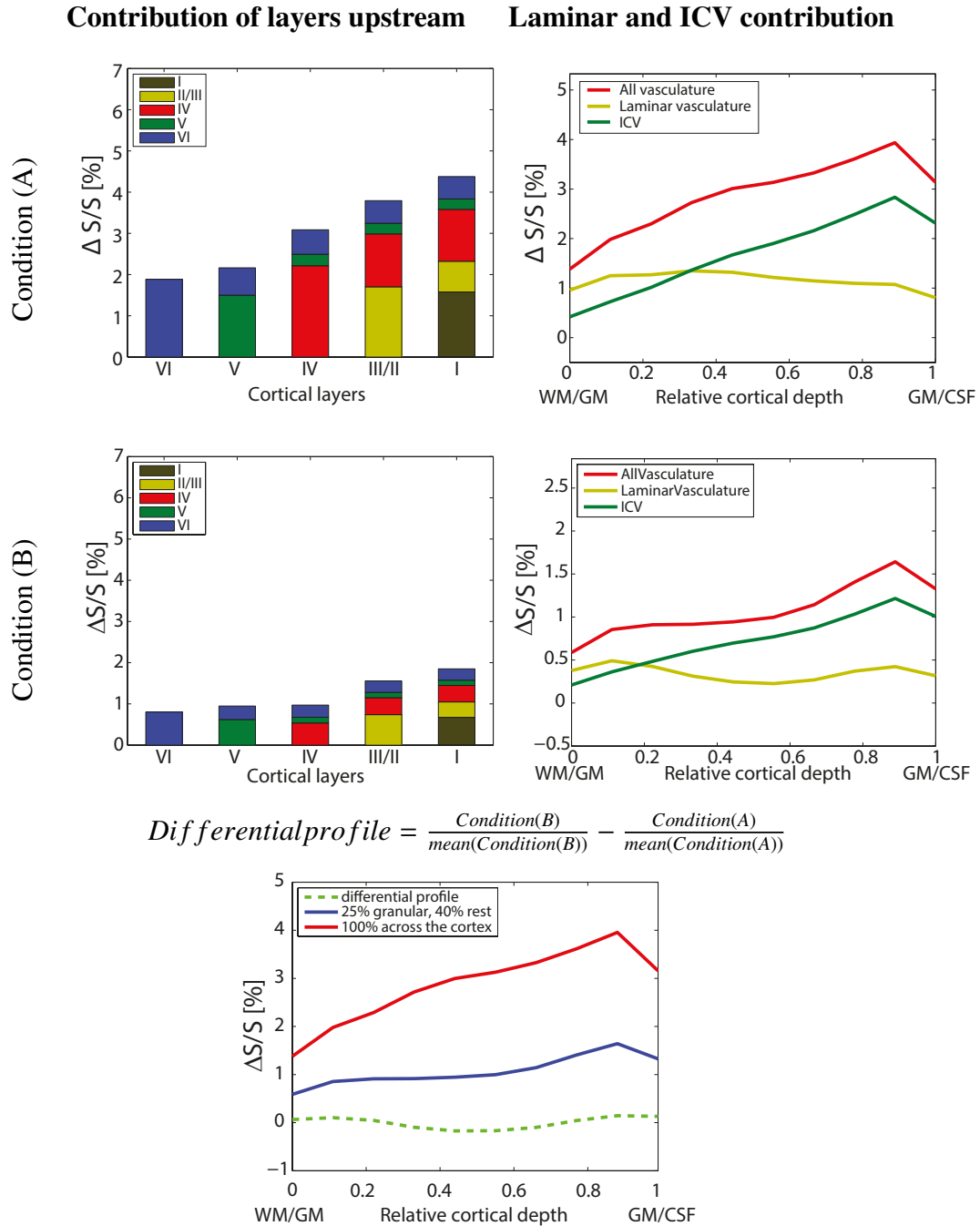
Figure S6.2: GE-BOLD signal profiles for conditions (A) and (B) on the first and second row, respectively, for 7 T and TE=28 ms. The differential activation profile (dotted green line) obtained after subtracting the normalized BOLD signal profiles for condition (A) from condition (B).

Chapter 7

Estimation of Laminar BOLD Activation Profiles using Deconvolution with a Physiological Point Spread Function

Abstract

The laminar specificity of gradient echo (GE)-BOLD activation profiles is degraded by intracortical veins as they drain blood from lower to upper cortical layers, propagating activation signal in the same direction. This work describes a new approach to obtain layer specific profiles by deconvolving the measured profiles using an estimate of the physiological Point Spread Function (PSF). The validity of this post-processing step is first tested on profiles obtained using a multi-echo 3D-FLASH sequence. These profiles are echo time dependent, but the underlying neuronal response is the same over echoes. This feature is exploited to perform a data-based estimation of the PSF. The algorithm can accommodate analysis of variable numbers of cortical layers, and the effect on the profiles of different cortical sampling densities is studied. Lastly, the approach is tested on laminar profiles obtained using the 3D-EPI sequence, which is a more commonly used acquisition method in functional MRI. The deconvolved profiles obtained are similar to spin echo BOLD profiles from the literature. These results suggest that the deconvolution approach successfully removes the effect of signal propagation through intracortical veins. This way, it is possible to obtain profiles with high laminar specificity while benefitting from the higher sensitivity and efficiency of GE-BOLD sequences.

7.1 Introduction

The neo-cortex is divided into six histological layers in most of the regions in the brain. Following the canonical model by *Felleman and Van Essen* (1991), layers within a region are predominantly involved in passing over information from a lower order brain region to a higher order region (feedforward connection), in receiving information from a higher order region (feedback connection), or in connecting areas at the same level (lateral connection). Therefore, detecting neuronal activity at the laminar level is of interest to understand the hierarchical relationship between different brain regions and understand brain function better.

Although some initial attempts have been made using magnetoencephalography (*Bonaiuto et al.*, 2018; *Troebinger et al.*, 2014), functional MRI (fMRI) is to date the most popular technique to measure brain function *in-vivo* at sub-millimeter resolution and obtain cortical depth-resolved activation signals (*Huber et al.*, 2017a; *Uludağ and Blinder*, 2018) and articles therein.

The most widely used method in fMRI measures the Gradient Echo (GE) based blood oxygenation level dependent (BOLD) signal. The advantage of this method is that it has a higher sensitivity to activation and a higher efficiency compared to the other MR methods available for fMRI. The disadvantage is its reduced spatial specificity due to the contribution from large veins (*Boxerman et al.*, 1995). In layer-specific fMRI the spatial specificity of the measured BOLD profile is mainly degraded by the contribution from emerging or intracortical veins. These are the veins that are oriented perpendicular to the pial surface and drain blood uni-directionally from lower layers to upper layers. Therefore, part of the activation signal in a lower layer will propagate or leak into upper layers downstream. This phenomenon will be referred to as the "inter-laminar leakage-problem" in this chapter.

Over the past two decades, the MR community has proposed several ways of dealing with the contamination from large veins. These were originally developed for use in standard-resolution fMRI, but have been applied in high-resolution fMRI studies too. One of these methods consists of combining the standard GE-BOLD method with a differential paradigm (*Cheng et al.*, 2001; *Kashyap et al.*, 2017; *Menon et al.*, 1997; *Sánchez Panchuelo et al.*, 2015). The signal resulting from the subtraction of the condition of interest and the control condition is expected to have a much lower contribution from large veins. Another way of obtaining an activation with little contribution from large veins is to use SE based sequences. The 180° pulse refocuses the extravascular signal in the static dephasing regime, which is the source of the largest contribution in GE-BOLD at 3 T and beyond (*Goense and Logothetis*, 2006; *Harel et al.*, 2006b; *Harmer et al.*, 2012; *Kemper et al.*, 2015; *Yacoub et al.*, 2007, 2009; *Zhao et al.*, 2006). A further BOLD-based

method would be the measurement of the S2 signal of the unbalanced SSFP sequence, which is believed to be dominated by T_2 contrast (*Barth et al.*, 2010; *Ehses et al.*, 2013; *Goa et al.*, 2014). Arterial spin labelling (ASL) has been used to measure changes in the cerebral blood flow (CBF), i.e. the volume of blood that is delivered to a region per unit of time (*Calamante*, 2013; *Ivanov et al.*, 2016). At high spatial resolution, capillaries will contribute the most to changes in blood flow in the cortex and hence this method is expected to have a high laminar specificity. The final method for obtaining an activation signal without venous contribution, that has also been applied in laminar studies, is the measurement of cerebral blood volume (CBV) changes using the vascular space occupancy (VASO) method (*Guidi et al.*, 2016; *Huber et al.*, 2015, 2017b; *Lu et al.*, 2003). The activation signal measured with this method is proportional to the change in vascular blood volume between rest and activation. As the largest portion of blood volume change is located in the capillary bed, this is weighted towards the capillaries and not towards larger vessels.

The methods mentioned above present different specific technical difficulties of their own (e.g. sensitivity to motion, risk of exceeding energy deposition limits at high fields, efficient tagging or inversion of the blood signal . . .). Nonetheless, they all present a lower sensitivity to activation and temporal resolution compared to the standard GE-BOLD based fMRI approach.

This chapter proposes a new method to deal with the inter-laminar leakage problem. It consists of deconvolving the measured GE-BOLD activation profile across the cortex with the spatial physiological point spread function (PSF) of the neuronal activation. As it is not generally possible to measure the PSF in vivo, the PSF estimated in *Markuerkiaga et al.* (2016) using a model of cortical vasculature is used. The strength of this method is that it delivers activation profiles with little inter-laminar leakage while allowing the use of data acquired with the simplest fMRI sequence that has the highest efficiency and sensitivity.

The validity of the approach is assessed on profiles acquired at 7 T that have previously been published. First the approach is tested on the profiles obtained using the multi-echo 3D-FLASH sequence (*Koopmans et al.*, 2011) using the PSF estimated by the model for different sampling densities across the cortex. Due to the sequence used, in this dataset, BOLD profiles are echo dependent, mostly due to the strong TE-dependency of the intravascular venous contribution, but the underlying neuronal state is not. This feature is exploited to perform a data-based estimation of the PSF. Lastly, the approach is validated on the profiles obtained using the 3D-EPI sequence (*Fracasso et al.*, 2017), a sequence more commonly used in functional MRI.

7.2   Materials and methods

7.2.1   Description of the deconvolution approach

This section describes the features of the PSF, the reformulation of the deconvolution as a linear problem and a correction to the physiological PSF proposed here for different cortical sampling densities.

The physiological Point Spread Function

It is not possible to measure the physiological Point Spread Function *in-vivo* in humans due to the difficulty in obtaining the response of a single layer, without simultaneously generating a response in other layers within the region due to inter-laminar connections. Therefore the physiological point spread function estimated in *Markuerkiaga et al.* (2016) using a model of cortical vasculature will be used. In that work, first, a simple model of cortical vasculature based on published histological studies focusing on the primary visual cortex was developed. Thereafter, the well-known BOLD signal model and physiological changes upon activation as described in *Uludağ et al.* (2009) were applied to obtain the positive BOLD response across the cortex. As the simulated neuronal response, the features of the underlying vasculature and the resulting BOLD response were known, it was possible to estimate the physiological Point Spread Function (PSF).

The physiological point spread function of the laminar response in a small region of the cortex will depend on the baseline physiological conditions and the following two factors: the presence and size of emerging veins and the orientation of the cortex with respect to B_0. The physiological PSF estimated in *Markuerkiaga et al.* (2016) applies to the case in which the cortical profiles to be deconvolved are the result of integrating over a convoluted patch of cortex. This implies that the individual profiles that are summed cover a wide range of possible orientations with respect to B_0 and that the integrated profiles contain emerging veins. Baseline physiological conditions will affect the magnitude of the response, but not the shape. In addition, the estimated PSF in that work characterizes the PSF of the steady-state BOLD response. This is the case for stimuli longer than 1 s - when the cortex has reached steady state after the stimulus onset.

The estimated PSF is very similar between layers. It presents a peak in the layer of activation and a rather constant tail towards the pial surface (see Figure 4b in *Markuerkiaga et al.* (2016)). Hence, it can be approximated using two parameters, the peak at the site of activation and the average of the tail downstream towards the pial surface, or, given that the amplitude of the activation is an experimental variable, by a single one, namely, the peak to tail ratio (p2t). Following

Markuerkiaga et al. (2016) a p2t of ∼5.3 was estimated at 7 T for TE=28 ms, using 10 bins across the cortex, and an intravascular contribution to the GE-BOLD signal change of ∼10%.

Deconvolution reformulated as an inverse linear problem

In the steady state, this problem can be described as a simple linear problem $Y = X\beta + \epsilon$, where X is a matrix of shifted PSFs resulting from the underlying laminar BOLD response, β, and ϵ is the error term. Specifically, the elements of the multiplication $Y = X\beta + \epsilon$ are:

$$
\begin{bmatrix} y_1 \\ y_2 \\ \vdots \\ y_n \end{bmatrix} = \begin{bmatrix} peak & 0 & \dots & 0 \\ tail & peak & \ddots & 0 \\ \vdots & \vdots & & 0 \\ tail & tail & \dots & peak \end{bmatrix} \begin{bmatrix} \beta_1 \\ \beta_2 \\ \vdots \\ \beta_n \end{bmatrix} + \begin{bmatrix} \epsilon_1 \\ \epsilon_2 \\ \vdots \\ \epsilon_n \end{bmatrix}
\tag{7.1}
$$

where y_i is the BOLD response as measured at bin i, peak is the peak value of the PSF (BOLD response directly related to the local neuronal response), tail is the tail of the PSF (at a certain bin, the BOLD response resulting from drainage of a deeper cortical layer), β is the underlying laminar response free of inter-laminar leakage and n is the number of bins considered in the analysis. In this chapter, bin refers to each of the sampling points across the cortex, and n is counted, starting at the lowest layer. ϵ is the error term that accounts for a combination of measurement noise and potential deviations of the model from the biophysical system due to the simplifications made.

The peak and tail values will vary between subjects due to the high inter-subject variability of the BOLD response. However, given that the vascular architecture is similar between individuals, their ratio (the peak to tail ratio, p2t) can be expected to show less variance. There are two ways of determining the elements in the mixing matrix X in Equation 7.1. One of the options is to set *peak* = y_1 and *tail* = $y_1/p2t$, in which case the underlying profile of the BOLD response will be normalized to the response in the lowest bin. The other option is to write the matrix as all ones on the diagonal and 1/p2t in the lower diagonal. In this approach, the laminar BOLD profiles will not be normalized and differences in the average magnitude of the profiles between subjects would reflect differences in the average BOLD response between them.

Adjustment to the p2t value for different cortical sampling densities

Following *Markuerkiaga et al.* (2016) a p2t of ∼5.3 is estimated at 7 T for TE=28 ms, 10 bins across the cortex, and an intravascular contribution to the GE-BOLD

signal change of ~10%. If a different number of bins is used, then the p2t has to be adjusted in the following way:

$$p2t = p2t_{model}\frac{n}{n_{model}} + \frac{n_{model} - n}{2n_{model}} \tag{7.2}$$

where n is the number of bins across the cortex in the acquired data and n_{model} is the number of bins used in the model used to estimate $p2t_{model}$. The derivation of Equation 7.2 is shown in section 7.A.

Hence, once the BOLD response across the cortex has been processed and the correct p2t calculated, the underlying laminar activation profile corrected for the leakage from lower layers is easily estimated by solving Equation 7.1 for $\widetilde{\beta} = X^{-1}Y$.

Data based estimation of the physiological PSF

The 3D-FLASH multi-echo dataset obtained an activation profile at each echo time, caused by the same underlying neural response. This feature can be exploited to estimate all the parameters in Equation 7.1 and thus obtain a data-based estimation of the magnitude of the PSF.

For a single echo time, the number of parameters to estimate in Equation 7.1 is the number of cortical bins plus one peak and one tail value. As the number of observations is equal to the number of cortical bins, the system is underdetermined. If a second profile at a different echo time is added to the system of equations, then another set of peak and tail values will have to be estimated. However, if the number of cortical bins is larger than two, the system will be overdetermined and it will be possible to solve it with a data fitting algorithm.

In this work, profiles acquired for two echo times were used to obtain an estimation of the underlying laminar BOLD response, β, and the peak to tail ratio per echo time, as shown in Equation 7.3. As the underlying neural response and hemodynamics do not vary between echo times, it is expected that the profile of the leakage free BOLD response, β, across the cortex will not vary. The magnitude of the leakage-free profile is in principle TE-dependent, but as the peak and tail values are calculated per echo time, any differences in the average magnitude of βacross echo times will lead to a scaling of the corresponding peak and tail values.

$$\begin{bmatrix} \underline{Y}_{TE_1} \\ \underline{Y}_{TE_2} \end{bmatrix} = \begin{bmatrix} \underline{\underline{X}}_{TE_1} \\ \underline{\underline{X}}_{TE_2} \end{bmatrix} \underline{\beta} + \begin{bmatrix} \underline{\epsilon}_{TE_1} \\ \underline{\epsilon}_{TE_2} \end{bmatrix} \tag{7.3}$$

In Equation 7.3 there are 14 parameters to estimate (10 underlying leakage-free BOLD responses β, one per cortical bin, and one peak and one tail value per echo

time) and 20 observations (10 cortical bins for each of the 2 echo times). Least squares non-linear data-fitting using the "Trust region algorithm" as implemented in MATLAB 2017a (The MathWorks, Inc.) was used for parameter estimation. Apart from the description of the system to solve, this solver requires initial values of the parameters for the first iteration, as well as upper and lower boundaries. Lower boundaries were all set to 0 and upper boundaries to 10. Initial parameter values were set in the following way:

- Leakage-free BOLD response, β: values were randomly picked at each cortical bin from a uniform distribution between 0 and 10.

- Peak values: randomly picked for each TE from a uniform distribution between 0 and 10.

- Tail values: the peak value divided by a plausible peak to tail ratio (p2t). This peak to tail ratio was randomly chosen from a uniform distribution between 4 and 8. The choice of this range was made because the p2t estimated in the model was 5.3.

The system is overdetermined and, if a solution exists, there will be many. In this case, as no constraints on the profiles of the βs are set, large values of p2t and very low ones will also be a solution of the system, although they are not physiologically plausible. That is why a loose relationship following physiological expectation was set between the initial values of the peak and tail parameters. In order to avoid that the parameter estimations were strongly biased by the initial parameter values fed to the solver, the estimation was repeated 100 times randomly varying initial values in each of the repetitions as explained earlier. The median of the 100 p2t values calculated using this procedure was considered to be the p2t estimated by this method.

7.2.2 Description of experimental datasets

The multi-echo and ultrahigh-resolution datasets used in this chapter were originally acquired for other purposes and published in *Fracasso et al.* (2017); *Koopmans et al.* (2011). A detailed description of the MR acquisition protocols and the extraction of the cortical activation profiles can be found in the corresponding publications. Here, only the most relevant parameters to understand the nature of the profiles used for the deconvolution are given (see also Table 7.1).

Multi-echo dataset

The 3D-FLASH multi-echo dataset was acquired at 7 T using an isotropic voxel size of 0.75 mm (*Koopmans et al.*, 2011). The stimulus used was a flickering checkerboard covering all of the visual field. Cortical profiles over the activated primary visual cortex (V1) were carefully aligned based on two landmarks, the GM/CSF boundary and the stripe of Gennari, which leads to very clean profiles as shown in Figure 7.1a. The magnitude and shape of the cortical BOLD profile is TE-dependent, whereas the underlying activation is the same across TEs.

The multi-echo dataset was heavily interpolated, it had 100 cortical bins within gray matter. In the current chapter this data was down sampled to 10 cortical bins within gray matter, as that was the cortical sampling in the cortical model used to estimate the physiological PSF. Often, layer specific studies have less cortical bins (*De Martino et al.*, 2015; *Kok et al.*, 2016; *Muckli et al.*, 2015; *Siero et al.*, 2011, 2013; *Trampel et al.*, 2012). In order to test how the approach would work under those conditions, the data was further down sampled to obtain 5 and 3 equally thick cortical bins within the cortex.

Ultrahigh-resolution dataset

The 3D-EPI dataset was acquired at 7 T using a dedicated coil array positioned under the occipital lobe (*Fracasso et al.*, 2017). The response to a checkerboard-like stimulus covering half of the visual field was measured in the ipsilateral and contralateral V1, obtaining a negative and positive BOLD response, respectively. The voxel size was 0.55 mm isotropic. In *Fracasso et al.* (2017) data were divided into profiles presenting a weak, middle or strong linear components (Figure 7.1b shows the profiles of the positive BOLD response for a sample subject). The argument for this parcellation was that at this resolution, some of the profiles will not contain large emerging veins and will therefore be dominated by the laminar response. Such profiles would be expected to have a weaker linear component.

BOLD profiles across the surface were therefore ordered according to how well they fitted a linear trend (Figure 7.1b). The first 40% of the profiles with the weakest linear trend were averaged to obtain the weak linear trend profile. The strongest 30% linear trend were averaged to obtain the strong linear trend and the remaining 30% generated a middle trend. As the p2t value estimated in *Markuerkiaga et al.* (2016) assumed that the profiles were added along the convoluted cortex, the average BOLD response was calculated as shown in Equation 7.4 to test the deconvolution approach and is shown as a thick black line in Figure 7.1b:

$$averageBOLD = 0.4 \cdot WeakLinearProfile$$
$$+ 0.3 \cdot MiddleLinearProfile + 0.3 \cdot StrongLinearProfile \quad (7.4)$$

7.2.3 Data processing

The profile at TE = 27.6 ms in the multi-echo 3D-FLASH dataset, which corresponds to T^*_{2GM} (*Koopmans et al.*, 2011; *Peters et al.*, 2007), was used to calculate the underlying laminar BOLD response. Equation 7.1 was applied using the p2t estimated by the model for that TE, i.e. 5.3. Then, profiles were undersampled to 5 and 3 cortical bins and deconvolved adjusting the p2t value for the number of bins $\neq 10$ following Equation 7.2. Additionally, and exploiting the specific features provided by the multi-echo data, the p2t was estimated as in Equation 7.3, and then used to create new laminar responses to evaluate the robustness of the laminar response to the exact p2t parameters. Lastly, the approach was applied to the ultrahigh-resolution dataset acquired with a more common sequence used in laminar fMRI, namely the 3D-EPI, which had a more conventional repetition time. As *Fracasso et al.* (2017) used 16 bins across the cortex, the p2t estimated by the model was adjusted following Equation 7.2 before solving Equation 7.1 to obtain the underlying laminar response .

7.3 Results

Figure 7.2 shows the deconvolved profiles obtained following Equation 7.1 using the multi-echo dataset. Figure 7.2a was obtained using the laminar profile with 10 bins across the cortex at TE=27.6 ms. Compared to the corresponding profile in Figure 7.1a, in red, the deconvolved profile no longer follows an ascending profile and is rather flat. The individual profiles per subject have been normalized to their average value so that the group average, black line, is not driven by differences in the magnitude of the response. That is why the magnitude is around 1 for all subjects in this Figure. Non-normalized deconvolved responses per subject are shown in Figure S7.1, in the *Supplementary Information.*

The average profile over subjects shows a protuberance towards the middle of the cortex in Figure 7.2a, coinciding with the thalamo-cortical input in the primary visual cortex to the upper layer IV and lower layer III (*Rockland*, 2017). Results of the cortical BOLD responses downsampled to 5 and 3 sampling points across the cortex and deconvolved with the p2t values adjusted accordingly are shown in Figure 7.2b,c. They resemble downsampled versions of the profiles obtained with 10 bins.

Figure 7.3 shows the results obtained for the multi-echo dataset estimating the magnitude of the p2t based on the data. Figure 7.3a shows the distribution of the p2t values obtained over the 100 repetitions for TE=27.6 ms. The minimization algorithm required upper and lower bounds for the estimation of the parameters, which were set to 10 and 0 for all the parameters estimated. Hence the peak and

Multi-echo dataset

(*Koopmans et al.*, 2011)

Ultrahigh resolution dataset

(*Fracasso et al.*, 2017)
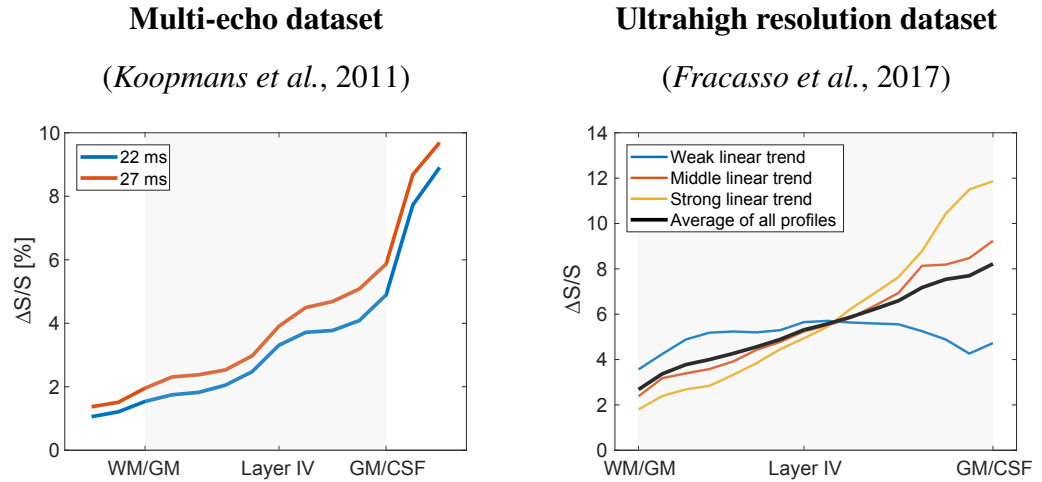
Figure 7.1: GE-BOLD profiles across the cortex that are used to test the deconvolution approach in this chapter. Single subject profiles shown for clarity. The data have been published in the indicated publications. Unless otherwise stated, only data-points within the shaded region have been considered for deconvolution.

	Multi-echo dataset (*Koopmans et al.*, 2011)	**Ultrahigh resolution dataset** (*Fracasso et al.*, 2017)
Voxel size	0.75 mm isotropic	0.55 mm isotropic
Nr of bins	Downsampled to 10 within GM	16 within GM
Sequence	3D-FLASH, multiecho	3D-EPI
Volume TR/ TE	90 s/ 5.7-56 ms	6.5 s/ 27 ms
Visual stimulus	Flickering checkerboard	Semi-field flickering checkerboard
Nr of subjects	5	5 (one of which was scanned twice)

Table 7.1: Relevant acquisition parameters of the sequences used to obtain the GE-BOLD profiles across the cortex that are used to test the deconvolution approach in this chapter.
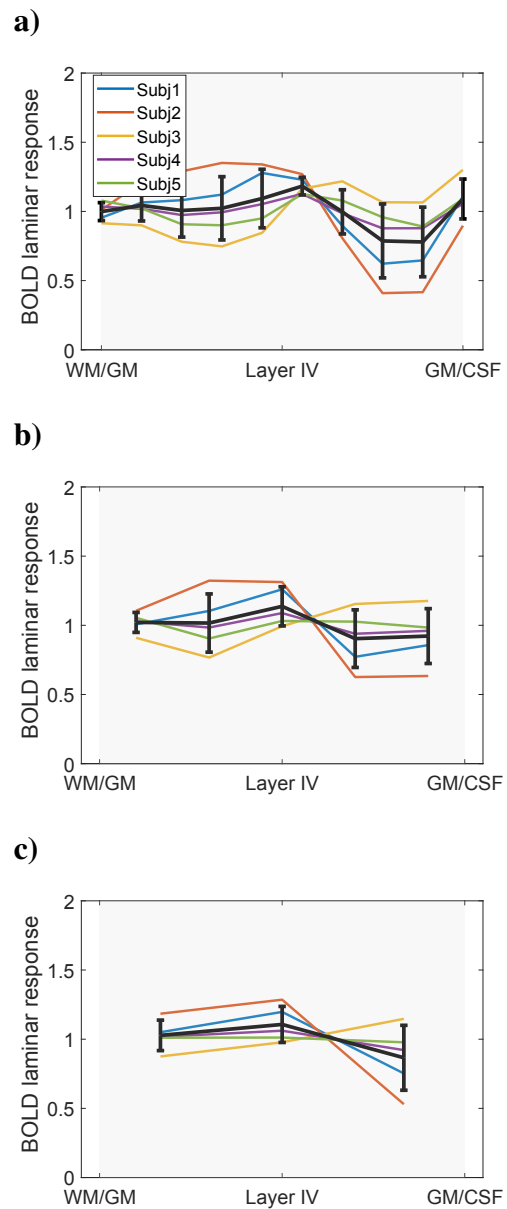
Figure 7.2: Multi-echo profiles downsampled to **a)** 10, **b)** 5 and **c)** 3 cortical bins deconvolved with the corresponding p2t, i.e. 5.3, 2.9 and 1.9, respectively.
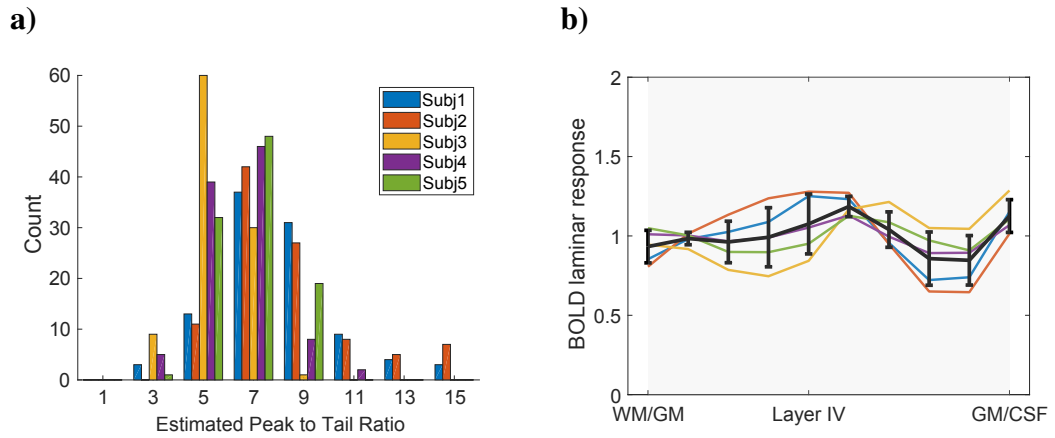
a)

b)

Figure 7.3: **a)** Combined histogram of the peak to tail ratio estimations for 100 repetitions of all subjects for TE=27.6 ms. The average over subjects of the median of the p2t of the repetitions was 6.6±0.9. **b)** Deconvolved profiles obtained using the median of the estimated p2t per subject instead of the p2t value obtained from the model.

tail values that the algorithm will deliver are bounded but the p2t values, the ratio between these, is not.

Therefore, it is encouraging that the obtained p2t are around the values that are expected according to the model. The average over subjects of the median of the 100 repetitions was 6.64 ± 2.3 and 6.57 ± 0.9 for TE=21.9 ms and TE=27.6 ms. The difference between the p2t for these two echo times is smaller than the standard deviation over subjects. Figure 7.3b shows the deconvolved profiles obtained per subject using the subject specific p2t estimated for TE=27.6 ms. These profiles resemble in shape those obtained using p2t=5.3 (directly obtained from the model) shown in Figure 7.2a. The main difference observable is that using subject specific p2t reduces the standard deviation across subjects. This indicates that the approach is not very sensitive to the exact p2t value.

The weighted average of the three profiles presenting a weak, middle and strong linear trend is shown in black for the positive BOLD response of a representative subject of the ultrahigh-resolution dataset in Figure 7.1b. The average for each of the subjects is shown in Figure 7.4a. This dataset was sampled with 16 bins across the cortex, so Figure 7.4b shows the deconvolved profile using the p2t value from the cortical model corrected for the number of bins. The deconvolved profiles no longer show an ascending pattern, showing a light protuberance in the lower layers closely resembling the week linear trend BOLD profiles (Figure 7.4).
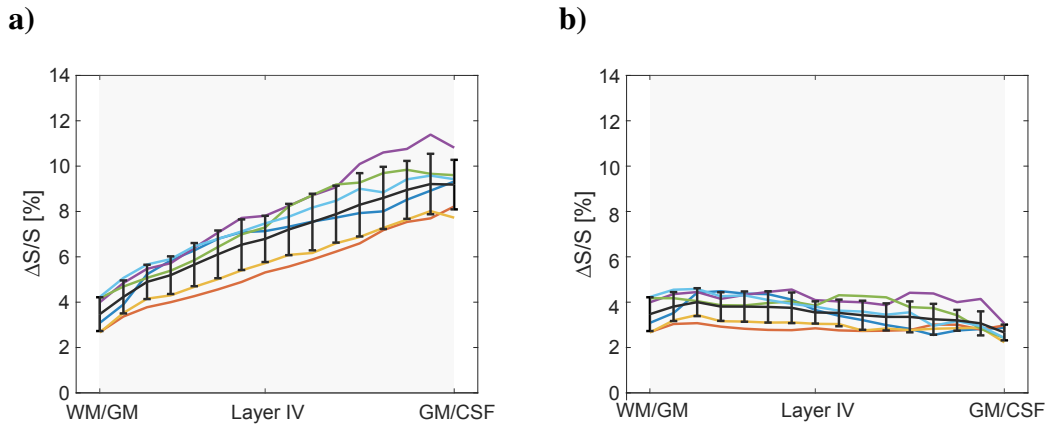
Figure 7.4: **a)** Weighted average profile of the weak, middle and strong linear profiles of the positive BOLD response in *Fracasso et al.* (2017), and **b)** the corresponding deconvolved profiles. The different colours refer to different acquisitions, 5 subjects and one subject acquired twice. The black line shows the average±std across subjects.

7.4 Discussion

The deconvolution of GE-BOLD profiles with the physiological point spread function results in cortical profiles that are similar to those obtained with BOLD based techniques that are less sensitive to the contribution of veins larger than 20 µm in diameter, such as SE and GRASE (*Jin and Kim*, 2008a; *Kemper et al.*, 2015; *Zhao et al.*, 2006). This supports the idea that the deconvolution of GE-BOLD profiles with the PSF is a valid approach to eliminate the inter-laminar signal leakage through intracortical veins and still benefit from the higher efficiency and sensitivity achievable with GE sequences.

7.4.1 Validation of the estimated PSF

The fact that deconvolved profiles are in line with results obtained using approaches with a negligible contribution of emerging veins supports the hypothesis that the physiological point spread function estimated in *Markuerkiaga et al.* (2016) captures the essential features of signal leakage in gradient-echo laminar fMRI.

Similarly, the results in this chapter show that a peak to tail ratio ~5.3 for TE=27.6 ms at 7 T for 10 sampling points across the primary visual cortex adequately describes the biophysical properties of the leakage for the mentioned parameters. Furthermore, the results are largely insensitive to the exact value of the p2t, as the results obtained using the model based or the data-based p2t, ~5.3 and ~6.6,

respectively, are very similar, indicating that a p2t value around these number is valid at 7 T for TE $\sim T^*_{2GM}$ and 10 cortical bins in the primary visual cortex. In addition, for similar echo times, for example 21.9 and 27.6 ms, the data driven estimation of the p2t shows that the variability between subjects is larger than the variability between echo times.

The p2t was estimated in the primary visual cortex for 10 bins across the cortex. In this work it has only been tested in profiles acquired in that region. Assuming that the characteristics of cortical vasculature are comparable across cortical regions, the deconvolution approach will also apply for other regions, but the p2t will need to be adjusted for cortical thicknesses different to that of primary visual cortex. For example, the primary motor cortex, M1, is on average 4 mm thick, whereas the primary visual cortex, V1, is 2 mm thick. Hence, p2t=5.3 will be valid in the motor cortex if it is divided into 20 bins. For a different number of bins across M1, the p2t will have to be adjusted following Equation 7.2.

7.4.2   Deconvolved profiles

The deconvolved profiles are rather flat in all cases. This is expected, as in both datasets the cognitive task that subjects needed to perform was to attend to a visual stimulus that consisted of a full- or semi-field flickering checkerboard. This stimulus is not expected to generate too much input from higher order areas in the primary visual cortex.

The multi-echo profiles tend to show a slight increase just above the middle of the cortex, a point that corresponds to the thalamo-cortical input in the upper layer IV lower layer III as reported in *Rockland* (2017). This small increase is less obvious in the profiles obtained for the positive BOLD response in the high-resolution dataset from *Fracasso et al.* (2017), although the underlying response is expected to be similar between them. A plausible reason for this may be that in the multi-echo dataset the individual profiles were realigned using the stripe of Gennari and the GM/CSF boundary as landmarks. Slight misalignments are likely to blur the small bump and lead to a flatter profile.

In *Fracasso et al.* (2017) individual profiles were grouped in profiles showing a weak, middle or strong linear trend. As the voxel size was 0.55 mm isotropic, it is reasonable to assume that there will be some profiles with little or no contribution from emerging veins. The deconvolved profiles of the positive BOLD response show a strong resemblance to the weak linear trend profiles (see Figure S7.2 in *Supplementary Information*). This is, two processing methods designed to deal with signal leakage through intracortical veins using different approaches deliver similar inter-laminar leakage-free profiles.

The deconvolved profiles of the multi-echo dataset with 10 cortical bins (Figure 7.2a) show a higher BOLD response in the cortical bin closest to the pial surface, although this is not expected as the cell-body density is rather low in layer I (*Shipp*, 2007). A plausible explanation is that pial signal smearing may be confined to the top layer in this dataset. If a parameter reflecting signal smearing is added to Equation 7.3, then the estimated p2t and leakage-free profiles are very similar across the cortex, except for the bin closest to the pial surface, which is no longer higher than the rest (see Figure S7.4 in *Supplementary Information*).

The PSF was estimated considering a positive BOLD response (PBR) following a net excitatory activity across the cortex in *Markuerkiaga et al.* (2016). Inhibitory activity has been shown to give rise to a negative BOLD response (NBR) following a decrease in $CMRO_2$ and CBF compared to baseline (*Boorman et al.*, 2010; *Goense et al.*, 2012; *Shmuel et al.*, 2001, 2006).There is little understanding of the exact effect of inhibitory activity on $CMRO_2$ and CBF, but it is well-known that 80% of the cortical neurons are excitatory neurons and that CBF is strongly driven by excitatory activity (*Buxton et al.*, 2014). Hence, the neurovascular coupling coefficient *n*, (i.e. $n = \frac{\Delta CBF}{\Delta CMRO_2}$) might be similar for the PBR and NBR under comparable conditions (e.g. attention level, caffeine intake, etc). Besides, as shown in Figure 5a in *Markuerkiaga et al.* (2016), the difference in the magnitudes of the p2t ratios for n=2.5 and n= 4 is similar to the standard deviation over subjects of the p2t values given in this chapter. It can hence be expected that the deconvolution approach should be robust within this range of neurovascular coupling coefficients. The deconvolution approach was tested on the NBR profiles shown in *Fracasso et al.* (2017), similar to the PBR case, flatter profiles showing a strong resemblance to the average profile of the weak linear trend were obtained (see Figure S7.3 in the *Supplementary Information*). This suggests that the approach should be able to deal with the case of PBR in some layers and NBR in others, provided that the hemodynamic response to laminar activation is laminar specific, which seems to be the case (*Poplawsky et al.*, 2015, 2017a; *Tian et al.*, 2010; *Yu et al.*, 2014).

7.4.3 Number of bins required to apply the deconvolution approach

The deconvolved profiles using 5 and 3 bins are practically a down sampled version of the profile obtained using 10 bins. In fact, if instead of under sampling to 10 bins, the original profile in *Koopmans et al.* (2011) is sampled using 50 bins and deconvolved with the corrected p2t (see Figure S7.5 in *Supplementary Information*), the profiles are still very similar but the nominal spatial resolution is higher. Hence, as long as profiles are clean and have enough sampling points to characterize them properly, the deconvolution approach corrected for the number of points will deliver good results.

7.4.4   General requirements to apply the deconvolution approach

First, the cortex has to be sampled at regular intervals to apply the deconvolution approach as defined in Equation 7.1. Second, the approach as defined in Equation 7.1 assumes that the response of the cortical vasculature to the stimulus is in steady state and does not apply to transient cases, this will be the case for stimuli longer than 1 s. It a lso assumes that the profiles have been obtained integrating over a sufficiently large and convoluted patch of cortex that contains emerging veins. Third, good segmentation and co-registration are paramount to apply the approach. If the cortical sampling deviates too much from the model due to segmentation problems, the approach will fail.

7.5   Conclusions

The deconvolution approach has been applied to GE-BOLD profiles obtained at 7 T acquired using similar stimuli but different sequences, resolutions and processed with different number of samples across the cortex. The features of the deconvolved profiles obtained are similar to the cortical profiles acquired with SE-BOLD. Using the model based p2t or the data-based p2t delivered remarkably similar results, although the inter-subject variability was slightly reduced when the data-based approach was used. The deconvolution approach seems to be a plausible alternative to obtaining inter-laminar leakage-free profiles, while still benefitting from the higher efficiency and sensitivity of GE-BOLD based functional acquisition methods.

7.6   Acknowledgements

7.A   Derivation of the adjustment of the p2t for different number of bins

Following Equation 7.1 in this chapter, the BOLD response at a given cortical bin is obtained by the following expression:

$$y_i = b_i \cdot peak + \sum_{k=1}^{i-1} b_k \cdot tail$$

The total response across the cortex, A, is obtained by integrating over all bins.

$$A = \sum_i y_i \cdot \Delta x = \sum_i \left(b_i \cdot peak + \sum_{k=1}^{i-1} b_k \cdot tail \right) \Delta x$$

where Δx is the thickness of the bin. For the p2t adjustment sought, without loss of generality, the system can be solved for the specific case in which $b_i = 1, \forall i$. In this case, the expression is simplified to:

$$A = \sum_i^n \left(peak + \sum_{k=1}^{i-1} tail \right) \Delta x$$

As $p2t = \dfrac{peak}{tail}$ and $\Delta x = \dfrac{d}{n}$, where d is the cortical thickness n is the number of bins across the cortex:

$$A = \sum_i^n \left(p2t + \sum_{k=1}^{i-1} 1 \right) tail \cdot \frac{d}{n}$$

$$A = \sum_i^n (p2t + i - 1) \cdot tail \cdot \frac{d}{n}$$

$$A = \left(n \cdot (p2t - 1) + \sum_{i=1}^n i \right) \cdot tail \cdot \frac{d}{n}$$

As $\sum_{i=1}^n i = \dfrac{n \cdot (n+1)}{2}$,

$$A = \left(p2t - 1 + \frac{(n+1)}{2} \right) \cdot tail \cdot d$$

$$A = \left(\frac{2 \cdot p2t + n - 1}{2} \right) \cdot tail \cdot d$$

The p2t depends on the number of bins used, n, but the total BOLD response should be independent of the number of bins. Therefore,

$$A(n_1) = A(n_2)$$

$$\left(\frac{2 \cdot p2t_{n_1} + n_1 - 1}{2} \right) \cdot tail_{n_1} \cdot d = \left(\frac{2 \cdot p2t_{n_2} + n_2 - 1}{2} \right) \cdot tail_{n_2} \cdot d$$

$$(2 \cdot p2t_{n_1} + n_1 - 1) \cdot tail_{n_1} = (2 \cdot p2t_{n_2} + n_2 - 1) \cdot tail_{n_2}$$

$$p2t_{n_1} = \left(\frac{tail_{n_2}}{tail_{n_1}} (2 \cdot p2t_{n_2} + n_2 - 1) + 1 - n_1 \right) \cdot \frac{1}{2}$$

The magnitude of the tail is proportional to the size of the unit element that is being drained. This is inversely proportional to the number of bins used. Hence,

$$\frac{tail_{n_2}}{tail_{n_1}} = \frac{n_1}{n_2}$$

$$p2t_{n_1} = \left(\frac{n_1}{n_2} (2 \cdot p2t_{n_2} + n_2 - 1) + 1 - n_1 \right) \cdot \frac{1}{2}$$

$$p2t_{n_1} = p2t_{n_2} \cdot \frac{n_1}{n_2} + \frac{n_2 - n_1}{2 \cdot n_2}$$

7.7   Supplementary Information

Deconvolved subject profiles in the multi-echo dataset

Figure S7.1 shows the deconvolved profiles obtained by applying Equation 7.1, modified as described below in Equation S7.1. The p2t value obtained from the model in *Markuerkiaga et al.* (2016) for TE= 21.9 ms and 27.6 ms has been used for each of the profiles, p2t = 5.4 and 5.3 respectively. As expected, the profiles obtained in in Figure S7.1 for different TEs differ in the average magnitude of the response, but their shape is similar.

$$
\begin{bmatrix} y_1 \\ y_2 \\ \vdots \\ y_n \end{bmatrix} = \begin{bmatrix} 1 & 0 & \dots & 0 \\ 1/p2t & 1 & \ddots & 0 \\ \vdots & \vdots & & 0 \\ 1/p2t & 1/p2t & \dots & 1 \end{bmatrix} \begin{bmatrix} \beta_1 \\ \beta_2 \\ \vdots \\ \beta_n \end{bmatrix} + \begin{bmatrix} \epsilon_1 \\ \epsilon_2 \\ \vdots \\ \epsilon_n \end{bmatrix} \tag{S7.1}
$$
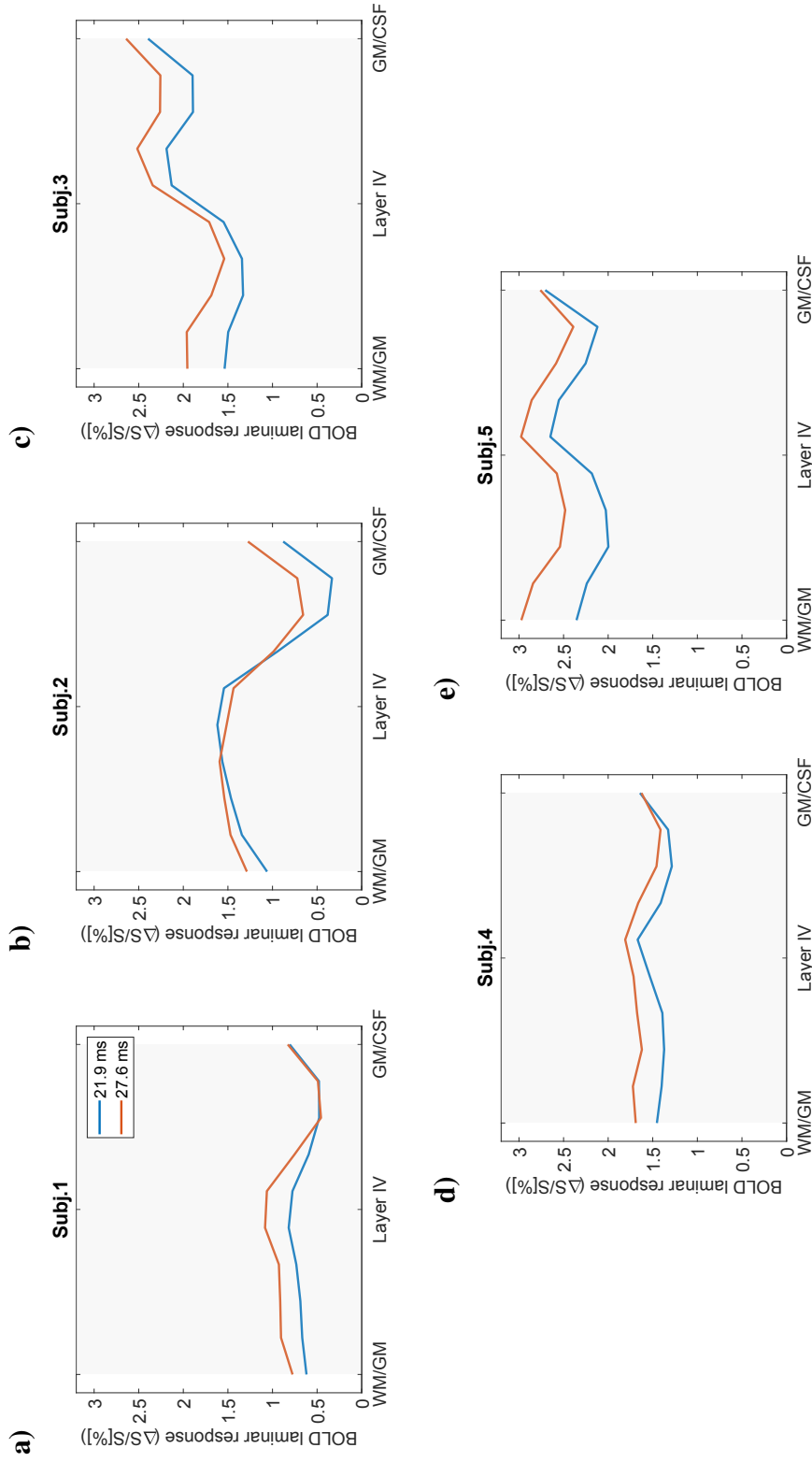
Figure S7.1: Deconvolved laminar BOLD responses per subject obtained for the multi-echo dataset applying Equation S7.1 using the corresponding p2t from the model for two commonly used TEs, graphs **a)** to **e)**. The difference in the magnitude of the profiles between subjects reflects the difference in the average response between subjects.

Deconvolved subject profiles in the ultra-high resolution dataset
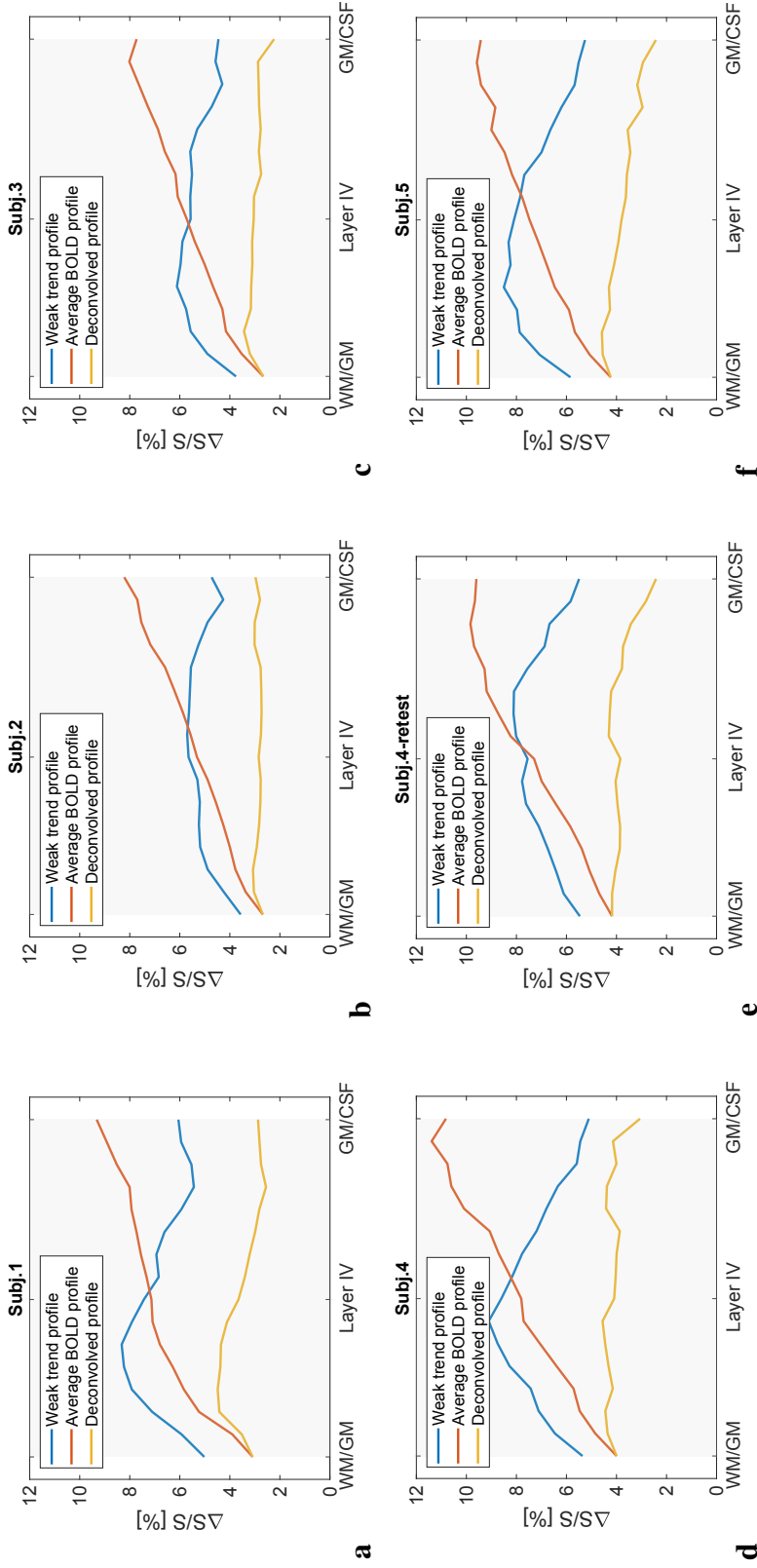
Figure S7.2: Single subject profiles obtained with the ultrahigh-resolution data for each of the 6 measurements (5 subjects, one subject measured twice) for the positive BOLD response. The weakly lineal profile (blue), the average of the weak, middle and strong linear profiles calculated as specified in Equation 7.4 (red) and the average profile deconvolved with the estimate peak to tail ratio (yellow).

Negative BOLD response

a)   b)
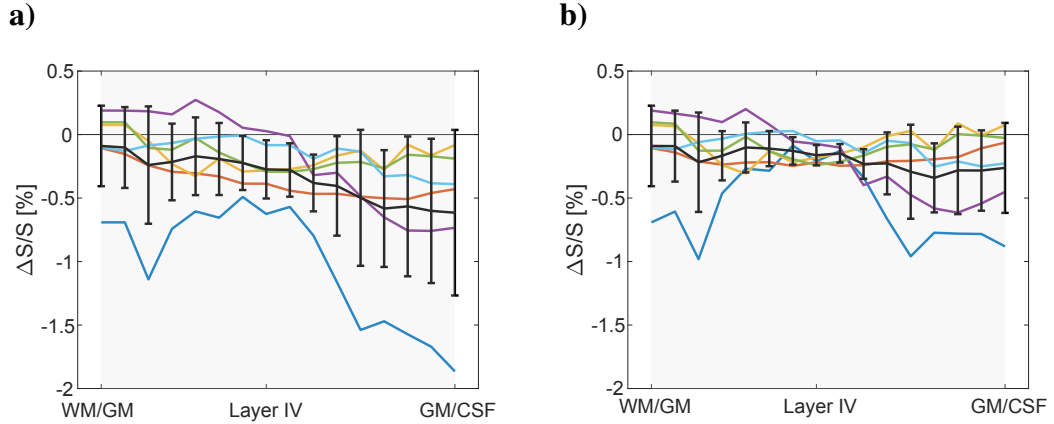
Figure S7.3: **a)** Weighted average profile of the weak, middle and strong linear profiles of the negative BOLD response in *Fracasso et al.* (2017). **b)** the corresponding deconvolved profiles. The different colours refer to different acquisitions, 5 subjects and one subject acquired twice.

Deconvolution accounting for pial contamination in the multi-echo dataset

The deconvolved profiles of the multi-echo dataset with 10 cortical bins (Figure 7.2a) show a higher BOLD response in the cortical bin closest to the pial surface, compared to the preceding sampling point, while this is not the case in the deconvolved profiles in the ultrahigh-resolution dataset. This is not expected considering physiology either, as the cell-body density is rather low in layer I. One reason for this might be that the pial response compared to the average response in GM is stronger in the multi-echo dataset (see Figure 7.1a) compared to other profiles in the literature, presumably due to the profile selection and alignment method. Pial signal smearing into the cortical profile within GM might be sharper in this dataset and manifest itself predominantly in the cortical bin closest to the pial surface. If this is the case, this would lead to an overestimation of the laminar BOLD response in that bin.

In order to test this, the p2t and deconvolved profiles were estimated again using the multi-echo dataset and an extended version of Equation 7.3 that accounted for partial volume with the pial surface (see Equation S7.2). The results are shown in Figure S7.4 below.

$$
\begin{bmatrix} y_1 \\ y_2 \\ \vdots \\ y_8 \\ y_9 \\ y_{10} \\ y_{11} \end{bmatrix} = \begin{bmatrix} peak & 0 & \dots & 0 \\ tail & peak & \ddots & 0 \\ \vdots & \vdots & & 0 \\ tail & tail & \dots & 0 \\ tail & tail & \dots & 0 \\ tail & tail & \dots & peak \end{bmatrix} \begin{bmatrix} \beta_1 \\ \beta_2 \\ \vdots \\ \beta_8 \\ \beta_9 \\ \beta_{10} \end{bmatrix} + \begin{bmatrix} 0 \\ 0 \\ \vdots \\ \alpha^3 \cdot pial \\ \alpha^2 \cdot pial \\ \alpha \cdot pial \\ pial \end{bmatrix} + \begin{bmatrix} \epsilon_1 \\ \epsilon_2 \\ \vdots \\ \epsilon_8 \\ \epsilon_9 \\ \epsilon_{10} \\ \epsilon_{11} \end{bmatrix} \quad \text{(S7.2)}
$$

a)

b)

Partial volume factor $\alpha = 0.12$
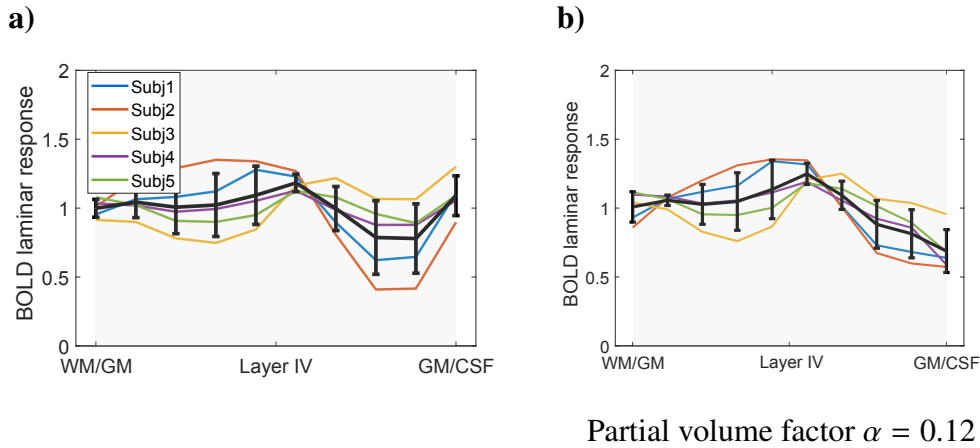
Figure S7.4: **a)** Profiles obtained using the approach that does not consider pial con-tamination within the cortex, as defined in the body of the chapter. **b)** Laminar response obtained using the method described above in Equation S7.2, which includes the par-tial volume factor, α, to account for partial volume between the pial surface and the parenchyma. The magnitude of the partial volume factor is not universal, as it depends on the acquisition and processing method used.

Deconvolution results for higher sampling densities

a)   b)
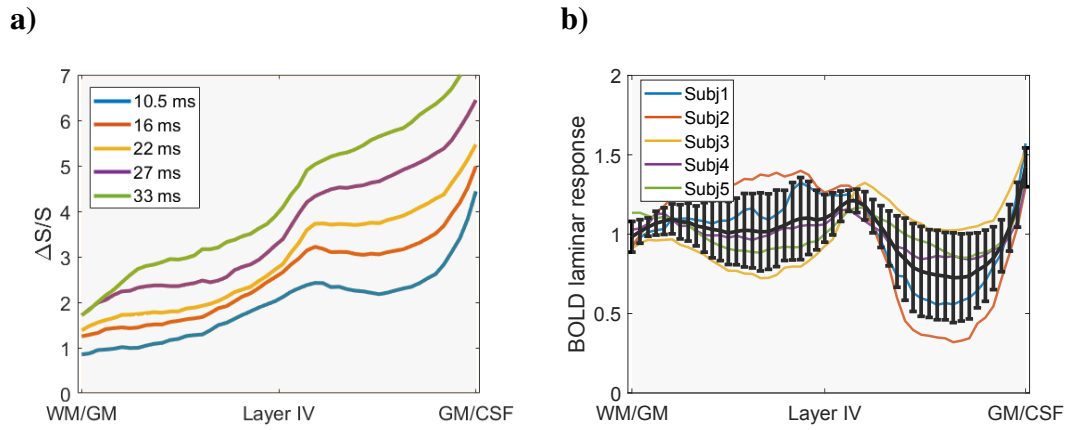
Figure S7.5: **a)** Multi-echo profiles for different TEs for the same subject as that shown in Figure 7.1 but sampled using 50 bins instead of with 10 bins, and **b)**, corresponding deconvolved profiles for all subjects using the model p2t value adjusted accordingly.

Chapter 8

High resolution BOLD-fMRI using S2-SSFP at 7 T

Abstract

The S2-SSFP signal gives a T_2-like contrast, without the high-power deposition associated with spin-echo experiments at high static field strengths. As the T_2 of blood is considerably shorter than the T_2 of the parenchyma at 7 T, functional contrast can be expected to be dominated by extravascular signal changes around microvasculature under the correct experimental conditions. Hence, this sequence might be a good candidate to obtain highly laminar specific BOLD activation profiles at 7 T. To test this, S2-SSFP laminar activation profiles in response to a visual stimulus are acquired. Data were obtained at 7 T with 0.75 mm isotropic resolution and the sequence parameters were optimized to maximize signal change upon activation (TR/TE= 13.4/7.14 ms) according to previous simulation. The cortical profiles showed an ascending pattern that peaks towards the superficial layers. The experiments were simulated using a model of cortical vasculature where the S2-SSFP signal was approximated as that arising from pairs of consecutive RF pulses. The simulation results show that for the parameters used there is a considerable intravascular contribution and an extravascular contribution in the static dephasing regime that leads to ascending activation profiles. Hence, the S2-SSFP sequence may only be well-suited to obtain T_2-like laminar activation profiles at prohibitively long TR-values.

8.1   Introduction

Cortical grey matter is on average ~3 mm thick and in most areas of the neo-cortex it is divided into 6 cytoarchitectonically distinct layers. Following *Felleman and Van Essen* (1991), these layers have a specific role in the feed-forward and feed-back connections between brain regions. Therefore, there is an interest among neuroscientist to measure functional activation at the laminar level in order to distinguish between these two processes, and the interactions between them (*Lawrence et al.*, 2017). T_2-weighted, spin echo (SE) BOLD functional activation signal is considered to be well suited for laminar applications because, if the TE is sufficiently long that intravascular BOLD contributions can be neglected, then the contrast should arise solely from extravascular dynamic averaging, which is better localized to the underlying neuronal activity (*Ogawa et al.*, 1993).

However, SE acquisitions with whole brain coverage and/or high spatial resolution might hit Specific Absorption Rate (SAR) limits, particularly at 7 T and above, because energy deposition by the RF pulse increases approximately quadratically with B_0. Furthermore, SE sequences are often combined with an echo-planar image (EPI) encoding scheme in order to shorten the acquisition time and keep the sequence suitable for acquisitions measuring brain function. This can lead to distortion artefacts in regions of poor field homogeneity and reduces the laminar specificity of the measured signal due to T_2' contribution during signal read-out that will increase the contribution from intracortical veins (*Goense and Logothetis*, 2006). Slice multiplexing combined with PINS pulses (*Norris et al.*, 2011) and parallel transmit (*Zelinski et al.*, 2009) can alleviate the SAR problem, whereas parallel transmit can also be used to reduce distortions (*Setsompop et al.*, 2009).

Another way of measuring T_2-like contrast is measuring the S2-SSFP signal (Steady State Free Precession) (*Gyngell*, 1988). The S2-SSFP signal is composed of the spin echo that results from the last two RF pulses and the stimulated echoes from the previous pulses. Hence, it is dominated by T_2-like contrast. The S2-SSFP sequence will be slower than the SE-EPI sequence but will not hit SAR limits and will not suffer from distortion artefacts.

This study builds on previous work by (*Barth et al.*, 2010), which acquired only the S2 signal using a low spatial resolution, and (*Goa et al.*, 2014) which acquired both S1 and S2 signals at high spatial resolution. In this work the same spatial resolution as in (*Goa et al.*, 2014) is used, but only the S2 signal is acquired, reducing the demands on the gradients and increasing the image SNR. In addition, sequence parameters have been chosen to maximise signal change in the parenchyma upon neuronal activation on the basis that the functional signal change observed is caused solely by T_2 changes in grey matter (*Barth et al.*, 2010). This assumption was made as venous blood at 7 T was assumed to have

a very short T_2 relaxation time (*Lee et al.*, 1999; *Yacoub et al.*, 2003). By only acquiring the S2-signal the sensitivity to motion is reduced, as the gradient switching required to acquire the S1-signals is eliminated, and the TR can be chosen to correspond to the theoretical optimum.

Although S2-SSFP generates images that are highly similar to T_2-weighted ones, it is not clear what the relative contribution of the different BOLD contrast mechanisms to the functional signal change is in SSFP. It is also notoriously difficult to tease apart the relative contributions of these contrast mechanisms to the total BOLD signal (*Hoogenraad et al.*, 2001; *Jochimsen et al.*, 2004) but the combination of laminar profiles with a model approximating the underlying signal changes (*Markuerkiaga et al.*, 2016) can offer additional insight. Ideally, the S2-SSFP functional signal change would be dominated by the extra-vascular dynamic averaging contribution. In this work we test whether this is the situation in practice, allowing us to draw firm conclusions on the value of this contrast for fMRI in general, and laminar fMRI in particular.

8.2   Materials and methods

10 healthy volunteers (7 female, 28.8±7.7 years old) were scanned at a 7 T scanner (Magneton, Siemens Healthcare, Erlangen, Germany) using a single channel transmit / 32-channel receive radiofrequency (RF) head coil (Nova Medical Inc., Wilmington, USA). All participants gave written informed consent according to the guidelines of the local ethics committee before the scan.

8.2.1   Data acquisition

The session protocol consisted of a high-resolution anatomical scan, a low-resolution functional localizer and a high-resolution SSFP functional sequence. The functional localizer was processed online and the activation map obtained was used to position the thin imaging slab of the SSFP high-resolution functional scan covering as much as possible of the region responding to the stimulus.

The whole brain, high resolution, T_1-weighted anatomical scan was acquired using the MP2RAGE sequence. The relevant parameters of this sequence were: TI1/TI2/TR= 600/2700/6000 ms, FA1/FA2=4/5°, echo spacing=7.2 ms, BW=240 Hz/pixel, 3-fold in-plane GRAPPA acceleration, 6/8 partial Fourier acceleration in the phase and slice directions and a 0.75 mm isotropic voxel size.

The functional localizer was acquired using a 2D-EPI sequence with TR/TE=3000/30 ms, FA=90°, 2 mm isotropic voxel size. The imaging slab was 66 mm thick and was oriented parallel to the calcarine sulcus, generously covering the entire occipital lobe. 60 measurements were acquired while the subject attended to the same stimulus as the one that was used in the high-resolution functional scan. The paradigm in the functional localizer was 15 seconds of grey screen with a fixation cross, followed by 3 seconds of a circular flickering checkerboard (8 Hz).

The high resolution functional scan was acquired using a 3D S2-SSFP acquisition sequence. Gradient spoiling in the read-out direction of 2π/pixel was added on top of the read-out dephasing lobe to prevent any S1 signal leaking into the acquired S2 signal. The field of view was 192x144x16.5 mm^3 and the voxel size was 0.75 mm isotropic. The imaging slab was oriented obliquely covering as much as possible of the activated region as measured with the functional localizer. The flip angle was FA=23° and TR/TE = 13.4/7.14 ms which implies an effective TE for the S2-SSFP signal of TE$_{eff}$ = 2xTR-TE = 19.66 ms. Other sequence parameters were: bandwidth =115 Hz/pixel, readout time= 8.8 ms, 3-fold in-plane GRAPPA acceleration, volume TR=30.5 s. The stimulus paradigm consisted of alternating the grey screen and circular flickering checkerboard described above. The same condition was sustained during the acquisition of a functional volume and participants were asked to stare at the fixation cross throughout the experiment. 30 volumes were acquired.

8.2.2   Data processing

Motion correction and co-registration

First, the outer slices at the edges of the 3D functional slab were discarded due to imperfections of the slab profile. The skull was removed using FSL-BET (*Smith*, 2002) and a bias field correction was performed (*Zhang et al.*, 2001). Motion correction was carried out in AFNI (*Cox*, 1996) using a linearised weighted least squares algorithm (two passes, zero padded, 7th order polynomial interpolation), realigning all volumes to the first one, and high-pass filtered with $f_c = 1/(2.1 \times volTR)$. Due to the very thin slab, some of the slices close to the edges suffered from lower or uneven signal intensity in the signal time course due to the interpolation when transforming the volume according to the motion correction parameters. These slices were removed before further processing. The anatomical volume was co-registered to the first functional scan using the boundary based registration method implemented in FreeSurfer (*Greve and Fischl*, 2009).

Cortical sampling

Following the approach used in *Polimeni et al.* (2010), the white matter surface generated in FreeSurfer was expanded (*Dale et al.*, 1999) by 10% of the cortical depth at each vertex to sample the functional volume (15 sampling points across the cortex: 2 points in white matter, 11 points in the cortex and 2 points in the CSF). To avoid areas of poor grey matter segmentation, vertices in V1 areas with an estimated cortical thickness larger than 2.5 mm were discarded from further analysis.

Cortical activation profiles

First, the motion corrected high-resolution functional data were processed applying the General Linear Model as implemented in FSL-FEAT to obtain a mask of the voxels that responded to the stimulus. The functional data were spatially smoothed using a 3 mm Gaussian kernel to gain sensitivity and voxels with a z-score>3 were included in the mask. The surface boundaries obtained in FreeSurfer were overlaid onto the activation maps and vertices coincident with activated voxels were identified. The unsmoothed high-resolution functional volumes were sampled at the identified vertices across the cortical depth and the average of the individual profiles was computed to obtain cortical profiles in the hemisphere.

In S2-SSFP images CSF appears much brighter than grey matter and the boundary between the two structures is easily identified. As done in *Goa et al.* (2014), this feature was exploited to compensate for small-scale coregistration errors and to obtain well aligned individual profiles. For each profile, the CSF/GM boundary was identified as the maximum gradient in the SSFP profile and for all profiles these pointes were aligned. Only profiles where this maximum gradient was within the 10% of the profile closest to the GM/CSF surface, as defined by the FreeSurfer segmentation, were included. After realignment, the signal change, ΔS, was calculated as the difference of the average profile between the activated and resting conditions: $\Delta S = \overline{S_{act}} - \overline{S_{rest}}$.

8.2.3 Simulation of cortical profiles

In order to investigate the BOLD contrast mechanisms that underlie the activation profiles measured using the SSFP sequence, cortical profiles were simulated following the model of cortical vasculature proposed in *Markuerkiaga et al.* (2016). This model captures the vascular differences across the cortex by considering the distribution of the extravascular and intravascular spaces and the type of vessels present as a function of cortical depth. For the simulations in this work, the model was extended to include a pial vein of $\varnothing = 200$ μm on the cortical surface. The

voxel in which the pial vein is located is a 0.75 mm isotropic vessel and half of the extravascular space is GM and the other half is CSF.

The resulting vascular distribution is shown Figure S8.1 in the *Supplementary Information*. The microvascular density is around 2.3% and shows a rather flat profile, with a peak towards the middle of the cortex. The density of intracortical veins, which are all larger than 20 μm in diameter, increases steadily from lower layers to upper layers and is always smaller than the microvascular density, with a maximum in the most superficial layer around 1.3%. The vein simulated on the pial surface takes up 5.6% of the volume of the 0.75 isotropic voxel. The BOLD signal at each voxel/cortical depth is simulated as a volume weighted sum of the intravascular and extravascular compartments based on the corresponding relaxation times at 7 T as given in *Uludağ et al.* (2009):

$$S_{Tot} = (1 - CBV) \cdot S_{ex} + \sum_i CBV_i \cdot S_{in,i} \tag{8.1}$$

where *CBV* is the percentage of cerebrovascular volume in the voxel, *i* refers to each of the vascular compartments in the voxel and S_{ex} and S_{in} are the extravascular and intravascular signals that are given by $S = S_0 \times e^{-TE/T_2^{(*)}}$, where the $T_2^{(*)}$ is compartment specific.

Uludağ et al. (2009) provide analytical expressions on how the intravascular and extravascular relaxation times T_2 and T_2^* vary with field strength and blood oxygenation level for blood and grey matter. In this chapter, the relaxation rate of CSF for simulating the pial surface was obtained as the sum of the intrinsic R_2, $R_{2CSF,0}$, and the blood oxygenation induced changes in the extravasculature, $R_{2CSF,Y}$, i.e. $R_{2CSF}^{(*)} = R_{2CSF,0} + R_{2CSF,Y}^{(*)}$. $R_{2CSF,0}$ was set to R_2 values reported in the literature for CSF, 8 s^{-1} (i.e. $T_{2CSF} = 125$ ms as reported in *Crémillieux et al.* (1998)). $R_{2CSF,Y}^{(*)}$ was calculated using the parameters given for the extravascular static dephasing in *Uludağ et al.* (2009). For typical TEs used in fMRI, spins around veins ∅>20 μm will diffuse in the static dephasing regime in grey matter. The diffusion coefficient is 3-4 times larger in CSF compared to grey matter. As the simulated vein has ∅ =200 μm, it is safe to assume that spins will diffuse in the static dephasing regime around it and to use the coefficients calculated for this regime in the mentioned paper by Uludağ.

In this work, the response to the equal net excitatory neuronal activity and neurovascular coupling across the cortex was simulated. The hemodynamic parameters used were taken from *Uludağ et al.* (2009); the relaxation times in the resting and activated conditions are given in Table 8.1 and all compartments across the vascular tree increased their volume by 16% upon activation, except for veins with ∅ > 20 μm, which were not considered to dilate. To a first approximation, the S2-SSFP signal can be considered to be dominated by the shortest echo pathway. In

this case, the magnitude of the S2 signal is estimated as the magnitude of a T_2 decay at the effective echo time of the sequence (2xTR-TE) multiplied by the T_2' weighting due to the fact that the S2 signal has to be acquired earlier than the echo, as this coincides with the RF pulse.

$$S_2 = S_0 \cdot e^{-TE_{eff}/T_2} \cdot e^{-TE/T_2'} \qquad (8.2)$$

where TE is the echo time, TE_{eff} is the effective echo time of the SSFP signal acquisition, $T_2^{(\prime)}$ is the transversal relaxation time and S_0 is the spin density of the extrapolated signal at TE=0. T_2 was estimated following *Uludağ et al.* (2009), whereas T_2' was calculated following the analytical expressions in the same article as $T_2' = 1/(1/T_2^* - 1/T_2)$. The SSFP profiles were simulated for TE=7 ms and TE$_{eff}$=19.66 ms, corresponding to the echo times of the experimental SSFP profiles in this study.

	T_2 [ms]		T_2^* [ms]	
	Rest	Activation	Rest	Activation
Grey matter	46.7	47.6	27.5	28.4
Venous blood (Y_{rest}=0.6)	8.5	13.4	0	0
Capillary blood (Y_{rest}=0.75)	20	30.7	0	0
CSF	118.4	121.4	41.1	51.6

Table 8.1: Relaxation times of the different compartments in the middle of the cortex used in the simulation. The compartments that correspond to the cortex (grey matter and vascular compartments) have been obtained from *Uludağ et al.* (2009) and references therein. The relaxation time of CSF was obtained from *Crémillieux et al.* (1998) and the dephasing in the CSF around the pial vein ($\varnothing$=200 μm) was taken from *Uludağ et al.* (2009).

The extravascular contributions to the BOLD signal were divided into contributions in the dynamic averaging regime (related to T_2) and in the static dephasing regime (related to T_2'). To the authors' knowledge, the T_2^* of blood and its dependency with blood oxygenation has not been described in the literature for 7 T, so the intravascular contribution is not presented divided into the static and dynamic averaging regimes. The contributions are obtained in the following way:

$$S_{ex,dynamic} = (1 - CBV) \cdot e^{-TE_{eff}/T_{2,ex}}$$

$$S_{ex,static} = (1 - CBV) \cdot e^{-TE_{eff}/T_{2,ex}} \cdot e^{-TE/T'_{2,ex}} - S_{ex,dynamic} \qquad (8.3)$$

$$S_{in} = \sum_i CBV_i \cdot e^{-TE_{eff}/T_{2,in_i}}$$

In the vascular model, the cortical depth is divided into 10 voxels with a size of 0.75x0.75x0.25 mm^3, where the shortest side is along the cortical depth. The voxel size in the SSFP acquisition was 0.75 mm isotropic. In order to obtain more realistic profiles, the simulation profiles were smoothed with a convolution kernel expanding 3 voxels, as previously described (*Markuerkiaga et al.*, 2016).

The effect of the TE and TE$_{eff}$ on the profiles and the laminar specificity of the signal was studied for a range of values. The degree of T'_2 weighting was studied by varying the TE for the fixed TE$_{eff}$ =19.66 ms. Then the laminar specificity of a range of TE (TE=0,1,3,5,7 ms) and TE$_{eff}$ (TE$_{eff}$=20,30,40,50,60 ms) was studied by calculating the peak to tail ratio (p2t). This metric was introduced in *Markuerkiaga et al.* (2016), where it was shown that the physiological point spread function of a layer specific activation can be approximated as a peak at the layer of activation followed by a rather constant tail towards the cortical surface. The p2t is the ratio between the laminar peak and the average of the tail.

8.3   Results

8.3.1   Experimental SSFP profiles

The image quality of the SSFP volumes was good and no geometric distortions were visible with the bandwidth used (150Hz/pixel). One subject's data had to be discarded due to excessive motion during image acquisition. Figure 8.1 shows the BOLD signal change upon activation measured after realigning the individual profiles to the GM/CSF boundary for the remaining nine subjects. The profiles show an ascending curve that peaks in the upper layers or the pial surface.
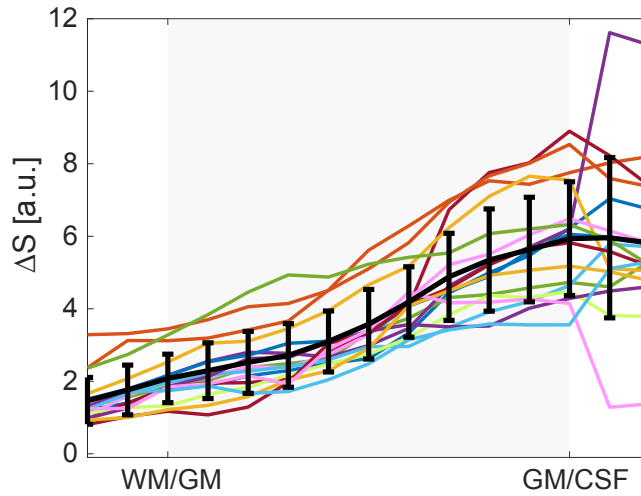
Figure 8.1: Signal change upon activation across the cortex obtained using the SSFP sequence with an effective TE=19.66 ms per subject and hemisphere. Each colour corresponds to one subject and hemisphere.

8.3.2 Simulated SSFP profiles

Figure 8.2 shows the simulated SSFP profiles broken down into the underlying contrast mechanisms that can contribute to the BOLD signal. The intravascular and extravascular dynamic contributions are rather flat across the cortex, reflecting the microvascular density, whereas the extravascular static dephasing steadily increases towards the cortical surface, following the vascular density of intracortical veins. Within the cortex, the intravascular and extravascular contributions are similar, especially in lower layers. On the pial surface, however, the extravascular static dephasing is clearly the dominating contrast mechanism and contributes to almost 70% of the BOLD signal change, when a pial vessel with $\varnothing$=200 μm is simulated.

Figure 8.3a shows that the steepness of the activation profile increases with increasing TE due to increased T_2' weighting across the cortex. This is most notorious on the pial surface around large veins. The peak to tail ratio (p2t) decreases with increasing TE, i.e. with increasing contribution in the static dephasing regime, because the increase in the contribution from intracortical veins is larger than that from the laminar vasculature (Figure 8.3b). Regarding the dependence on the effective echo time, the p2t increases with increasing TE_{eff}. Focusing on the curve with no T_2' weighting (TE=0), shown in blue, this increase of the p2t can be explained by the fact that the relative contribution of the dynamic dephasing around microvasculature with respect to the intravascular contribution increases with increasing TE_{eff}. P2t increases more rapidly by reducing the TE than by increasing TE_{eff}.
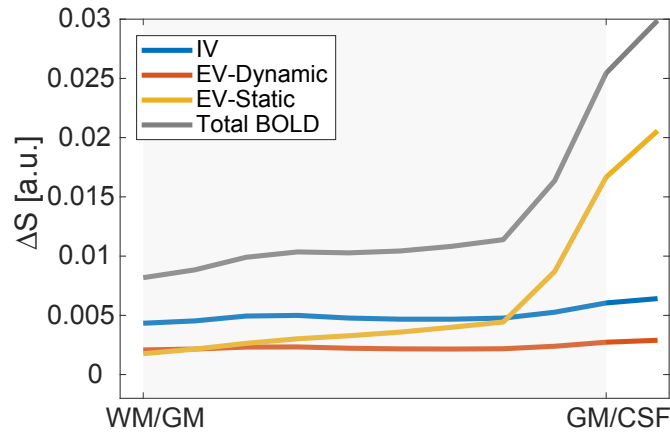
Figure 8.2: Cortical activation profiles simulated for SSFP based on the vascular model presented in *Markuerkiaga et al.* (2016). The effective echo time is 19.66 ms and the sequence TE is 7 ms. The SSFP signal is approximated as the echo arising from the shortest pathway (see Equation 8.2). The contribution to the BOLD signal change of the intravascular and extravascular compartments, shown in colour, were obtained following Equation 8.3.

a)   **b)**
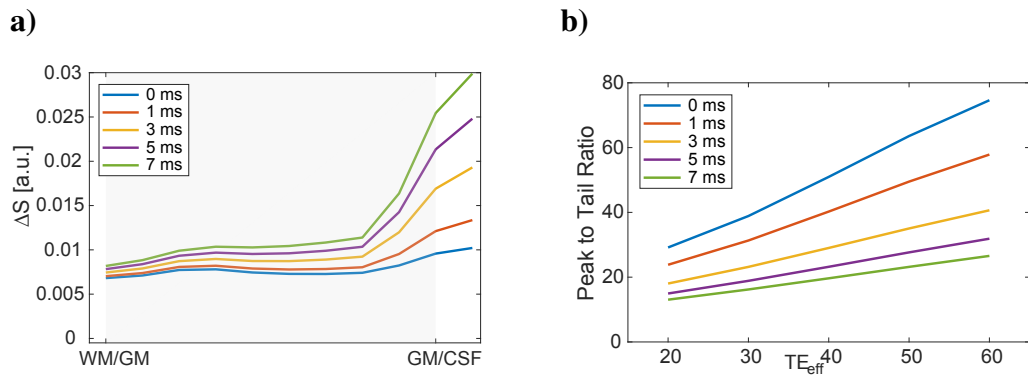
Figure 8.3: **a)** Simulated SSFP activation profiles for 5 different TEs between 0 and 7 ms. The effective TE was 19.66 ms for all curves. **b)** The peak to tail ratio as a function of effective TE (TE_{eff}) for the same sequence TEs as in graph a).

8.4   Discussion

8.4.1   General conclusion and expectation of profile for T_2-contrast

The purpose of this work was to explore the underlying contrast of S2-SSFP and its utility for obtaining laminar activation profiles. The strength of activation in-

creased steadily from lower layers to upper layers (Figure 8.1). The checkerboard stimulus used is not expected to lead to a strong feedback to the upper layers and the microvascular density, if anything, is lower in the upper layers. Hence, in the absence of intravascular contribution, activation profiles dominated by extravascular T_2 contrast are not expected to show a maximum in the upper layers when this stimulus is used. This implies that the measured S2-SSFP signal has contributions from additional contrast mechanisms.

8.4.2 Contribution of the BOLD contrast mechanisms to the cortical activation profiles

The cortical vascular model was used to simulate the activation profiles to tease apart the mechanisms contributing to the measured S2-SSFP profiles. The simulation results in Figure 8.2 show that, at TE_{eff}=19.66 ms and TE=7 ms, the largest contribution to the BOLD signal change comes from the intravascular compartment. However, the profile of the intravascular contribution is not strongly ascending within the parenchyma as it is dominated by the microvascular contribution. The slightly ascending profile of the total BOLD signal change within the cortex is the result of the static extravascular contribution that arises from intracortical veins.

The strong signal change on the pial surface is, as opposed to the signal in the parenchyma, dominated by the extravascular static contribution. Owing to partial volume effects, signal changes at the pial surface will leak into the superficial layer of the parenchyma. Figure 8.3a shows that the contribution in the static dephasing regime with TE=7 ms leads to a pronounced steep profile when compared to the case with no T_2' weighting (TE=0 ms).

In summary, the simulation results show that the intravascular contribution to the BOLD signal at the TE_{eff} used and the extravascular contribution in the static dephasing contribute more to the total signal change than the extravascular contribution in the dynamic averaging regime (e.g. extravascular T_2 contribution).

8.4.3 Effects not considered in the simulations

The average experimental profile shown in Figure 8.1 is a smoothed version of the simulated result shown in Figure 8.2. Hence, the approximations made when simulating the S2-SSFP signal seem valid. The smoothing is most likely the result of the cortical sampling perfomed to obtain laminar profiles. Nonetheless, for the sake of completeness, it is worth mentioning the effects not considered in the simulation. First, the S2-SSFP simulation used here only considered the shortest coherence pathway. According to *Goa et al.* (2013), the lifetime of the S2 pathways for TR/FA=27 ms/ 25° was ~0.3 s. This lifetime was mostly determined

by the flip angle and much less by TR. The SSFP acquisition in this work had a FA=23° and therefore a similar lifetime will be assumed. Intracortical veins have a diameter between 20 -120 μm (*Duvernoy et al.*, 1981). The incidence of intracortical veins with a diameter in the lower range is larger and prevalent in the upper layers. The diffusion time of freely diffusing spins within the parenchyma to diffuse by a similar distance as the diameter range mentioned above is between 0.066-2.4 s ($< s^2 >= 6Dt$), where the diffusion constant in grey matter is taken as 0.8×10^{-3} mm^2/s). Therefore, stimulated echoes from longer pathways may contain a contribution from intracortical veins in the dynamic averaging regime and will contribute to the steepness of the profiles. Second, considering only the most recent pathways may lead to a larger intravascular contribution compared to the case when the full S2-SSFP signal is simulated. This is, although the T_1 of blood and tissue are similar at 7 T, the shorter intravascular T_2 implies that the IV contribution will decay faster than the EV contribution with increasing coherence pathway length.

8.4.4　Consequences for pulse sequence design

The simulations show that with the parameters chosen, the intravascular signal and extravascular static dephasing around large vessels are the largest contributors to the signal change. The measurements and simulations performed here would appear to preclude the use of S2-SSFP for fMRI in most practical situations. If dynamic averaging in the parenchyma is to be the dominant contrast mechanism then TR should be increased to eliminate the intravascular contribution, and TE reduced to eliminate static dephasing (Figure 8.3b). Both of these options have highly negative consequences for the efficiency and sensitivity of the sequence. If extravascular dynamic averaging about large vessels is important then these modifications will be to no avail.

8.5　Acknowledgements

8.6   Supplementary Information
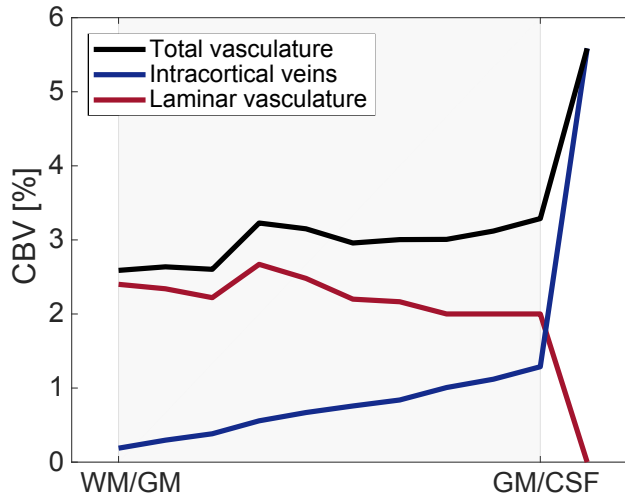
Figure S8.1: Vascular distribution across the cortex used for simulating the activation signal for the SSFP sequence (profile not smoothed).

Chapter 9

An *in-vivo* study of BOLD laminar responses as a function of echo time and static magnetic field strength

Abstract

Layer specific functional MRI requires imaging at high spatial resolution. An approach often used for compensating for the poor signal to noise ratio (SNR) associated with small voxel sizes consists of integrating the signal from voxels at a given cortical depth over a patch of cortex. After this integration, physiological noise is expected to be the dominant noise source in the signal. In this context, the sensitivity gain in moving to higher static field strengths is expected to be lower than when thermal noise is the dominant source of noise. In this work, activation profiles in response to the same visual stimulus are compared at 1.5 T, 3 T and 7 T using the multi-echo, gradient echo (GE) FLASH sequence, with a 0.75 mm isotropic voxel size and the cortical integration approach. The obtained results show that after integrating over a patch of cortex between roughly 100 and 250 voxels (for 7 T and 1.5 T, respectively), the signal is in the physiological noise dominated regime and that the obtained profiles are similar for equivalent echo times. As BOLD-like noise is the dominant source of physiological noise at the three studied fields, the functional contrast to noise ratio is not strongly echo time or field strength dependent. Nonetheless, the extent over which it is required to integrate decreases and the efficiency of the acquisition increases with increasing static magnetic field.

9.1   Introduction

The human neo-cortex is ~1.5-3 mm thick and is divided into six anatomical layers in most cortical regions. According to the canonical model of neural processing (*Felleman and Van Essen*, 1991), layers play a specific role in the feed-forward/feedback connections between cortical regions and in the processing within a cortical area. Therefore, there is a growing interest to acquire high resolution functional MRI data to measure the layer specific response and understand the interactions between brain regions.

In MRI, high spatial resolution implies a reduced image Signal to Noise Ratio (SNR) because there are less protons in the voxel that give rise to the MR signal while the main noise sources are unaltered. If everything else is kept constant, image SNR and temporal SNR (tSNR) increase with the strength of the main magnetic field (*Triantafyllou et al.*, 2005). Therefore, most layer specific BOLD-fMRI studies in humans in recent years have been performed at 7 T to obtain a higher sensitivity to activation (*De Martino et al.*, 2013; *Fracasso et al.*, 2017; *Heidemann et al.*, 2012; *Kemper et al.*, 2015; *Kok et al.*, 2016; *Koopmans et al.*, 2011; *Maass et al.*, 2014; *Muckli et al.*, 2015; *Polimeni et al.*, 2010; *Siero et al.*, 2015).

Many of these layer specific studies at 7 T further improved the signal to noise ratio (SNR) by integrating the signal over a patch of cortex at a given cortical depth. The larger the number of voxels that are integrated the better the sensitivity to activation will be, provided that the signal variation over time is not coherent between the voxels, for example if only thermal noise is present. Once physiological noise sources, i.e. those that result in signal modulations unrelated to neuronal changes induced by the functional task, become important, then the signal variation will become correlated over voxels, and the sensitivity gains achieved by summation will be diminished. In this physiological noise regime (*Kruger and Glover*, 2001; *Triantafyllou et al.*, 2005) the sensitivity gain in moving to higher static field strengths will be lower than for the thermal noise regime (*Uludağ and Blinder*, 2018).

This argumentation would in principle apply to all forms of functional contrast so far explored for laminar fMRI at 7 T: gradient-echo (GE) BOLD (*Fracasso et al.*, 2017; *Guidi et al.*, 2016; *Kashyap et al.*, 2017; *Kok et al.*, 2016; *Maass et al.*, 2014; *Polimeni et al.*, 2010; *Puckett et al.*, 2016; *Scheeringa et al.*, 2016; *Siero et al.*, 2013, 2015), spin-echo based BOLD (*De Martino et al.*, 2013; *Kemper et al.*, 2015; *Muckli et al.*, 2015; *Olman et al.*, 2012), VASO (*Huber et al.*, 2015) and SSFP (*Goa et al.*, 2014). Due to its robustness, high functional sensitivity and speed of acquisition, GE-BOLD is a widely used approach in layer specific fMRI. An assessment of the potential value of GE-BOLD laminar fMRI below 7

T requires a characterisation of the laminar activation profile as a function of TE, and measurement of the sensitivity relative to the gold standard of 7 T when data are acquired in the physiological noise regime.

We have previously performed such a characterisation at 7 T using the multi-echo FLASH sequence (*Koopmans et al.*, 2011). Here we replicate the 7 T study and extend this approach to 3 and 1.5 T. In order to perform a comparison based on BOLD signal properties alone, it is important to obtain largely distortion and dropout free images at all fields and echo times. This is achieved by measuring with a multi-echo FLASH sequence as the more common EPI image encoding scheme would suffer field-dependent distortion and signal loss. In this chapter, the laminar BOLD-dependent signal and relaxation time changes as a function of TE and static field strength are compared first. These features are independent of the temporal resolution. After that, the noise in the signal is analysed to describe the noise regime for which the functional sensitivity results obtained here apply.

9.2 Materials and Methods

The same 9 healthy volunteers (4 female, 30 ± 4 years old) were scanned at 1.5 T, 3 T and 7 T (Avanto, Skyra and Magnetom, respectively, manufactured by Siemens Healthcare, Erlangen, Germany). The coil configurations used at 1.5 T and 3 T were the vendor-provided 32 Channel head coil for reception and the body coil for transmission. At 7 T, the single channel transmit/32-channel receive radiofrequency (RF) head coil (Nova Medical Inc., Wilmington, USA) was used. Prior to the scan, all participants gave written informed consent according to the guidelines of the local ethics committees (Donders Institute, Nijmegen, the Netherlands, for 1.5 T and 3 T and Erwin L. Hahn Institute, Essen, Germany, for 7 T).

9.2.1 Data acquisition

The session protocol consisted of one high resolution anatomical scan and one high-resolution functional scan, preceded by a low resolution functional online localizer. The purpose of the latter was to position the high resolution functional slab to cover as much as possible of the V1 region that would activate in response to the stimulus used.

The high resolution functional scan was acquired using a multi-echo 3D-FLASH sequence with parameters (e.g. voxel size and echo spacing/range) matched across fields as possible (see Table 9.1 for sequence parameters). The slab thickness was thinner at 1.5 T and 3 T in order to minimise the acquisition time per volume, i.e.

the volume TR. Compared to 7 T, the TRs were longer (the last acquired echo was the limiting factor and was chosen based on the literature values of grey matter T_2^*) which lengthened the acquisition. Besides, in-plane acceleration factors achievable with good image quality were lower than at 7 T (R=3 instead of R=4) for the lower fields (*Ohliger et al.*, 2003; *Pruessmann*, 2004). Therefore, reducing the slab thickness at these fields was the way to reduce the acquisition time per volume and acquire enough volumes for a functional analysis on a reasonable time-scale.

The stimulation paradigm consisted of a circular checkerboard flickering at 7.5 Hz interleaved with a grey screen. Both conditions had a fixation cross in the middle. The duration of the stimulus block was equal to one volume acquisition time at each field (i.e. 160 s, 130 s and 97 s at 1.5 T, 3 T and 7 T respectively). The total acquisition time of the functional protocol was the same across B_0 (~27 minutes), which allows the comparison of the fMRI performance in the same amount of time (but different number of functional cycles).

The BOLD response as a function of stimulus type was studied due to concerns of an adaptation effect during the long stimulus ON block while piloting. This was tested at 3 T using one subject and a 2D-EPI sequence, with 3.5 mm isotropic voxel size and TR/TE=2000/30 ms. In this test, the following intra-stimulus patterns were studied: 6 s ON - 2 s OFF, 5 s ON- 3 s OFF, 7 s ON - 1 s OFF and continuously ON. Each of the stimulus patterns was repeated 8 times, forming a stimulus ON block with a duration of 1 min 4 s. A stimulus ON block was followed by a grey screen with a fixation cross of 1 min 4 s and the sequence was repeated 3 times. This paradigm was run four times, once per intra-stimulus pattern tested, and the temporal mean and standard deviation of the BOLD response was examined for each of the stimulus-ON patterns. The continuously ON stimulus scored the highest mean BOLD signal with the lowest standard deviation, so this was the stimulus mode chosen for the study.

The low resolution functional online localizer consisted of acquiring a 2D-EPI sequence while the subject attended to the same stimulus pattern as in the functional scan described above. These data were processed online obtaining a map of voxels that responded to the stimulus. The map was subsequently used to make sure that the thin slab used in the high resolution functional scan overlapped with the region responding to the stimulus. The relevant parameters of the functional localizer were the same across field strengths (e.g. 3.0 mm isotropic voxel size, TR=3000 ms, FA=90°, 60 measurements), and the TE was 44 ms, 30 ms, 30 ms at 1.5 T, 3 T and 7 T, respectively. The paradigm used during the functional localizer was 15 seconds of grey screen with a fixation cross, followed by 3 seconds of the same flickering checkerboard as in the functional scan. Based on the anatomical scan, the slab was first placed along the calcarine sulcus, where the BOLD response was in general strongest. Then the online functional map was used to

	1.5 T	3 T	7 T
Functional scan			
Sequence	3D-FLASH	3D-FLASH	3D-FLASH
Voxel size	0.75 mm isotropic	0.75 mm isotropic	0.75 mm isotropic
Slab thickness	12 mm	12 mm	16.5 mm
Nr of slices in the slab	16	16	22
BW/pixel	110 Hz	170 Hz	240 Hz
TE (10 echoes)	TE1/ΔTE/TE10= 7.3/10.6/102.6 ms	TE1/ΔTE/TE10= 5.9/8.1/79.0 ms	TE1/ΔTE/TE10= 4.8/5.7/56.1 ms
Read-out gradient mode	Monopolar	Monopolar	Monopolar
TR	115 ms	95 ms	63 ms
Volume TR	160 s	130 s	97 s
Duration of functional paradigm	26 min 41 s	26 min 27 s	26 min 23 s
Number of volumes	10	12	18
FA	25°	20°	20°
Parallel Imaging (in plane)	3 (ref lines: 36)	3 (ref lines: 36)	4 (ref lines: 24)
Anatomical scan	MPRAGE with 1 mm isotropic voxel size	MPRAGE with 0.75 mm isotropic voxel size	MP2RAGE with 0.75 mm isotropic voxel size

Table 9.1: Relevant acquisition parameters at the three studied fields.

adjust the orientation of the slab in such a way that it covered the activated region as much as possible.

Whole brain, high resolution, T_1-weighted anatomical scans were acquired using the MPRAGE sequence at 1.5 T and 3 T and the MP2RAGE at 7 T. The relevant parameters of the MPRAGE at 3 T were: TR/TI/TE=2300/1100/3.15 ms, FA=8°, voxel size=0.8 mm isotropic, GRAPPA factor=2. Functional data for each subject were sampled with the cortical segmentation obtained from the corresponding anatomical scan at 3 T. The anatomical scans at 1.5 T and 7 T were used to calculate the co-registration parameters between the functional scan and the anatomical scan at 3 T. The acquisition parameters for these sequences are given in Table S9.1.

9.2.2   Data processing

Motion correction and co-registration

First, the outer slices at the edges of the 3D functional slab were discarded due to imperfections of the slab profile. The skull was removed using FSL-BET (*Smith*, 2002) and all echoes at a given time-point were added together to improve the SNR of the images prior to motion correction. Motion correction was performed in AFNI (*Cox*, 1996) using a linearised weighted least squares algorithm (two passes, zero padded, 7th order polynomial interpolation), realigning all volumes to the first one, and high-pass filtered with $f_c = \frac{1}{2.1 \times volTR}$. Due to the very thin slab, some of the slices close to the edges suffered from lower or uneven signal intensity in the signal time course due to the interpolation when transforming the volume according to the motion correction parameters. These slices were removed before further processing. The anatomical volume acquired at 3 T was co-registered to the first functional scan using the boundary based registration method implemented in FreeSurfer (*Greve and Fischl*, 2009).

Cortical sampling

Following the approach used in *Polimeni et al.* (2010), the white matter surface generated in FreeSurfer was expanded (*Dale et al.*, 1999) by 10% of the cortical depth at each vertex to sample the functional volume (15 sampling points across the cortex: 2 points in white matter, 11 points in the cortex and 2 points in the CSF). To avoid areas of poor grey matter segmentation, vertices in V1 areas with an estimated cortical thickness larger than 2.5 mm were discarded from further analysis.

9.2.3 Feature extraction

Five out of the twenty-seven scans acquired had to be discarded due to within volume motion artefacts, and one scan due to deficient shimming in the occipital lobe. Features were extracted from the remaining twenty-one scans.

Signal extraction across the cortex

Depth resolved profiles were obtained by sampling unsmoothed functional volumes by nearest neighbour interpolation using the surface layering obtained in the anatomical scans (see subsection "Cortical sampling" above). All voxels sampled at a given depth were integrated over the corresponding region of interest and the average resting and activation signal over volumes were calculated. The region of interest consisted of:

- only activated voxels for metrics related to activation

- all V1 voxels that fell within the slab for metrics related to noise characteristics

Mask of activated voxels

The selection of voxels responding to the stimulus was performed by using FSL-FEAT on the high-resolution data, after summing over all 10 echoes and motion correcting the data. A 3 mm smoothing kernel was applied and voxels that scored z>2.3 were selected for the mask (see Figure S9.1). This heavy smoothing (given the high original resolution) was used for the purpose of limiting a bias towards higher fields due to their higher image SNR when calculating the mask. The surface boundaries obtained in FreeSurfer were overlaid onto the activation maps and vertices falling on activated voxels were identified.

Feature estimation

R_2^* was calculated by fitting a mono-exponential function to the signal decay obtained for each cortical depth and volume. The average R_2^*-values at rest and activation were obtained by averaging over the corresponding state and ΔR_2^* was obtained as the difference of these two values.

BOLD signal measures were obtained by computing first the average signal in the region of interest per volume and cortical depth and calculating the BOLD signal change and the functional Contrast to Noise Ratio (CNR) per echo time thereafter (a summary of this well-known calculations is given in Table S9.2).

Weisskoff test and physiological noise

The Weisskoff test was described in *Weisskoff* (1996) as a means of measuring scanner stability. This was done by measuring, in a phantom, the temporal variance of the mean signal in ROIs of different sizes. *Koopmans et al.* (2011) applied this principle to estimate the minimum extent of the ROI that was needed until physiological noise became the main source of noise in the signal. In order to measure this, an increasing number of voxels from 1 to N, where N is the maximum number of voxels in the area of interest, were averaged, and the temporal standard deviation of the average signal was computed. In the thermal noise dominated regime, this curve is expected to be proportional to $\frac{1}{\sqrt{N}}$. If increasing the number of voxels added does not result in the decrease in the standard deviation over time expected in the thermal noise dominated regime, the physiological noise dominated regime has been reached.

The Weisskoff-test was carried out as specified in *Koopmans et al.* (2011) randomly selecting voxels within V1 that were added in each iteration until all voxels in V1 within the slab were part of the ROI. The image value of a voxel is in arbitrary units. In order to be able to compare between fields, the standard deviation values were normalized by dividing them with the average of all voxels over the whole ROI for $TE = T^*_{2GM}$ at each field:

$$\sigma_{n_{i,TE}} = \frac{std_{i,TE}}{avg(S_{N,T^*_{2GM}})} \tag{9.1}$$

where i is the number of voxels that are added and goes from 1 to N. N is the total number of voxels in V1 within the slab, which varies between subjects and hemispheres. TE is the echo time and the range varies between fields as specified in Table 9.1. The numerator in Equation 9.1 is hence the standard deviation over resting volumes for a given ROI size i at a given echo time TE and the denominator is the average voxel intensity over resting volume for the ROI with all voxels at an echo time equal to the T^*_{2GM}.

9.3   Results

9.3.1   GE-BOLD signal change across the cortex

ΔS profiles in Figure 9.1a-c show the characteristic ascending profile of laminar GE-BOLD profiles across the cortex (*Duong et al.*, 2000; *Goense and Logothetis*, 2006; *Huber et al.*, 2015; *Jin and Kim*, 2008b; *Koopmans et al.*, 2010, 2011; *Lu et al.*, 2004; *Polimeni et al.*, 2010; *Trampel et al.*, 2012). This ascending shape is believed to be the result of signal leakage from lower layers as blood is drained

from lower layers to upper layers (*Markuerkiaga et al.*, 2016) and partial volume effects with pial veins will make these profiles steeper close to the cortical surface.

The curves in Figure 9.1a-c have been divided by the mean value over echoes and cortex (hence, one value per profile), so that the average profile is not dominated by differences in the mean response between subjects. This way, it is possible to focus on the differences in the profiles of activation across echoes and fields. The profiles at 7 T are similar to those shown in *Koopmans et al.* (2011), only smoother. This is because the processing step used here did not involve manual realignment of the individual profiles to account for inaccurate registration or segmentation of grey matter boundaries (*Koopmans et al.*, 2011). Laminar GE-BOLD profiles at 3 T are less frequent in the literature. Nonetheless the results shown here (Figure 9.1b) are in line with the ascending profiles for similar stimuli reported to date (*Koopmans et al.*, 2010; *Ress et al.*, 2007). Part of the variability between previous and current work may be due to differences in echo time, studied region or analysis approach. The profiles obtained at 1.5 T (Figure 9.1a), which represent to our knowledge the first layer specific functional studies at this field, show qualitatively the same expected behaviour as those obtained at higher fields but with a slightly lower SNR.

The steepness of the profiles for different echo times in Figure 9.1a-c depends on the intravascular and extravascular signal contribution to the BOLD signal change, which varies with TE and B_0. For example, at 7 T, the signal on the pial surface is larger for shorter TEs (compare yellow and orange curves). This is because at short echo times, there is still a venous intravascular contribution to the BOLD signal change (a compilation of venous relaxation times across fields is given in Table S9.4). This contribution is larger for large pial vessels on the pial surface than for venous vessels in the parenchyma, due to larger blood volume.

To summarize the data presented in Figure 9.1a-c and allow a simpler comparison between fields, we used the parenchyma to pial ratio of the BOLD signal change (Figure 9.1d). Note that in this graph the TEs -which were different across fields- in the x-axis have been normalized with the average T_2^* within the parenchyma obtained at that field. It is shown that pial contribution increases with shorter TEs. For equivalent echo times between fields, the magnitudes of the ratios themselves are similar, around 0.65 for TE=T_2^* (grey matter). This similarity of the ratios is in line with the simulation results for the ratio of micro- and macrovascular contributions between fields given in *Uludağ et al.* (2009).

A 2-way ANOVA test of the pial to parenchyma ratio was performed to assess the effect of echo time, field strength and their interaction. Only the effect of the echo time was significant. For short echo times (TE1-5), with considerable intravascular contribution, the parenchyma to pial ratio is significantly different to that of late echoes (TE8-10), where venous signal has faded away.
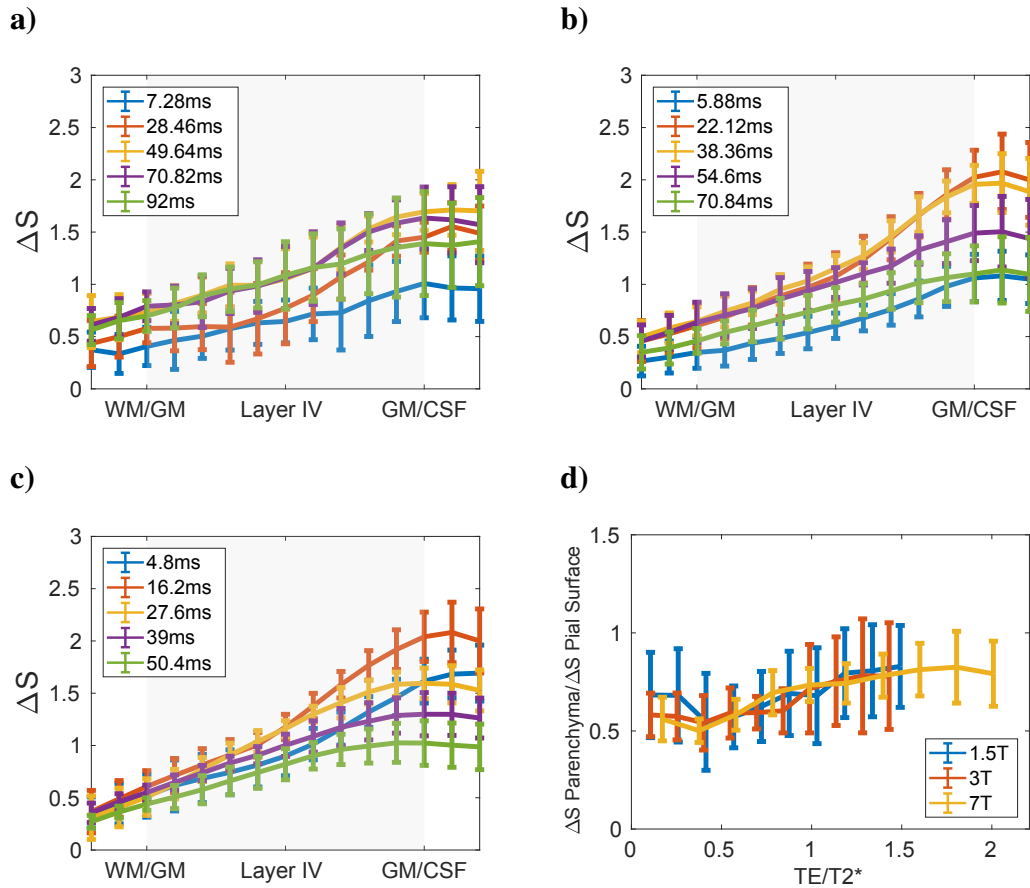
Figure 9.1: BOLD signal change, ΔS, profiles averaged over subjects for different echo times (5 out of 10 echo times shown for visualization purposes) at **a)** 1.5 T, **b)** 3 T and **c)** 7 T. The individual profiles have been divided by the mean value over echoes and cortex (hence, one value per profile), so that the average profile is not dominated by differences in the mean response between subjects. **d)** The ratio between the signal change in the middle of the parenchyma and on the pial surface across fields. The echo times used at each of the field strengths have been normalized with the corresponding T_2^* measured in the middle of the parenchyma.
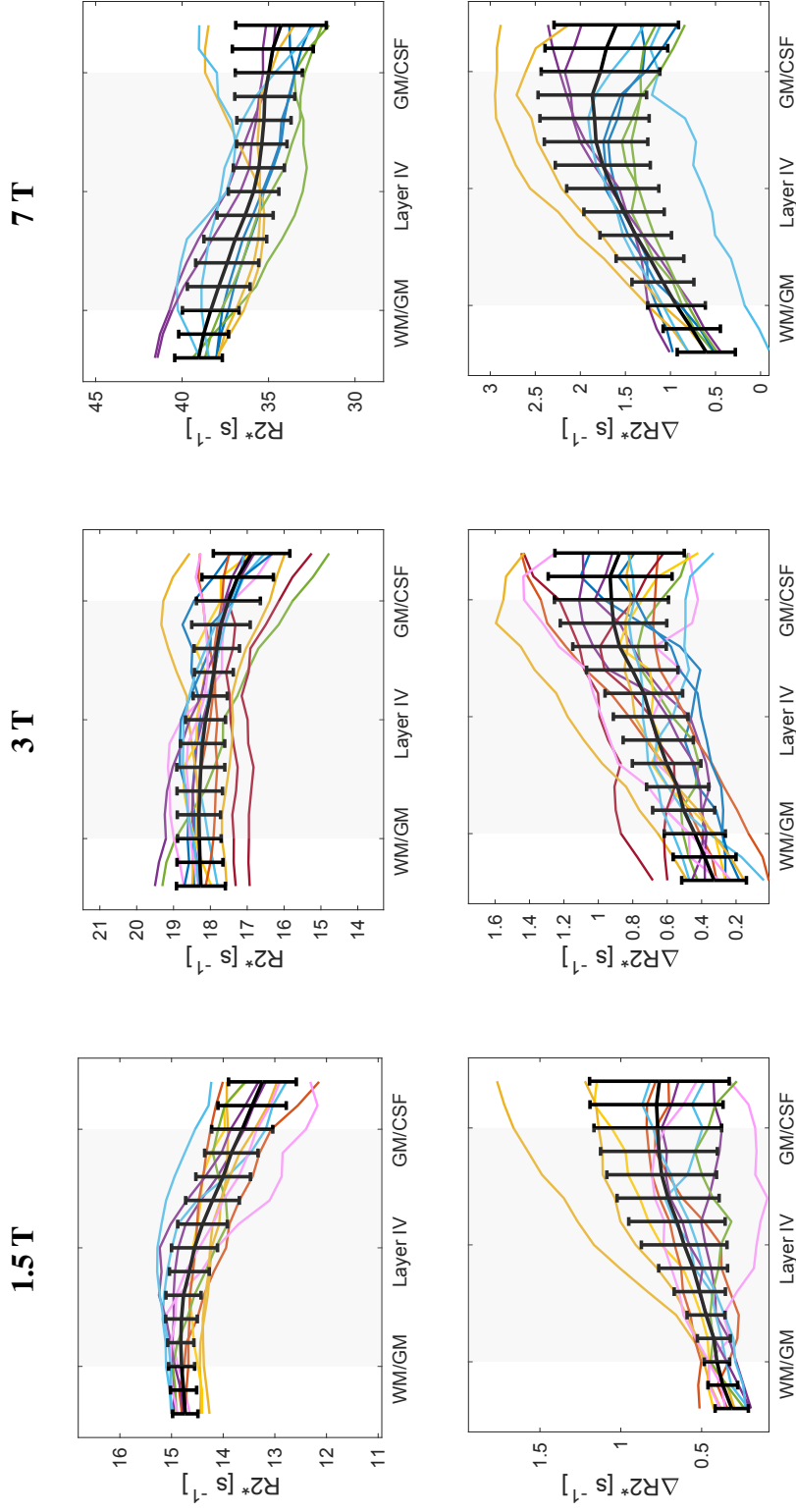
Figure 9.2: Individual R_2^* (upper row) and ΔR_2^* (bottom row) profiles for each subject and hemisphere (each colour corresponds to a subject and each line to the profile within a hemisphere). The black line is the mean ± std over subjects, normalized with the average T_2^* of grey matter at that field.

9.3.2   Resting R_2^* and ΔR_2^* upon activation

Transverse relaxation times at rest and upon activation are shown in Figure 9.2. The acquisition and analysis approach used in this work (i.e. acquiring at submillimeter isotropic resolution and integrating over a given cortical depth) allows for a good separation between parenchymal signal and signal from the pial surface, as it limits the partial volume effects.

The average T_2^* relaxation times within the cortex (T_2^*= 70, 55 and 27 ms approximately, shown in Table 9.2) are in line with those published previously (as summarized in Table S9.3). The average R_2^* values and profiles obtained at 7 T are similar to those shown in *Marques et al.* (2017). The reduction in R_2^* from the WM to the pial surface was observed at all field strengths (Figure 9.2a-c) and has been attributed to a combination of reduction of myelin and iron (*Stüber et al.*, 2014). On the other hand, the variation of transverse relaxation rate upon activation, ΔR_2^*, had the opposite behaviour, increasing from the WM to the pial surface reflecting the increased blood partial volume and oxygenated blood draining towards the cortical surface.

The voxels that coincide with the pial surface generated in FreeSurfer will in general contain three compartments with very different relaxation times: parenchymal tissue, CSF and pial veins. It was not possible to fit a multi-compartment relaxation given the noise level in the data, the differences in the relaxation times of the compartments in the voxel, and the range and number of echo times used in this work.

9.3.3   Temporal fluctuations of the resting signal

The Weisskoff curves calculated as in Equation 9.1 are shown for all field strengths and subjects in Figure 9.3a-c. All Weisskoff curves reach the plateau related to the physiological noise dominated regime after integrating over a couple of hundred voxels, except for one outlier at 1.5 T and 3 T. The variability between subjects within a field is stronger than the differences between fields. Hence, the differences in the physiological level between fields are not statistically significant. A regression analysis between the magnitude of the physiological noise level and the motion parameters from the motion correction algorithm was performed and there was no relationship between the two and scatter plots showed rather randomly spread data points (data not shown). Therefore, the variability of physiological level can be related to the variability of the BOLD signal between sessions or/and to other sources of signal fluctuations that cannot be corrected in post-processing, such as microscopic movement during volume acquisition or small differences in the GRAPPA kernel used in each volume. These effects are expected to affect the

noise level in the physiological noise dominated regime in a similar way at the three field strengths.

Figure 9.3d shows the average profiles over subjects at each of the field strengths to visualize any potential differences in the number of voxels that signal needs to be averaged over until the plateau is reached. Visual inspection shows that the point in which the average Weisskoff curve deviates from the noise level in the physiological noise dominated regime (dashed lines), is reached earlier with increasing field, but within 250 voxels at all fields (~100 voxels at 7 T, ~150 voxels at 3 T and ~250 voxels at 1.5 T).

These rough limits show the number of voxels that need to be averaged until a fully physiological noise dominated regime is achieved. It is worth mentioning that most of the thermal noise averaging has happened after averaging fewer voxels. For example, at 1.5 T, after averaging 50 voxels, the magnitude of the signal fluctuation is 17% of the fluctuation for the single voxel, while in the physiological noise dominated regime is 10%.

Figure 9.4 shows the magnitude over echoes of the physiological noise level. This is, the variation over TEs of the magnitude of the plateau shown in Figure 9.3 for TE=T^*_{2GM}. Following the physiological noise model in *Kruger and Glover* (2001), the non-BOLD like noise (e.g. cardiac/respiratory fluctuations, scanner instability ...) scales with signal strength and will therefore decrease with echo time. The BOLD-like noise (e.g. resting neuronal fluctuations or blood flow changes), on the contrary, will follow the BOLD signal pattern. The average profiles obtained in this work once the plateau has been reached in the Weisskoff test first increase and then decrease with echo time, indicating that BOLD-like physiological noise dominates. Therefore, although no cardiac or respiratory noise correction have been used due to the very long volume TRs, the results suggest that BOLD-like noise is the main contributor to physiological noise in this dataset after signal is averaged along the cortex. As a sanity check, these profiles were compared to the profiles obtained for single voxels. These did not follow a similar shape and varied greatly across voxels, as expected from a thermal noise dominated noise distribution.

The limited number of resting volumes and subjects calls for cautious interpretation of these results. In fact, the 1-way ANOVA test shows that the curves only show a statistically significant dependence of TE at 7 T. However, it is worth mentioning that the profiles of the physiological noise over echo times in Figure 9.4 show that, at 1.5 T and 3 T, a larger magnitude of the resting fluctuation for echo times close to the T^*_2 time of venous blood, marked in green in the figures, than for the echo time corresponding to T^*_{2GM}, marked in red. This pattern is reversed for the profile at 7 T, which shows a larger magnitude of the fluctuations at around the T^*_2 of tissue (marked in red in the figures). This is in line with the fact that intravascular contribution to the BOLD signal change is larger at 1.5 T and 3 T than at 7 T.
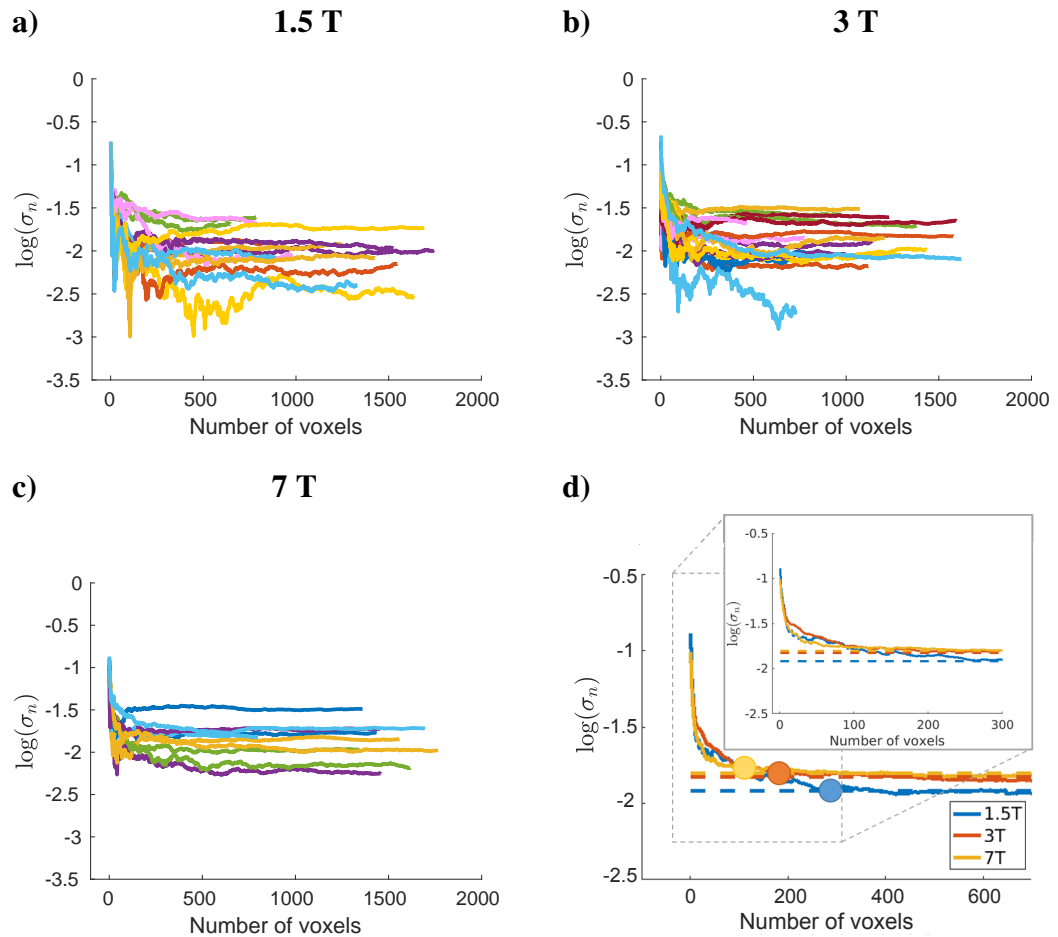
Figure 9.3: Results of the Weisskoff test. Standard deviation over time of the mean resting signal as a function of the number of voxels considered/included (see Equation 9.1) at **a)** 1.5 T, **b)** 3 T and **c)** 7 T. The voxels added were located in the middle of the parenchyma and the curves here correspond to TE=T^*_{2GM} at each field. Each colour represents a subject, one line per hemisphere. **d)** The average of the Weisskoff curves over subjects for the three fields studied. The circles correspond to the point in which the curve deviates from the plateau corresponding to the noise level once the physiological noise dominated regime has been reached (shown with dashed lines of the corresponding colour for each field). The inset corresponds to the result for the first 300 voxels.
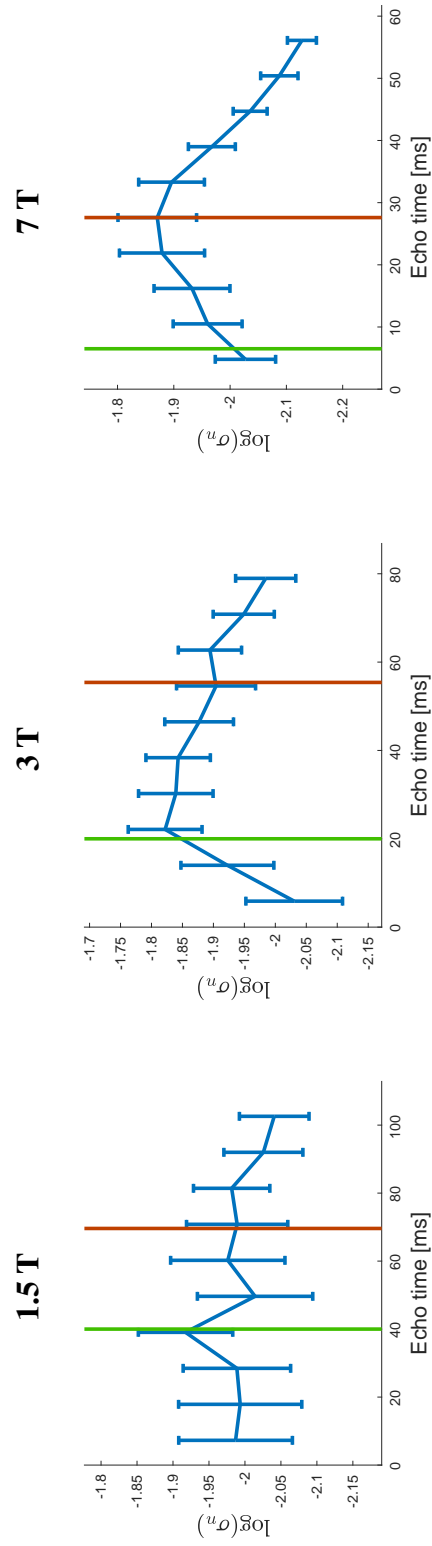
Figure 9.4: Average physiological noise level over subjects and standard error for the studied echo times in the middle of the parenchyma at 1.5 T (left), 3 T (middle) and 7 T (right). The green vertical line marks the venous T_2^* and the red vertical line marks the T_2^* of grey matter at each field.

9.3.4   Functional contrast to noise ratio

Figure 9.5 shows the functional contrast to noise ratio (CNR), measured as the signal change upon activation divided by the temporal standard deviation over time at rest. This is, the individual BOLD signal changes in Figure 9.1a-c divided by the individual standard deviation at rest. This is a measure of the sensitivity to activation induced BOLD signal changes. As in Figure 9.1, the profiles are less smooth at 1.5 T, most likely because of poorer cortical segmentation due to poor white matter/grey matter contrast. The magnitude of the curves are similar, specially between 3 T and 7 T. In addition, the error-bars at 3 T are larger than at 7 T, not because the inter-subject variability is higher at 3 T, but because the estimation of the standard deviation over time of the resting signal is less accurate due to the lower number of volumes in the resting condition. If CNR profiles for the first 12 volumes at 7 T are calculated, comparable error-bars are obtained (data not shown). A 2-way ANOVA test with interaction effects shows that within a field and in the middle of the parenchyma, there is no statistically significant TE-dependence of CNR. The differences in CNR are statistically significant between 1.5 T and 7 T. There is no interaction effect between field strength and echo time.

Despite the functional CNR being very similar between 3 T and 7 T, Figure 9.6a shows that the t-scores obtained at 7 T are higher at all echo times and cortical depths. This is because the temporal resolution is higher at 7 T and more volumes are acquired per unit time. This increases the degrees of freedom of the statistic and therefore the t-score. Figure 9.6b shows that within a field, the t-scores obtained do not vary considerably with TE. In fact, a 2-way ANOVA test accounting for the interaction effect shows that there is no TE nor interaction effect of TE with field strength. The t-scores obtained at 7 T are significantly different for those obtained at 1.5 T and 3 T.

9.3.5   Mask of activated voxels

As shown in Table 9.2, the extent of the region responding to the stimulus in the primary visual cortex increases with field. The masks were obtained using the same threshold for the z-score (2.3). Again, as the degrees of freedom when performing the statistical inference are higher at 7 T, the z-values will be increased, and more voxels will be above the defined threshold. In addition, the spatial coverage of V1 before and after motion correction was larger at 7 T. Figure S9.1 in the *Supplementary Information* shows activation maps for a sample subject across fields.
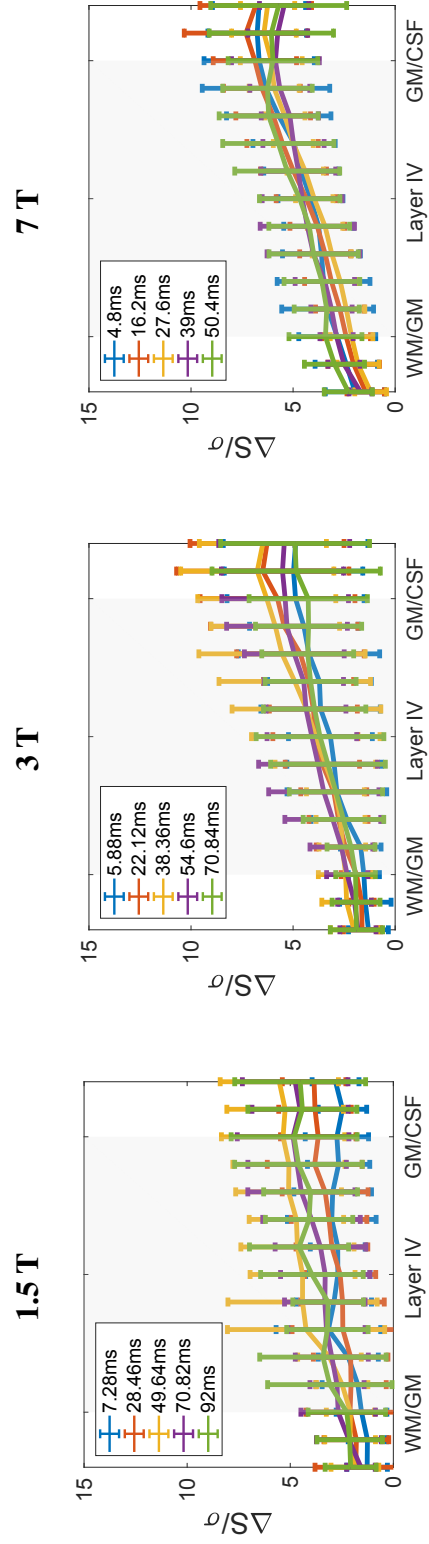
Figure 9.5: Functional CNR profiles at 1.5 T (left), 3 T (middle) and 7 T (right). The signal change upon activation (ΔS), is divided by the standard deviation over time of the signal in the resting condition, σ. Profiles correspond to average±std over subjects for different echo times (5 out of 10 echo times shown for visualization purposes).
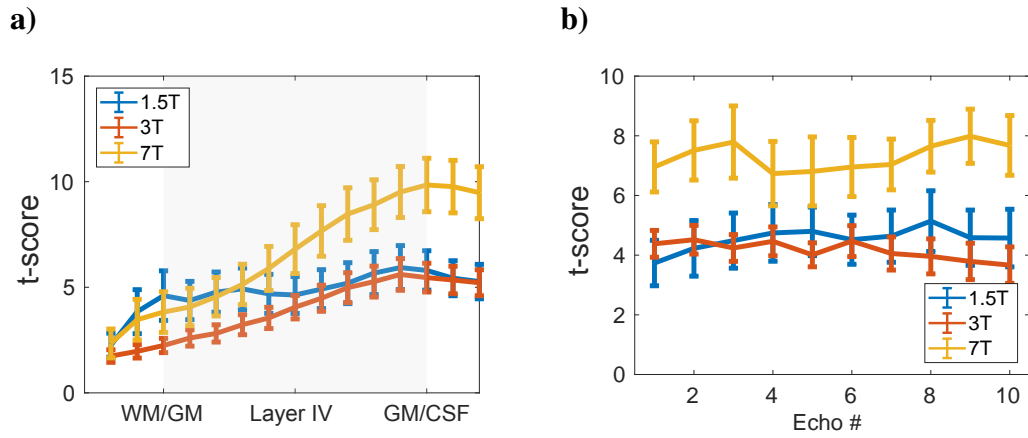
Figure 9.6: Average over subjects and standard error of **a)** t-scores across the cortex for TE=T^*_{2GM}, and **b)** t-scores in the middle of the parenchyma for each of the 10 echoes acquired. Note that the echo times acquired are different for the different fields (see Table 9.1).

9.4 Discussion

9.4.1 Activation profiles and relaxation times

GE-BOLD activation profiles are similar for equivalent TEs at 3 T and 7 T. The profiles at 1.5 T are noisier and less steep for short TEs. The steepness of the curves is TE-dependent and this fact should be considered, as already mentioned in *Koopmans et al.* (2011), if profiles at different TEs or non-equivalent TEs are compared within or between fields (Figure 9.1).

These profiles also inform about changes in the parenchymal specificity of the signal for standard voxel size fMRI in which thermal noise is the dominating source of noise. The curves in Figure 9.1d have all a minimum around $0.3 - 0.4 \times T^*_{2GM}$ which corresponds roughly the T^*_{2veins} at each field. This shows that the use of shorter echo times increases the pial contribution of the measured signal change. After this TE time, the microvascular contribution to the signal steadily increases for the TEs considered in this study.

Due to the submillimeter voxel size used, an estimation of the transverse relaxation time within grey matter with limited contamination from adjacent white matter and pial surface was computed. The mono-exponential signal decay was a good fit for the signal decay within grey matter and the estimated relaxation times are in accordance with those previously given in the literature (current work: 69.6 ms, 55.4 ms and 27.4 ms for 1.5 T, 3 T and 7 T, respectively; previous work: see Table S9.3).

	1.5 T	3 T	7 T
Number of voxels in the slab after motion correction that fall in the middle of GM	1199 ± 401	1140±342	1514±278
Activated voxels in V1 within the slab	32%	34%	41%
TE of ΔS_{max} on the pial surface	39.05 ms	30.24 ms	10.5 ms
TE of ΔS_{max} in the middle of the cortex	60.23 ms	46.48 ms	21.9 ms
T_2^* in grey matter at rest	68.8±2.1 ms	55.2±1.7 ms	27.9±1.2 ms

Table 9.2: Comparison of basic activation related results across field strengths.

9.4.2 Physiological noise dominated regime in the parenchyma

The Weisskoff curves in Figure 9.3 all reach a plateau, which indicates that signal averaging across the cortex results in a signal in which physiological noise is the dominant noise source at all fields. The average Weisskoff curves show that this regime is reached after averaging fewer voxels with increasing field strength; around 250, 150 and 100 voxels at 1.5 T, 3 T and 7 T, respectively. 250 voxels are roughly equivalent to a surface of 140 mm^2. This is expected because the physiological to thermal noise ratio increases with the static magnetic field. However, the inter-subject variability, see the Weisskoff curves for the single subjects, is stronger than the differences between fields. Most of the improvement in the reduction of the temporal fluctuations is achieved after averaging a small number of voxels: for example, at 1.5 T, around 90% of the total reduction was achieved after averaging over 50 voxels (and earlier in the other two fields). These results are in line with the results shown in *Triantafyllou et al.* (2011, 2016) in which they show that physiological noise dominates even at voxels as small as 3 mm^3 at 3 T and 7 T when a 32-channel array coil is used.

The integration approach along grey matter used in this work will lead to a higher tSNR if compared to the acquisition of a voxel with an equivalent volume (as long as the voxels have a significant grey matter fraction) as explained in *Triantafyllou et al.* (2006). However, it is difficult to estimate what the increase in tSNR will be as it depends on the extent of the spatial correlation of the physiological noise over the studied region, which is not known.

The physiological noise profiles in Figure 9.4 suggest that in this dataset BOLD like noise is the dominant source of physiological noise, although no physiolog-

ical noise correction method was used. This dominance of BOLD-like noise is probably the result of considering pure grey matter voxels where the BOLD noise should be higher than in white matter or CSF.

9.4.3   Functional CNR when BOLD-like physiological noise dominates

The time-course CNR is the parameter that determines the functional sensitivity of a sequence and therefore sequence parameters are optimized so that this measure is maximized. If the MR signal in a voxel is accurately characterized by a mono-exponential decay plus some TE-independent noise, i.e., thermal noise, then the highest functional sensitivity or functional CNR will be achieved at TE=$T_2^{(*)}{}_{GM}$. However, in the presence of physiological noise there will be a noise contribution that is TE dependent (*Kruger and Glover*, 2001). If the non-BOLD like physiological noise (i.e. mostly the corruption of the signal induced by the heart beat and respiration) dominates, then the maximum of the functional CNR curve will be located at TE $> T_2^{(*)}{}_{GM}$ (*Wald et al.*, 2015). If BOLD-like noise (i.e. signal fluctuations related to neural and hemodynamic fluctuations at rest) dominates, then the CNR curve will be flattened and the maximum functional sensitivity will be less TE-dependent (*Kruger and Glover*, 2001; *Wald et al.*, 2015).

The CNR profiles across the cortex, see Figure 9.5, are less steep than the ΔS profiles, especially for shorter echoes. This is because the shape and magnitude of the physiological noise profile across echoes follows to some extent that of ΔS, which results in a flattening of the profile and a convergence of the CNR magnitude. In addition, the CNR-values, especially for 3 T and 7 T, are very similar. This implies that when physiological noise dominates, the signal properties of the functional response are not remarkably different (*Kruger and Glover*, 2001; *Uğurbil et al.*, 2006). However, as the temporal resolution is higher at 7 T, the sequence is more efficient. This results in higher degrees of freedom of the statistical analysis, leading to higher t- scores across the cortex (Figure 9.6a). Because CNR does not vary considerably between echo times, t-scores obtained are also very similar between echoes within a field (Figure 9.6b).

9.4.4   Laminar fMRI acquisition options when physiological noise dominates

The physiological noise dominated regime is reached after averaging a few hundred voxels even at 1.5 T and the CNR does not vary much between fields when BOLD-like physiological noise dominates. This opens up a range of possibilities, depending on the application of the laminar study.

It follows from Figure 9.6b that, as long as BOLD-like physiological noise dominates, it would be possible to acquire at shorter TEs and improve the temporal resolution of the sequence. Furthermore, note that in the multi-echo acquisition presented in this work, the longer echoes are implicitly limiting the TR of the shorter echo acquisitions, thus in a single echo acquisition the efficiency will be higher for shorter TEs. An implication of acquiring at short TE would be that due to increased intravascular contribution, the laminar specificity of the BOLD signal will be increased (the microvascular volume is larger than that of draining veins), but so will the signal from large pial veins, increasing the need for an accurate segmentation.

If the region of interest spreads over a lager area than the number of voxels required to be in the physiological noise dominated regime at 1.5 T (or 3 T), it is possible to perform GE-BOLD laminar fMRI study at fields lower than 7 T. Specially at 1.5 T, as the T_2^* contrast between white matter and gray matter is very poor at this field, it would be advantageous to acquire the functional data with a distortion matched T_1-w anatomical scan that will ease the segmentation and coregistration of the region considerably.

Furthermore, if the patch of cortex over which it is integrated is large enough that signal is still physiological noise dominated after increasing the GRAPPA factor, then do this, as the temporal efficiency of the sequence will be better. Lastly, if a higher resolution across the cortex is required and the region of interest is large enough, averaging would allow to acquire very small voxels that can then be integrated over a larger patch of cortex to gain back SNR.

9.4.5   Choice of the acquisition protocol

The first focus of this study was to characterize BOLD signal profiles across fields and echo times. Therefore, it was important to obtain largely distortion and dropout free images to be able to make a comparison based on signal properties alone. Otherwise, the results would depend on the success of correction-methods in the post-processing. That is why the multi-echo FLASH sequence was used for the functional scan, instead of the EPI approach, more common in functional scans. In addition, the multi-echo implementation in the FLASH sequence allows a more accurate characterization of the transversal signal decay than the one obtained with multi-echo EPI.

The design of the protocols used was made such that they would be maximally SNR efficient (acquiring during the total TR time), using the same number of echo times, and covering a comparable range of TE/T_{2GM}^*. This was considered the fairest comparison that could be designed across different fields given their different relaxation times.

The Lorentzian broadening induced by the relaxation during acquisition is $\Delta f = \frac{1}{\pi T_2^*}$. In grey matter, this equals 4.6 Hz, 5.8 Hz and 11.4 Hz, at 1.5 T, 3 T and 7 T, respectively. As the 3D-FLASH sequence was used, the BW per pixels in the PE direction is infinite whereas the BW/pixel in the RO direction were 110, 170 and 240Hz/pixel for 1.5 T, 3 T and 7 T, respectively. These values are well above the linewidth broadenings mentioned earlier, hence it is not expected to have considerable differences in the degree of blurring across fields.

The visual cortex was chosen because it is a well characterized primary cortical region, in which strong BOLD responses can be registered. The drawback of studying V1 is that it is rather thin, ~2 mm on average. Therefore, in order to acquire depth resolved signal in V1, the acquisition of submillimeter voxel sizes in the 3 spatial directions was essential (0.75 mm isotropic voxel sizes were used in this study).

All these choices (i.e. distortion free, multi-echo and high-resolution acquisition) provided a high spatial accuracy that came at the cost of temporal resolution (acquisition time per volume over 1 min 30 s at all fields). As the acquisition time per volume varied with field (160, 130 and 97 seconds at 1.5 T, 3 T and 7 T, respectively), the choice made was to keep the total acquisition time of the functional protocol equal across fields (~27 minutes) and assess the performance in the same amount of time. Because the acquisition time at 1.5 T and 3 T was considerably longer, the number of resting volumes at these fields is substantially lower. This results in noisier profiles of the temporal fluctuations of the resting signal.

9.4.6   Validity of the results shown here for BOLD fMRI that use a standard temporal resolution

Due to the reasons just explained, the temporal resolution used in this work is very poor compared to that of conventional fMRI studies. Hence, it is worth discussing how the results obtained here apply to more common functional GE-BOLD acquisitions.

The GE-BOLD profiles as a function of TE and static field strength are independent of the temporal resolution of the sequence. *Kim and Kim* (2011) reported that for stimuli longer than 20 s the venous compartment dilated, which was not the case for shorter stimuli. The stimulus durations at the different fields (i.e. 1 volume TR) used here are well above that boundary. Therefore, venous contribution across the cortex may vary compared to profiles obtained with shorter stimuli. However, this will be the case at all fields (as the stimulus duration is well above 20 s in all cases), so the comparison between fields is still valid.

In terms of the noise behaviour of the resting signal, the results presented here apply to the case in which BOLD-like physiological noise is the dominant source of noise. Depending on the temporal resolution and acquisition scheme (2D/3D) used, the physiological noise level and distribution might be different to the one obtained in this work. In addition, the laminar signal obtained in this study is likely to have extra sources that introduce temporal fluctuations that will appear as "physiological noise", such as small movements within the long volume acquisition times that cannot be corrected for or the fact that the GRAPPA kernel is calculated for each volume, which might introduce small variations in the time-course.

In order to have an idea of what the physiological noise level is in a more standard fMRI protocol, the Weisskoff test was performed on a functional dataset obtained using a 3D-EPI acquisition at 7 T (other relevant parameters: volume TR ~ 4 s, 0.9 mm isotropic voxels and TE=22 ms), as shown in Figure S9.2 in the *Supplementary Information* of this chapter. The tSNR of the 3D-EPI for the integrated signal in the middle of the parenchyma was 68, whereas the average at 7 T in the FLASH sequence for the corresponding echo time was 78.9. The profile and physiological noise level obtained for this subject is comparable to those obtained using the 3D-FLASH (none of the datasets have been corrected for physiological noise). As the 3D-EPI was acquired at a single echo time, it is not possible to assess which is the dominant source of physiological noise in this dataset. However, if non-BOLD like physiological noise removal techniques are successfully applied in these datasets, then the dominating noise source would be BOLD-like physiological noise and the results regarding functional sensitivity shown in this chapter would apply to this type of acquisition too.

Although the behaviour of 3D-EPI with acquisition times above the cardiac and respiratory signal periods might show a similar noise pattern as the data acquired in this study, 2D-EPI acquisitions are likely to show a very different noise pattern when compared to multi-shot acquisitions (*Huber et al.*, 2018; *Lutti et al.*, 2013; *Reynaud et al.*, 2017) as physiological noise is not spread all over k-space and the physiological noise removal per acquired slice might work better. Hence, the extent over which it is necessary to integrate might be larger than the one shown in this chapter.

In summary, this work shows that GE-BOLD signal changes across the cortex following activation are TE-dependent and have comparable activation profiles between fields for equivalent echo times. When BOLD-like physiological noise dominates, which was the case in this study, the Contrast to Noise Ratio (CNR) profiles are largely echo time and field strength independent. This implies that high resolution laminar fMRI studies can be acquired at TE<T_{2GM}^* and/or at B_0 < 7 T with comparable CNR. Nonetheless, the extent over which it is required to integrate decreases and the efficiency of the acquisition increases with increasing static magnetic field.

9.5   Acknowledgements

9.6   Supplementary Information
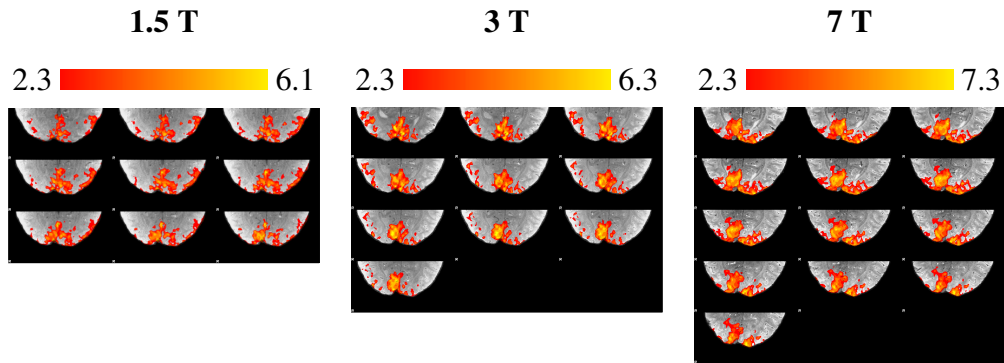
Figure S9.1: Activation maps obtained for a sample subject at 1.5 T, 3 T and 7 T. Activated voxels in the primary visual cortex were used as a mask to extract activation profiles.
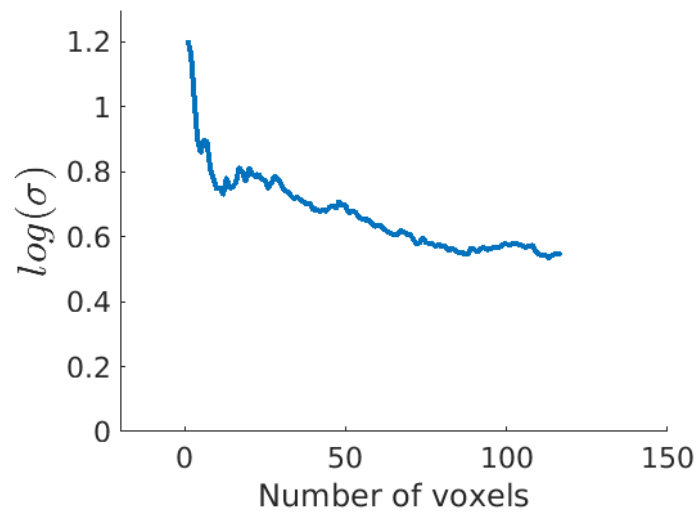
Figure S9.2: Results of the Weisskoff test for a dataset acquired using the 3D-EPI sequence with 0.9 mm isotropic voxel size and volume TR=3.96 s.

	MPRAGE @ 1.5 T	MPRAGE @ 3 T	MP2RAGE @ 7 T
TR [ms]	2300	2300	6000
TI1/TI2 [ms]	1100/-	1100/-	800/2700
TE [ms]	2.92	3.15	3.06
FA1/FA2 [°]	8/-	8/-	4/5
Voxel size [mm^3]	1x1x1	0.8x0.8x0.8	0.75x0.75x0.84
GRAPPA acceleration factor	3	2	3
Acquisition time	4 min 31 s	6 min 35 s	9 min 38 s

Table S9.1: Relevant acquistion parameters of the whole brain anatomical scans at each of the field strengths.

Name	Abbreviation	Formula
BOLD signal change	ΔS	$\Delta S = \overline{S_{act}} - \overline{S_{rest}}$
Functional contrast to noise ratio	(Functional) CNR	$CNR = \dfrac{\overline{S_{act}} - \overline{S_{rest}}}{std(S_{rest})}$
t-score	t	$S = X\beta + \epsilon$ $t = \dfrac{c'\beta}{\sqrt{Var(\epsilon)c'(XX')^{-1}c}}$

Table S9.2: List of activation related metrics and their functions used in this chapter.

Brain region Journal article	Voxel size [mm³]	1.5 T	3 T	4 T	7 T
Occipital lobe *Cox and Gowland* (2008)	1x1x3	74.9	59.7		42.1
Primary visual cortex *Gati et al.* (1997)	1.25x1.25x5	69.4		31.7	
Visual cortex *Yacoub et al.* (2001)	0.75x0.75x5			41.4 ±5.5	25.1 ±3.5
Average in cortical GM *Peters et al.* (2007)	2.1x2.1x3	84.0 ±0.8	66.0 ±1.4		33.2 ±1.3

Table S9.3: An overview of T_2^* values of grey matter, in milliseconds, reported in the literature.

Journal article	1.5 T	3 T	7 T
Blockley et al. (2008) *Y*=0.6, *Hct*=0.43	40	14.28	4
Zhao et al. (2007) *Y*=0.62, *Hct*=0.44		21.2	
Barth and Moser (1997) *Y*=0.72	42±2.8		
Yacoub et al. (2001) *Y*= 0.45			9

Table S9.4: Venous T_2^* times, in milliseconds, reported in the literature (ex-vivo samples). *Y* refers to the oxygenation of blood and *Hct* to hematocrit.

Chapter 10

Summary and Discussion

10.1 Summary

The availability of higher static magnetic fields, the advances in hardware and in acquisition sequences have led to a proliferation of laminar studies in fMRI. A bibliometric search shows that most of the ~130 articles in laminar fMRI literature have been published in the last decade. This literature is very heterogeneous. Studies include (mostly) animal work aiming at eliciting the properties of the laminar hemodynamic response to activation; fMRI acquisition methods development to measure CBV, CBF or $CMRO_2$ at very high resolution with sufficient SNR; post-processing strategies to obtain highly laminar specific signal across the convoluted cortex; assessment of the modulation of the layer input in response to different stimuli.

Compared to the other fMRI methods, GE-BOLD is the easiest approach to implement and has the largest efficiency and sensitivity to activation. In addition, it is the only technique capable of achieving large brain coverage with an acceptable frame-rate for fMRI. The downsides are that it is not quantitative and that the spatial specificity is degraded due to signal spread through draining veins. This thesis focuses on the use of GE-BOLD based functional MRI for layer specific functional MRI.

Chapter 6: Model of cortical vasculature to simulate BOLD profiles

The first part in this thesis deals with the characterization and correction of the spatial spread of the BOLD-based laminar fMRI signal. For this purpose, a model of cortical vasculature was developed. This model relies on anatomical and physiological studies available in the scientific literature and captures microvascular and macrovascular variations across the cortex. The static BOLD response to neuronal activation was simulated for the case in which signal is processed by integrating over a convoluted patch of cortex, i.e., it contains intracortical veins oriented over a wide range of angles with respect to B_0. The BOLD response was simulated at 7 T, as this is the field strength in which most laminar fMRI studies in humans have been performed.

The SE profile obtained in the simulation followed the microvascular density, which is rather flat across the cortex, whereas the GE-profiles presented an ascending profile towards the cortical surface. The model allowed us to estimate the physiological point spread function (pPSF) of the laminar activation. As blood is drained unidirectionally, the pPSF was skewed towards the surface, presenting a laminar peak followed by a rather constant tail all the way to the cortical surface. Hence, the pPSF could be approximated to a laminar peak followed by a constant tail that can be characterized by one parameter: the peak to tail ratio (p2t). At 7 T and at a TE matched to tissue T_2, the tail of the SE PSF was negligible, as the venous volume and the intravascular contribution at that TE are small. The physiological PSF for GE presented the same shape, with a non-negligible tail towards the surface. In the absence of an intravascular contribution to the GE signal, the p2t was roughly between 3.5 and 5.5 for a range of realistic neurovascular coupling ratios, n=2.5-4.

Chapter 7: Deconvolution of GE-BOLD profiles with the physiological point spread function

The next logical step was to study the use of the knowledge gained about the physiological point spread function to correct for the interlaminar leakage of the GE-BOLD signal. Intuitively, the measured cortical profiles are the result of the spatial convolution of the underlying activation profiles with the physiological PSF. Hence, the deconvolution of the measured activation profiles with the estimated physiological PSF should deliver the interlaminar leakage-fee activation profile. This approach was tested using multi-echo FLASH data. These data are well suited for this purpose because there is one activation profile per echo time, while the underlying activation remains unchanged over the acquired echo times. Indeed, the use of the TE-dependent p2t to deconvolve the activation profiles ob-

tained with the FLASH sequence delivered flatter profiles that were similar across echoes.

In order to assess its robustness and general applicability, the deconvolution approach was further tested with profiles obtained using high-resolution 3D-EPI, a sequence commonly used in high resolution functional MRI studies. The deconvolved profiles of the average activation signal across the cortex no longer showed an ascending profile and showed a stronger correlation with the presumably leakage-free profiles measured in that study (*Fracasso et al.*, 2017). Lastly, keeping in mind the general applicability of the method, a correction of the p2t magnitude was proposed dependent on the number of cortical divisions across the cortex, often referred to as bins, as laminar studies generally differ in the number of cortical divisions they use.

Chapter 8: S2-SSFP to obtain T_2-like contrast

Ideally, one would acquire laminar activation without signal leakage through intracortical veins. The easiest approach for doing this is acquiring T_2-based BOLD acquisition. In order to gain sensitivity, the acquisition can be performed at ultra-high field, such as 7 T. However, as the energy deposition in tissue by the RF pulse increases approximately with B_0^2, high-resolution whole brain acquisition can hit SAR limits. Further, if the acquisition is paired with an EPI read-out, there will be some T_2'-weighting in the signal and the spatial specificity of the measured signal will decrease. That is why the acquisition of S2-SSFP as an alternative approach to obtain T_2-like contrast without hitting SAR limits was explored in this thesis. This study built upon an earlier study by *Goa et al.* (2014), with the difference that only the S2 signal was acquired, which resulted in a sequence with reduced demands on gradients, better SNR and allowed the timing parameters to be optimized to the maximum signal change in tissue.

The expectation was to obtain T_2-like activation profiles that would follow the microvascular density across the cortex and would be rather flat. Nonetheless, the activation profiles obtained followed a clear ascending curve, more in line with T_2^* profiles in the literature. In order to elucidate this, the cortical vascular model developed earlier in this thesis was used. The S2-SSFP signal was approximated as a T_2-like activation profile with an additional T_2' weighting introduced due to acquiring some milliseconds before the (stimulated) echo time.

The results of the simulation showed that it was plausible that the intravascular signal and extravascular static dephasing around large vessels were the largest contributors to the signal change. The measurements and simulations performed appeared to preclude the use of S2-SSFP for fMRI in most practical situations. If dynamic averaging in the parenchyma were to be the dominant contrast mechanism then TR should be increased to eliminate the intravascular contribution, and TE reduced to eliminate static dephasing. Both options have highly negative consequences for the efficiency and sensitivity of the sequence.

Chapter 9: Feasibility and signal features of laminar GE-BOLD based fMRI at 1.5 T, 3 T and 7 T

The last part of the thesis tackled the feasibility of high resolution BOLD studies at field strengths lower than 7 T. The acquisition of cortical depth resolved activation signal requires submillimeter voxel sizes, especially at such thin and convoluted cortices as the visual cortex. In order to obtain a higher SNR and the predicted increased microvascular weighting of the BOLD activation signal, 7 T has become the workhorse to measure laminar fMRI. If the BOLD signal is averaged over a patch of cortex, then the SNR is further improved, at the cost of a loss of resolution along the cortical surface. This work studied GE-BOLD activation profiles obtained using this averaging approach at 1.5 T, 3 T and 7 T to study the feasibility of layer specific fMRI at field strengths lower than 7 T.

The activation profiles obtained were compared in terms of functional contrast and as a function of TE. The shapes of the activation profiles were similar if equivalent TEs were compared. In addition, after averaging over a patch of cortex, BOLD-like physiological noise dominated at all fields and CNR was largely echo time and field strength independent, although the acquisition at 7 T was most efficient. The cortical extent over which it was necessary to average until physiological noise dominated varied between 100 and 250 voxels (for 7 T and 1.5 T, respectively) for a voxel size of 0.75^3 mm^3. The extent decreased with increasing field, although the inter-subject variability was larger than the difference between fields in this study. This extent will depend on the image SNR and the amount of physiological noise in the signal after physiological correction, but the results in this study suggest that if the experimental conditions allow, it is possible to perform layer specific fMRI at field strengths lower than 7 T that are more widely available for human scans.

10.2   Discussion

The acquisition of experimental data throughout this thesis served the purpose of understanding the laminar specificity of the GE-BOLD signal. That is why temporal resolution was sacrificed for spatial resolution and limited distortion artefacts. The results obtained provide valuable insights to assess the laminar specificity of the T_2^*- BOLD signal.

The deconvolution with the estimated physiological point spread function led to laminar profiles without a strong ascending component for both the 3D-FLASH dataset (with a prohibitively long TR) and the 3D-EPI dataset with a temporal resolution of about ~6 s, which is closer to temporal resolutions routinely used

in neuroscience (1-4 s). In addition, Uludağ's group applied the deconvolution approach to activation profiles in the visual cortex obtained with a temporal resolution of ~3 seconds and reached the same conclusion *Marquardt et al.* (2018). These results show that the deconvolution approach proposed is, as expected, valid for GE- BOLD based acquisitions, independent of the image acquisition sequence and temporal resolution, provided that the cortex is in a steady state, which will be the case for stimuli longer than 1 s.

Deconvolving GE-BOLD profiles will result in profiles with increased laminar specificity. This is of particular interest for studying intracortical connectivity, because the increased laminar specificity is expected to lead to an increased sensitivity to detect interactions between cortical regions. In addition, calibrated laminar fMRI (*Guidi et al.*, 2016; *Zappe et al.*, 2008) will also benefit from the increased laminar specificity. After deconvolution, BOLD signal changes and blood flow/blood volume changes, to which BOLD is related to in the Davis model, will be weighted towards microvasculature. As a result, the estimation of oxygen consumption should be more accurate.

Other approaches that aim at correcting or reducing the effects of interlaminar leakage include using a differential paradigm (*Kashyap et al.*, 2017; *Sánchez Panchuelo et al.*, 2015), measuring the early response of the BOLD activation (*Siero et al.*, 2011, 2013, 2015) or to regress out the laminar time-course from layers upstream (*Kok et al.*, 2016). Compared to the deconvolution approach, the differential approach is less efficient and cannot fully eliminate the contribution from intracortical veins. Measuring the early laminar response requires high temporal and spatial resolution, which dramatically affects SNR and coverage. The regression approach will detect only the variance that is unique to the layer; any shared variance, including that that may be neuronal in origin because the activity spreads over more than one layer, will be regressed out. The disadvantage of the deconvolution approach with respect to these approaches is that it relies on the cortical vasculature being similar enough to the developed model, which will not be the case in, for example, diseases in which brain vascularization is altered.

This thesis described the features of cortical profiles in a modelled ideal setting and in a real experimental environment. In the latter, data have been analysed using standard approaches using open-source software for neuroimaging. It is expected, that the laminar specificity of the measured profiles will be improved as software tools capable of performing an accurate cortical segmentation and/or co-registration are developed. Regarding the extraction of the laminar profiles, the so-called equidistant approach for cortical layering was used throughout this thesis. As observed by *Bok* (1926), the thickness of a layer varies among gyri and sulci, but its volume is preserved. Hence, the equi-volume approach for cortical lamination (*Waehnert et al.*, 2013) is expected to deliver profiles with an improved laminar specificity. However, this does not put into questions the results obtained

in this work using the equidistant approach as studies that compared the two approaches obtained only slightly smoother profiles for the equidistant approach (*Kemper et al.*, 2017; *Kok et al.*, 2016).

There are several topics, specific and general, that future work could focus on. Regarding the deconvolution approach, it needs to be tested in different regions, correcting the p2t for different cortical thicknesses. It could also be expanded to include temporal dynamics that capture propagation through the cortex to measure layer specific BOLD signal transients or the response to event-like stimuli. On another topic, at the high-resolutions used in laminar fMRI, microscopic head motion during the scan will blur the image and will result in smoother profiles. Therefore, it would be beneficial to use some form of motion tracking, be it camera based or using navigators. The motion tracking can be used either prospectively or retrospectively using fat navigators (*Gallichan et al.*, 2016). The increase in acquisition time is marginal, although in its current form it needs to be reconstructed offline using the raw data of each channel, which can be time-consuming for long scans. Lastly, laminar segmentation would be most reliable if performed on a single-subject basis and not on an average regional laminar distribution, for which MR histology methods *in-vivo* need to be successfully developed (*Weiskopf et al.*, 2015).

In summary, this thesis proposes a method to obtain cortical profiles with reduced interlaminar leakage while still benefitting from the higher efficiency of GE-BOLD acquisitions, first. Then, it shows that the S2-SSFP approach is not well-suited to deliver T_2-like contrast for high resolution fMRI in acceptable acquisition times. Lastly, it shows that if the experimental question allows averaging over a patch of cortex and can accommodate a lower temporal efficiency, laminar fMRI can be performed at static field strengths lower than 7 T.

Bibliography

Andrews, B. T., M. Dujovny, H. G. Mirchandani, and J. I. Ausman, Microsurgical anatomy of the venous drainage into the superior sagittal sinus, *Neurosurgery*, *24*(4), 514–520, 1989.

Balasubramanian, M., R. V. Mulkern, W. M. Wells, P. Sundaram, and D. B. Orbach, Magnetic resonance imaging of ionic currents in solution: the effect of magnetohydrodynamic flow, *Magnetic Resonance in Medicine*, *74*, 1145–1155, 2016.

Barth, M., and E. Moser, Proton NMR relaxation times of human blood samples at 1.5 T and implications for functional MRI, *Cellular and molecular biology*, *43*, 783–791, 1997.

Barth, M., and D. G. Norris, Very high-resolution three-dimensional functional MRI of the human visual cortex with elimination of large venous vessels, *NMR in Biomedicine*, *477-484*, 2007.

Barth, M., H. Meyer, S. A. R. Kannengiesser, J. R. Polimeni, L. L. Wald, and D. G. Norris, T_2-weighted 3D fMRI using S2-SSFP at 7 tesla, *Magnetic Resonance in Medicine*, *63*, 1015–1020, 2010.

Blockley, N. P., L. Jiang, A. G. Gardener, C. N. Ludman, S. T. Francis, and P. a. Gowland, Field strength dependence of R_1 and R_2^* relaxivities of human whole blood to ProHance, Vasovist, and deoxyhemoglobin, *Magnetic Resonance in Medicine*, *60*, 1313–20, 2008.

Blockley, N. P., V. E. M. Griffeth, A. B. Simon, and R. B. Buxton, A review of calibrated blood oxygenation level-dependent (BOLD) methods for the measurement of task-induced changes in brain oxygen metabolism, *NMR in Biomedicine*, *26*, 987–1003, 2013.

Boas, D. a., S. R. Jones, A. Devor, T. J. Huppert, and A. M. Dale, A vascular anatomical network model of the spatio-temporal response to brain activation, *Neuroimage*, *40*, 1116–29, 2008.

Bok, S., Gibt es einen gemeinsamen bauplan in den kernen-und bahnen-systemen der verschiedenen querschnitte des neuralrohres?, *Zeitschrift für die gesamte Neurologie und Psychiatrie*, *100*(1), 678–699, 1926.

Bonaiuto, J. J., H. E. Rossiter, S. S. Meyer, N. Adams, S. Little, M. F. Callaghan, F. Dick, S. Bestmann, and G. R. Barnes, Non-invasive laminar inference with MEG: Comparison of methods and source inversion algorithms, *Neuroimage*, *167*, 372–383, 2018.

Boorman, L., A. J. Kennerley, D. Johnston, M. Jones, Y. Zheng, P. Redgrave, and J. Berwick, Negative Blood Oxygen Level Dependence in the Rat:A Model for Investigating the Role of Suppression in Neurovascular Coupling, *Journal of Neuroscience*, *30*, 4285–4294, 2010.

Boxerman, J. L., L. M. Hamberg, B. R. Rosen, and R. M. Weisskoff, MR Contrast Due to Intravascular Magnetic-Susceptibility Perturbations, *Magnetic Resonance in Medicine*, *34*, 555–566, 1995.

Budde, J., G. Shajan, M. Zaitsev, K. Scheffler, and R. Pohmann, Functional MRI in human subjects with gradient-echo and spin-echo EPI at 9.4 T, *Magnetic Resonance in Medicine*, *71*, 209–18, 2014.

Burkhalter, A., and K. L. Bernardo, Organization of corticocortical connections in human visual cortex, *Neurobiology*, *86*, 1071–1075, 1989.

Buxton, R. B., The elusive initial dip, *Neuroimage*, *13*, 953–958, 2001.

Buxton, R. B., *Introduction to Functional Magnetic Resonance Imaging: Principles and Techniques*, Cambridge University Press, 2009.

Buxton, R. B., E. C. Wong, and L. R. Frank, Dynamics of blood flow and oxygenation changes during brain activation: the ballon model, *Magnetic Resonance in Medicine*, *39*, 855–864, 1998.

Buxton, R. B., V. E. M. Griffeth, A. B. Simon, F. Moradi, and A. Shmuel, Variability of the coupling of blood flow and oxygen metabolism responses in the brain: a problem for interpreting BOLD studies but potentially a new window on the underlying neural activity, *Frontiers in neuroscience*, *8*, 139, 2014.

Calamante, F., Arterial input function in perfusion MRI: a comprehensive review, *Progress in nuclear magnetic resonance spectroscopy*, *74*, 1–32, 2013.

Cassot, F., F. Lauwers, C. Fouard, S. Prohaska, and V. Lauwers-Cances, A novel three-dimensional computer-assisted method for a quantitative study of microvascular networks of the human cerebral cortex, *Microcirculation*, *13*, 1–18, 2006.

Chen, G., F. Wang, J. C. Gore, and A. W. Roe, Layer-specific BOLD activation in awake monkey V1 revealed by ultra-high spatial resolution functional magnetic resonance imaging, *Neuroimage*, *64*, 147–55, 2013.

Chen, J. J., and G. B. Pike, BOLD-specific cerebral blood volume and blood flow

changes during neuronal activation in humans, *NMR in Biomedicine*, *22*, 1054–62, 2009.

Cheng, K., R. a. Waggoner, and K. Tanaka, Human ocular dominance columns as revealed by high-field functional magnetic resonance imaging, *Neuron*, *32*, 359–374, 2001.

Cox, E., and P. Gowland, Measuring T_2 and T_2' in the brain at 1.5 T, 3T and 7T using a hybrid gradient echo-spin echo sequence and EPI, in *Proceedings of the International Society of Magnetic Resonance in Medicine*, vol. 16, 2008.

Cox, R. W., AFNI: Software for Analysis and Visualization of Functional Magnetic Resonance Neuroimages, *Computers and Biomedical research*, *29*, 162–173, 1996.

Crémillieux, Y., S. Ding, and J. F. Dunn, High-resolutionin vivo measurements of transverse relaxation times in rats at 7 Tesla, *Magnetic Resonance in Medicine*, *39*, 285–290, 1998.

Dale, A. M., B. Fischl, and M. I. Sereno, Cortical surface-based analysis. I. Segmentation and surface reconstruction, *Neuroimage*, *9*, 179–94, 1999.

Davis, T. L., K. K. Kwong, R. M. Weisskoff, and B. R. Rosen, Calibrated functional MRI: mapping the dynamics of oxidative metabolism, *Proceedings of the National Academy of Sciences*, *95*, 1834–9, 1998.

De Martino, F., J. Zimmermann, L. Muckli, K. Uğurbil, E. Yacoub, and R. Goebel, Cortical depth dependent functional responses in humans at 7T: improved specificity with 3D GRASE, *PLoS One*, *8(3)*(e60514), 2013.

De Martino, F., M. Moerel, K. Uğurbil, R. Goebel, E. Yacoub, and E. Formisano, Frequency preference and attention effects across cortical depths in the human primary auditory cortex, *Proceedings of the National Academy of Sciences*, *112*, 16,036–16,041, 2015.

de Sousa, A. a., C. C. Sherwood, A. Schleicher, K. Amunts, C. E. MacLeod, P. R. Hof, and K. Zilles, Comparative cytoarchitectural analyses of striate and extrastriate areas in hominoids, *Cerebral Cortex*, *20*, 966–81, 2010.

Donahue, M. J., H. Hoogduin, P. C. M. van Zijl, P. Jezzard, P. R. Luijten, and J. Hendrikse, Blood oxygenation level-dependent (BOLD) total and extravascular signal changes and delta R_2^* in human visual cortex at 1.5, 3.0 and 7.0 T, *NMR in Biomedicine*, *24*, 25–34, 2011.

Douglas, R. J., and K. A. C. Martin, Neuronal circuits of the neocortex, *Annual Review of Neuroscience*, *27*, 419–51, 2004.

Drew, P. J., A. Y. Shih, and D. Kleinfeld, Fluctuating and sensory-induced vasody-

namics in rodent cortex extend arteriole capacity, *Proceedings of the National Academy of Sciences*, *108*, 8473–8478, 2011.

Duong, T. Q., A. C. Silva, S.-P. Lee, and S.-G. Kim, Functional MRI of calcium-dependent synaptic activity: cross correlation with CBF and BOLD measurements, *Magnetic Resonance in Medicine*, *43*(3), 383–392, 2000.

Duvernoy, H. M., S. Delon, and J. L. Vannson, Cortical blood vessels of the human brain, *Brain research bulletin*, *7*, 519–79, 1981.

Ehses, P., J. Budde, G. Shajan, and K. Scheffler, T_2-weighted BOLD fMRI at 9.4 T using a S2-SSFP-EPI sequence, in *Proceedings of the International Society of Magnetic Resonance in Medicine*, vol. 21, 2013.

Engel, S. A., G. H. Glover, and B. A. Wandell, Retinotopic organization in human visual cortex and the spatial precision of functional mri., *Cerebral cortex*, *7*(2), 181–192, 1997.

Felleman, D. J., and D. C. Van Essen, Distributed hierarchical processing in the primate cerebral cortex, *Cerebral Cortex*, *1*, 1–47, 1991.

Fischl, B., and A. M. Dale, Measuring the thickness of the human cerebral cortex from magnetic resonance images, *Proceedings of the National Academy of Sciences*, *97*(20), 11,050–11,055, 2000.

Fracasso, A., N. Petridou, and S. O. Dumoulin, Distinct BOLD laminar profiles elicited by retino-cortical and inter-hemispheric sources in human early visual cortex, in *Proceedings of the International Society of Magnetic Resonance in Medicine*, vol. 22, 2014.

Fracasso, A., P. R. Luijten, S. O. Dumoulin, and N. Petridou, Laminar imaging of positive and negative BOLD in human visual cortex at 7T, *Neuroimage*, pp. 1–12, 2017.

Friston, K. J., C. Buechel, G. R. Fink, J. Morris, E. Rolls, and R. J. Dolan, Psychophysiological and modulatory interactions in neuroimaging, *Neuroimage*, *6*, 218–229, 1997.

Friston, K. J., L. Harrison, and W. Penny, Dynamic causal modelling, *Neuroimage*, *19*, 1273–1302, 2003.

Gagnon, L., et al., Quantifying the microvascular origin of BOLD-fMRI from first principles with two-photon microscopy and an oxygen-sensitive nanoprobe, *Journal of Neuroscience*, *35*(8), 3663–3675, 2015.

Gallichan, D., J. P. Marques, and R. Gruetter, Retrospective correction of involuntary microscopic head movement using highly accelerated fat image navigators (3D FatNavs) at 7T, *Magnetic resonance in medicine*, *75*(3), 1030–1039, 2016.

Gati, J. S., R. S. Menon, K. Uğurbil, and B. K. Rutt, Experimental determination of the BOLD field strength dependence in vessels and tissue, *Magnetic Resonance in Medicine*, *38*, 296–302, 1997.

Goa, P. E., B. A. Poser, and M. Barth, Modeling and suppression of respiration induced B0-fluctuations in non-balanced steady-state free precession sequences at 7 Tesla, *Magnetic Resonance Materials in Physics, Biology and Medicine*, *26*(4), 377–387, 2013.

Goa, P. E., P. J. Koopmans, B. A. Poser, M. Barth, and D. G. Norris, BOLD fMRI signal characteristics of S1- and S2-SSFP at 7 Tesla, *Frontiers in neuroscience*, *8*, 1–6, 2014.

Goebel, R., Analysis of functional MRI data, in *From Nuclear Spins to Brain Functions*, edited by K. Uludağ, K. Uğurbil, and L. Berliner, Springer US, 2015.

Goense, J., H. Merkle, and N. K. Logothetis, High-resolution fMRI reveals laminar differences in neurovascular coupling between positive and negative BOLD responses, *Neuron*, *76*, 629–39, 2012.

Goense, J., Y. Bohraus, and N. K. Logothetis, fMRI at High Spatial Resolution: Implications for BOLD-Models, *Magnetic Resonance Materials in Physics, Biology and Medicine*, *10*, 1–13, 2016.

Goense, J. B. M., and N. K. Logothetis, Laminar specificity in monkey V1 using high-resolution SE-fMRI, *Magnetic resonance imaging*, *24*, 381–92, 2006.

Golay, X., J. Hendrikse, and T. C. C. Lim, Perfusion Imaging Using Arterial Spin Labeling, *Topics in Magnetic Resonance Imaging*, *15*, 10–27, 2004.

Greve, D. N., and B. Fischl, Accurate and robust brain image alignment using boundary-based registration, *Neuroimage*, *48*(1), 63–72, 2009.

Griffeth, V. E. M., A. B. Simon, and R. B. Buxton, The coupling of cerebral blood flow and oxygen metabolism with brain activation is similar for simple and complex stimuli in human primary visual cortex, *Neuroimage*, *104*, 156–162, 2014.

Grubb, R. L., M. E. Raichle, J. O. Eichling, and M. M. Ter-Pogossian, The Effects of Changes in PaCO2 Cerebral Blood Volume, Blood Flow, and Vascular Mean Transit Time, *Stroke*, *5*, 630–639, 1974.

Guidi, M., L. Huber, L. Lampe, C. J. Gauthier, and H. E. Moeller, Lamina-dependent calibrated BOLD response in human primary motor cortex, *Neuroimage*, *141*, 250–261, 2016.

Gyngell, M. L., The application of steady-state free precession in rapid 2DFT

NMR imaging: FAST and CE-FAST sequences, *Magnetic resonance imaging*, *6*(4), 415–419, 1988.

Hall, C. N., et al., Capillary pericytes regulate cerebral blood flow in health and disease, *Nature*, *508*, 55–60, 2014.

Harel, N., J. Lin, S. Moeller, K. Uğurbil, and E. Yacoub, Combined imaging-histological study of cortical laminar specificity of fMRI signals, *Neuroimage*, *29*, 879–87, 2006a.

Harel, N., K. Uğurbil, K. Uludağ, and E. Yacoub, Frontiers of brain mapping using MRI, *Journal of Magnetic Resonance Imaging*, *23*, 945–957, 2006b.

Harmer, J., R. M. Sánchez Panchuelo, R. Bowtell, and S. T. Francis, Spatial location and strength of BOLD activation in high-spatial-resolution fMRI of the motor cortex: a comparison of spin echo and gradient echo fMRI at 7T, *NMR in Biomedicine*, *25*, 717–25, 2012.

Heidemann, R. M., D. Ivanov, R. Trampel, F. Fasano, H. Meyer, J. Pfeuffer, and R. Turner, Isotropic submillimeter fMRI in the human brain at 7 T: Combining reduced field-of-view imaging and partially parallel acquisitions, *Magnetic Resonance in Medicine*, *68*, 1506–1516, 2012.

Hillman, E. M. C., A. Devor, M. B. Bouchard, A. K. Dunn, G. W. Krauss, J. Skoch, B. J. Bacskai, A. M. Dale, and D. a. Boas, Depth-resolved optical imaging and microscopy of vascular compartment dynamics during somatosensory stimulation, *Neuroimage*, *35*, 89–104, 2007.

Hoogenraad, F. G. C., P. J. W. Pouwels, M. B. M. Hofman, J. R. Reichenbach, M. Sprenger, and E. M. Haacke, Quantitative Differentiation Between BOLD Models in fMRI, *Magnetic Resonance in Medicine*, *246*, 233–246, 2001.

Horton, J. C., *Cytochrome oxidase patches: a new cytoarchitectonic feature of monkey visual cortex*, Philosophical Transactions of the Royal Society of London. B, Biological Sciences, 1984.

Hu, X., and E. Yacoub, The story of the initial dip in fMRI, *Neuroimage*, *62*, 1103–1108, 2012.

Hubel, D. H., and T. N. Wiesel, Receptive fields of single neurones in the cat's striate cortex, *The Journal of physiology*, *148*(3), 574–591, 1959.

Huber, L., Mapping Human Brain Activity by Functional Magnetic Resonance Imaging of Blood Volume, Ph.D. thesis, University of Leipzig, 2014.

Huber, L., D. Ivanov, S. N. Krieger, M. N. Streicher, T. Mildner, B. A. Poser, H. E. Möller, and R. Turner, Slab-selective, BOLD-corrected VASO at 7 Tesla provides measures of cerebral blood volume reactivity with high signal-to-noise ratio, *Magnetic resonance in medicine*, *72*(1), 137–148, 2014.

Huber, L., S. Marrett, D. A. Handwerker, A. Thomas, B. Gutierrez, D. Ivanov, B. A. Poser, and P. A. Bendettini, Fast dynamic measurement of functional T_1 and grey matter thickness changes during brain activation at 7T, in *Proceedings of the International Society of Magnetic Resonance in Medicine*, 2016.

Huber, L., K. Uludağ, and H. E. Möller, Non-BOLD contrast for laminar fMRI in humans: CBF, CBV, and $CMRO_2$, *Neuroimage*, pp. 1–19, 2017a.

Huber, L., D. Ivanov, D. A. Handwerker, S. Marrett, M. Guidi, K. Uludağ, P. A. Bandettini, and B. A. Poser, Techniques for blood volume fMRI with VASO: From low-resolution mapping towards sub-millimeter layer-dependent applications, *Neuroimage*, *164*, 131–143, 2018.

Huber, L., et al., Cortical lamina-dependent blood volume changes in human brain at 7T, *Neuroimage*, *107*, 23–33, 2015.

Huber, L., et al., High-Resolution CBV-fMRI Allows Mapping of Laminar Activity and Connectivity of Cortical Input and Output in Human M1, *Neuron*, pp. 1253–1263, 2017b.

Huettel, S. A., *Functional Magnetic Resonance Imaging, in: Functional Magnetic Resonance Imaging*, Oxford University Press Inc, 2004.

Huo, B.-X., Y.-R. Gao, and P. J. Drew, Quantitative separation of arterial and venous cerebral blood volume increases during voluntary locomotion, *Neuroimage*, *105*, 369–379, 2015.

Ivanov, D., B. A. Poser, S. S. Kashyap, A. Gardumi, L. Huber, and K. Uludağ, Sub-millimeter human brain perfusion imaging using arterial spin labelling at 3 and 7 Tesla, *Proceedings of the High Field Meeting of the International Society of Magnetic Resonance in Medicine*, *14*, 2016.

Jin, T., and S. Kim, Improved cortical-layer specificity of vascular space occupancy fMRI with slab inversion relative to spin-echo BOLD at 9.4 T, *Neuroimage*, *40*, 59–67, 2008a.

Jin, T., and S. Kim, Cortical layer-dependent dynamic blood oxygenation, cerebral blood flow and cerebral blood volume responses during visual stimulation, *Neuroimage*, *43*, 1–9, 2008b.

Jochimsen, T. H., D. G. Norris, T. Mildner, and H. E. Möller, Quantifying the intra- and extravascular contributions to spin-echo fMRI at 3 T, *Magnetic Resonance in Medicine*, *52*, 724–32, 2004.

Jones, M., N. Hewson-Stoate, J. Martindale, P. Redgrave, and J. Mayhew, Non-linear coupling of neural activity and CBF in rodent barrel cortex, *Neuroimage*, *22*, 956–965, 2004.

Kashyap, S., D. Ivanov, M. Havlicek, B. A. Poser, and K. Uludağ, High-resolution

T_1-mapping using inversion-recovery EPI and application to cortical depth-dependent fMRI at 7 Tesla, in *Proceedings of the International Society of Magnetic Resonance in Medicine*, Singapore, 2016.

Kashyap, S., D. Ivanov, M. Havlicek, B. A. Poser, and K. Uludağ, Impact of acquisition and analysis strategies on cortical depth-dependent fMRI, *Neuroimage*, 2017.

Kemper, V. G., F. De Martino, A. T. Vu, B. A. Poser, D. A. Feinberg, R. Goebel, and E. Yacoub, Sub-millimeter T_2 weighted fMRI at 7 T: comparison of 3D-GRASE and 2D SE-EPI, *Frontiers in neuroscience*, *9*, 163, 2015.

Kemper, V. G., F. De Martino, T. C. Emmerling, E. Yacoub, and R. Goebel, High resolution data analysis strategies for mesoscale human functional MRI at 7 and 9.4T, *Neuroimage*, 2017.

Kim, S.-G., E. Rostrup, H. B. Larsson, S. Ogawa, and O. B. Paulson, Determination of relative CMRO$_2$ from CBF and BOLD changes: significant increase of oxygen consumption rate during visual stimulation, *Magnetic Resonance in Medicine*, *41*(6), 1152–1161, 1999.

Kim, T., and S. Kim, Temporal dynamics and spatial specificity of arterial and venous blood volume changes during visual stimulation: implication for BOLD quantification, *Journal of Cerebral Blood Flow & Metabolism*, *31*, 1211–1222, 2011.

Kim, T., K. S. Hendrich, K. Masamoto, and S.-G. Kim, Arterial versus total blood volume changes during neural activity-induced cerebral blood flow change: implication for BOLD fMRI, *Journal of Cerebral Blood Flow & Metabolism*, *27*(6), 1235–1247, 2007.

Kok, P., L. J. Bains, T. van Mourik, D. G. Norris, and F. P. de Lange, Selective activation of the deep layers of the human primary visual cortex by top-down feedback, *Current Biology*, *26*(3), 371–376, 2016.

Koopmans, P., S. Orzada, M. Barth, and D. Norris, Distinguishing pial and laminar gradient-echo BOLD signals at 7 Tesla, in *Int Soc. Magn. Reson. Med.*, vol. 17, p. 1558, 2009.

Koopmans, P. J., M. Barth, and D. G. Norris, Layer-specific BOLD activation in human V1, *Human Brain Mapping*, *31*, 1297–1304, 2010.

Koopmans, P. J., M. Barth, S. Orzada, and D. G. Norris, Multi-echo fMRI of the cortical laminae in humans at 7 T, *Neuroimage*, *56*, 1276–85, 2011.

Kruger, G., and G. H. Glover, Physiological Noise in Oxygenation-Sensitive Magnetic Resonance Imaging, *Magnetic Resonance in Medicine*, *637*, 631–637, 2001.

Lauwers, F., F. Cassot, V. Lauwers-Cances, P. Puwanarajah, and H. Duvernoy, Morphometry of the human cerebral cortex microcirculation: general characteristics and space-related profiles, *Neuroimage*, *39*, 936–48, 2008.

Lawrence, S. J. D., E. Formisano, L. Muckli, and F. P. de Lange, Laminar fMRI: Applications for cognitive neuroscience, *Neuroimage*, pp. 1–7, 2017.

Lee, S. P., A. C. Silva, K. Uğurbil, and S. G. Kim, Diffusion-weighted spin-echo fMRI at 9.4 T: Microvascular/tissue contribution to BOLD signal changes, *Magnetic Resonance in Medicine*, *42*, 919–928, 1999.

Logothetis, N. K., J. Pauls, M. Augath, and T. O. Trinath, Neurophysiological investigation of the basis of the fMRI signal, *Nature*, *412*, 150–7, 2001.

Lorthois, S., F. Cassot, and F. Lauwers, Simulation study of brain blood flow regulation by intra-cortical arterioles in an anatomically accurate large human vascular network: Part I: methodology and baseline flow, *Neuroimage*, *54*, 1031–42, 2011.

Lu, H., X. Golay, J. J. Pekar, and P. C. M. Van Zijl, Functional magnetic resonance imaging based on changes in vascular space occupancy, *Magnetic Resonance in Medicine*, *50*, 263–274, 2003.

Lu, H., S. Patel, F. Luo, S. J. Li, C. J. Hillard, B. D. Ward, and J. S. Hyde, Spatial correlations of laminar BOLD and CBV responses to rat whisker stimulation with neuronal activity localized by Fos expression, *Magnetic Resonance in Medicine*, *52*, 1060–1068, 2004.

Lutti, A., D. L. Thomas, C. Hutton, and N. Weiskopf, High-resolution functional MRI at 3 T: 3D/2D echo-planar imaging with optimized physiological noise correction, *Magnetic Resonance in Medicine*, *69*, 1657–1664, 2013.

Maass, A., et al., Laminar activity in the hippocampus and entorhinal cortex related to novelty and episodic encoding, *Nature communications*, *5*, 5547, 2014.

Markuerkiaga, I., M. Barth, and D. G. Norris, A cortical vascular model for examining the specificity of the laminar BOLD signal, *Neuroimage*, *132*, 491–498, 2016.

Marquardt, I., M. Schneider, O. F. Gulban, D. Ivanov, and K. Uludağ, Cortical depth profiles of luminance contrast responses in human V1 and V2 using 7 T fMRI, *Human Brain Mapping*, pp. 1–16, 2018.

Marques, J. P., and D. G. Norris, How to choose the right MR sequence for your research question at 7T and above?, *Neuroimage*, pp. 1–22, 2017.

Marques, J. P., D. Khabipova, and R. Gruetter, Studying cyto and myeloarchitecture of the human cortex at ultra-high field with quantitative imaging: R_1, R_2^* and magnetic susceptibility, *Neuroimage*, *147*, 152–163, 2017.

Menon, R. S., S. Ogawa, J. P. Strupp, and K. Uğurbil, Ocular dominance in human V1 demonstrated by functional magnetic resonance imaging, *Journal of neurophysiology*, *77*(5), 2780–2787, 1997.

Mountcastle, V. B., Modality and topographic properties of single neurons of cat's somatic sensory cortex, *Journal of neurophysiology*, *20*(4), 408–434, 1957.

Muckli, L., F. De Martino, L. Vizioli, L. S. Petro, F. W. Smith, K. Uğurbil, R. Goebel, and E. Yacoub, Contextual Feedback to Superficial Layers of V1, *Current Biology*, *25*, 2690–2695, 2015.

Mullinger, K. J., S. D. Mayhew, A. P. Bagshaw, R. Bowtell, and S. T. Francis, Poststimulus undershoots in cerebral blood flow and BOLD fMRI responses are modulated by poststimulus neuronal activity, *Proceedings of the National Academy of Sciences*, *110*(33), 13,636–13,641, 2013.

Norris, D. G., Principles of magnetic resonance assessment of brain function, *Journal of Magnetic Resonance Imaging*, *23*, 794–807, 2006.

Norris, D. G., *Pulse Sequences for fMRI, in: FMRI: From Nuclear Spins to Brain Functions*, Springer, pp. 131-162, 2015.

Norris, D. G., P. J. Koopmans, R. Boyacioglu, and M. Barth, Power independent of number of slices (PINS) radiofrequency pulses for low-power simultaneous multislice excitation, *Magnetic Resonance in Medicine*, *66*, 1234–1240, 2011.

Obata, T., T. T. Liu, K. L. Miller, W. Luh, E. C. Wong, L. R. Frank, and R. B. Buxton, Discrepancies between BOLD and flow dynamics in primary and supplementary motor areas: application of the balloon model to the interpretation of BOLD transients, *Neuroimage*, *21*, 144–153, 2004.

Ogawa, S., T. M. Lee, A. R. Kay, and D. W. Tank, Brain magnetic resonance imaging with contrast dependent on blood oxygenation, *Proceedings of the National Academy of Sciences*, *87*(24), 9868–9872, 1990.

Ogawa, S., R. Menon, D. Tank, S. Kim, H. Merkle, J. Ellermann, and K. Uğurbil, Functional brain mapping by blood oxygenation level-dependent contrast magnetic resonance imaging. A comparison of signal characteristics with a biophysical model, *Biophysical journal*, *64*(3), 803–812, 1993.

Ohliger, M. A., A. K. Grant, and D. K. Sodickson, Ultimate Intrinsic Signal-to-Noise Ratio for Parallel MRI: Electromagnetic Field Considerations, *Magnetic Resonance in Medicine*, *50*, 1018–1030, 2003.

Olman, C. A., N. Harel, D. A. Feinberg, S. He, P. Zhang, K. Uğurbil, and E. Yacoub, Layer-specific fMRI reflects different neuronal computations at different depths in human V1, *PLoS One*, *7*(e32536), 2012.

Park, J., I. Ronen, D. Kim, and K. Uğurbil, Spatial specificity of high resolution

gradient echo (GE) BOLD and spin echo (SE) BOLD fMRI in cat visual cortex at 9.4 T, in *Proceedings of the International Society of Magnetic Resonance in Medicine*, vol. 31, 2005a.

Park, S. H., T. Hayashi, and S. G. Kim, Determination of intracortical venous vessel density using venography at 9.4 T, in *Proceedings of the International Society of Magnetic Resonance in Medicine*, 13, 2005b.

Peters, A. M., M. J. Brookes, F. G. Hoogenraad, P. A. Gowland, S. T. Francis, P. G. Morris, and R. Bowtell, T_2^* measurements in human brain at 1.5, 3 and 7 T, *Magnetic resonance imaging*, *25*, 748–753, 2007.

Pohmann, R., O. Speck, and K. Scheffler, Signal-to-noise ratio and MR tissue parameters in human brain imaging at 3, 7, and 9.4 tesla using current receive coil arrays, *Magnetic Resonance in Medicine*, *75*, 801–809, 2016.

Polimeni, J. R., B. Fischl, D. N. Greve, and L. L. Wald, Laminar analysis of 7T BOLD using an imposed spatial activation pattern in human V1, *Neuroimage*, *52*, 1334–46, 2010.

Poplawsky, A. J., M. Fukuda, M. Murphy, and S. Kim, Layer-Specific fMRI Responses to Excitatory and Inhibitory Neuronal Activities in the Olfactory Bulb, *Journal of Neuroscience*, *35*, 15,263–15,275, 2015.

Poplawsky, A. J., M. Fukuda, B. m. Kang, J. H. Kim, M. Suh, and S. G. Kim, Dominance of layer-specific microvessel dilation in contrast-enhanced high-resolution fMRI: Comparison between hemodynamic spread and vascular architecture with CLARITY, *Neuroimage*, pp. 1–11, 2017a.

Poplawsky, A. J., M. Fukuda, and S. Kim, Foundations of layer-specific fMRI and investigations of neurophysiological activity in the laminarized neocortex and olfactory bulb of animal models, *Neuroimage*, in press, 2017b.

Poser, B., *Techniques for BOLD and blood volume weighted fMRI*, Radboud Universiteit, 2009.

Pruessmann, K. P., Parallel imaging at high field strength: synergies and joint potential, *Topics in Magnetic Resonance Imaging*, *15*, 237–244, 2004.

Puckett, A. M., K. M. Aquino, P. A. Robinson, M. Breakspear, and M. M. Schira, The spatiotemporal hemodynamic response function for depth-dependent functional imaging of human cortex, *Neuroimage*, *139*, 240–248, 2016.

Ress, D., G. H. Glover, J. Liu, and B. Wandell, Laminar profiles of functional activity in the human brain, *Neuroimage*, *34*, 74–84, 2007.

Reynaud, O., J. Jorge, R. Gruetter, J. P. Marques, and W. van der Zwaag, Influence of physiological noise on accelerated 2D and 3D resting state functional MRI data at 7 T, *Magnetic Resonance in Medicine*, *78*, 888–896, 2017.

Rockland, K. S., What do we know about laminar connectivity?, *Neuroimage*, pp. 1–13, 2017.

Sakadžić, S., et al., Large arteriolar component of oxygen delivery implies a safe margin of oxygen supply to cerebral tissue, *Nature communications*, *5*, 5734, 2014.

Sánchez Panchuelo, R. M., D. Schluppeck, J. Harmer, R. Bowtell, and S. Francis, Assessing the Spatial Precision of SE and GE-BOLD Contrast at 7 Tesla, *Brain topography*, *28*(1), 62–65, 2015.

Scheeringa, R., P. J. Koopmans, T. van Mourik, O. Jensen, and D. G. Norris, The relationship between oscillatory EEG activity and the laminar-specific BOLD signal, *Proceedings of the National Academy of Sciences*, *113*(24), 6761–6766, 2016.

Schmitt, F., M. K. Stehling, and R. Turner, *Echo-Planar Imaging Theory, Technique and Application*, Springer, 1998.

Setsompop, K., et al., Slice-Selective RF pulses for in-vivo B1+ Inhomogeneity Mitigation at 7 Tesla using Parallel RF Excitation with a 16- Element Coil, *Magnetic Resonance in Medicine*, *60*, 1422–1432, 2009.

Shipp, S., Structure and function of the cerebral cortex, *Current Biology*, *17*, R443–9, 2007.

Shmuel, A., E. Yacoub, J. Pfeuffer, P. F. Van De Moortele, G. Adriany, K. Uğurbil, and X. Hu, Negative BOLD response and its coupling to the positive response in the human brain, *Neuroimage*, *6*(13), 1005, 2001.

Shmuel, A., M. Augath, A. Oeltermann, and N. K. Logothetis, Negative functional MRI response correlates with decreases in neuronal activity in monkey visual area V1, *Nature neuroscience*, *9*, 569–577, 2006.

Shulman, R. G., and D. L. Rothman, *Brain energetics and neuronal activity: applications to fMRI and medicine*, John Wiley & Sons, 2005.

Siero, J. C. W., N. Petridou, H. Hoogduin, P. R. Luijten, and N. F. Ramsey, Cortical depth-dependent temporal dynamics of the BOLD response in the human brain., *Journal of Cerebral Blood Flow & Metabolism*, *31*, 1999–2008, 2011.

Siero, J. C. W., N. F. Ramsey, H. Hoogduin, D. W. J. Klomp, P. R. Luijten, and N. Petridou, BOLD specificity and dynamics evaluated in humans at 7 T: comparing gradient-echo and spin-echo hemodynamic responses, *PLoS One*, *8*(e54560), 2013.

Siero, J. C. W., J. Hendrikse, H. Hoogduin, N. Petridou, P. Luijten, and M. J. Donahue, Cortical depth dependence of the BOLD initial dip and poststimulus

undershoot in human visual cortex at 7 Tesla, *Magnetic Resonance in Medicine*, *73*, 2283–2295, 2015.

Silva, A. C., and A. P. Koretsky, Laminar specificity of functional MRI onset times during somatosensory stimulation in rat, *Proceedings of the National Academy of Sciences*, *99*(23), 15,182–15,187, 2002.

Smith, S. M., Fast robust automated brain extraction, *Human Brain Mapping*, *17*, 143–155, 2002.

Stüber, C., et al., Myelin and iron concentration in the human brain: A quantitative study of MRI contrast, *Neuroimage*, *93*, 95–106, 2014.

Thomson, A. M., and A. P. Bannister, Interlaminar connections in the neocortex, *Cerebral Cortex*, *13*, 5–14, 2003.

Tian, P., et al., Cortical depth-specific microvascular dilation underlies laminar differences in blood oxygenation level-dependent functional MRI signal, *Proceedings of the National Academy of Sciences*, *107*(34), 15,246–15,251, 2010.

Tootell, R., S. Hamilton, M. S. Silverman, and E. Switkes, Functional anatomy of macaque striate cortex. I. Ocular dominance, binocular interactions, and baseline conditions, *Journal of Neuroscience*, *8*, 1500–1530, 1988.

Trampel, R., P.-l. Bazin, A. Schäfer, R. M. Heidemann, D. Ivanov, G. Lohmann, S. Geyer, and R. Turner, Laminar-specific fingerprints of different sensorimotor areas obtained during imagined and actual finger tapping, in *Proceedings of the International Society of Magnetic Resonance in Medicine*, 2012.

Triantafyllou, C., R. D. Hoge, G. Krueger, C. J. Wiggins, A. Potthast, G. C. Wiggins, and L. L. Wald, Comparison of physiological noise at 1.5 T, 3 T and 7 T and optimization of fMRI acquisition parameters, *Neuroimage*, *26*, 243–50, 2005.

Triantafyllou, C., R. D. Hoge, and L. L. Wald, Effect of spatial smoothing on physiological noise in high-resolution fMRI, *Neuroimage*, *32*, 551–557, 2006.

Triantafyllou, C., J. R. Polimeni, and L. L. Wald, Physiological noise and signal-to-noise ratio in fMRI with multi-channel array coils, *Neuroimage*, *55*, 597–606, 2011.

Triantafyllou, C., J. R. Polimeni, B. Keil, and L. L. Wald, Coil-to-coil physiological noise correlations and their impact on functional MRI time-series signal-to-noise ratio, *Magnetic resonance in medicine*, *76*(6), 1708–1719, 2016.

Troebinger, L., J. D. Lopez, A. Lutti, S. Bestmann, and G. Barnes, Discrimination of cortical laminae using MEG, *Neuroimage*, *102*, 885–893, 2014.

Truong, T. K., A. Avram, and A. W. Song, Lorentz effect imaging of ionic currents in solution, *Journal of Magnetic Resonance*, *191*, 93–99, 2008.

Turner, R., How Much Cortex Can a Vein Drain? Downstream Dilution of Activation-Related Cerebral Blood Oxygenation Changes, *Neuroimage*, *16*, 1062–1067, 2002.

Uğurbil, K., et al., High Magnetic Fields for Imaging Cerebral Morphology, Function and Biochemistry, in *Ultra High Field Magnetic Resonance Imaging*, edited by P.-M. Robitaille and L. Berliner, Springer US, Boston, MA, pp. 285-343, 2006.

Uludağ, K., To dip or not to dip: Reconciling optical imaging and fMRI data, *Proceedings of the National Academy of Sciences*, *107*, E23–E23, 2010.

Uludağ, K., and P. Blinder, Linking brain vascular physiology to hemodynamic response in ultra-high field MRI, *Neuroimage*, *168*, 279–295, 2018.

Uludağ, K., B. Müller-Bierl, and K. Uğurbil, An integrative model for neuronal activity-induced signal changes for gradient and spin echo functional imaging, *Neuroimage*, *48*, 150–65, 2009.

Van de Moortele, P. F., K. Uğurbil, and S. Lehericy, Is T_2^* always the optimum echo time in BOLD FMRI? Challenging a common concept with a new contrast to noise ratio BOLD model, in *Proceedings of the International Society of Magnetic Resonance in Medicine*, p. p. 2464, 2008.

van der Zwaag, W., P. F. Buur, A. Fracasso, T. van Doesum, K. Uludağ, M. Versluis, and J. P. Marques, Distortion-matched T 1 maps and unbiased T 1 -weighted images as anatomical reference for high-resolution fMRI, *Neuroimage*, *176*, 41–55, 2018.

Van Zijl, P. C., S. M. Eleff, J. A. Ulatowski, J. M. Oja, A. M. UluÇ§, R. J. Traystman, and R. A. Kauppinen, Quantitative assessment of blood flow, blood volume and blood oxygenation effects in functional magnetic resonance imaging, *Nature medicine*, *4*(2), 159–167, 1998.

Vaughan, J. T., et al., 7T vs. 4T: RF power, homogeneity, and signal-to-noise comparison in head images, *Magnetic Resonance in Medicine*, *46*, 24–30, 2001.

Vazquez, A. L., M. Fukuda, J. C. Crowley, and S. Kim, Neural and Hemodynamic Responses Elicited by Forelimb- and Photo-stimulation in Channelrhodopsin-2 Mice: Insights into the Hemodynamic Point Spread Function, *Cerebral Cortex*, 2013.

Waehnert, M. D., J. Dinse, M. Weiss, M. N. Streicher, P. Waehnert, S. Geyer, R. Turner, and P.-l. Bazin, Anatomically motivated modeling of cortical laminae, *Neuroimage*, 2013.

Wald, L. L., and J. R. Polimeni, Impacting the effect of fMRI noise through hardware and acquisition choices : Implications for controlling false positive rates, *Neuroimage*, *154*, 15–22, 2017.

Wald, L. L., C. Triantafyllou, and R. D. Hoge, Field Strength Dependence of Contrast and Noise in fMRI, in *From Nuclear Spins to Brain Functions*, edited by K. Uludağ, K. Uğurbil, and L. Berliner, Springer US, 2015.

Wang, X.-J., and H. Kennedy, Brain structure and dynamics across scales: In search of rules, *Current opinion in neurobiology*, *37*, 92–98, 2016.

Weber, B., A. L. Keller, J. Reichold, and N. K. Logothetis, The microvascular system of the striate and extrastriate visual cortex of the macaque, *Cerebral Cortex*, *18*, 2318–30, 2008.

Weiskopf, N., S. Mohammadi, A. Lutti, and M. F. Callaghan, Advances in MRI-based computational neuroanatomy: from morphometry to in-vivo histology, *Current opinion in neurology*, *28*(4), 313–322, 2015.

Weisskoff, R. M., Simple measurement of scanner stability for functional NMR imaging of activation in the brain, *Magnetic Resonance in Medicine*, *36*, 643–5, 1996.

Yacoub, E., T. Q. Duong, P.-f. Van De Moortele, M. Lindquist, G. Adriany, S. Kim, K. Uğurbil, and X. Hu, Spin-echo fMRI in humans using high spatial resolutions and high magnetic fields, *Magnetic Resonance in Medicine*, *49*, 655–64, 2003.

Yacoub, E., A. Shmuel, N. Logothetis, and K. Uğurbil, Robust detection of ocular dominance columns in humans using Hahn Spin Echo BOLD functional MRI at 7 Tesla, *Neuroimage*, *37*, 1161–1177, 2007.

Yacoub, E., K. Uğurbil, and C. Olman, Feasibility of detecting differential layer specific activations in humans using SE BOLD fMRI at 7 T., in *Proceedings of the International Society of Magnetic Resonance in Medicine*, 1607, 2009.

Yacoub, E., et al., Imaging brain function in humans at 7 Tesla, *Magnetic Resonance in Medicine*, *45*(4), 588–594, 2001.

Yu, X., D. Glen, S. Wang, S. Dodd, Y. Hirano, Z. Saad, R. Reynolds, A. C. Silva, and A. P. Koretsky, Direct imaging of macrovascular and microvascular contributions to BOLD fMRI in layers IV-V of the rat whisker-barrel cortex, *Neuroimage*, *59*, 1451–60, 2012.

Yu, X., C. Qian, D. Chen, S. J. Dodd, and A. P. Koretsky, Deciphering laminar-specific neural inputs with line-scanning fMRI, *Nature Methods*, *11*, 55–8, 2014.

Zappe, A. C., J. Pfeuffer, H. Merkle, N. K. Logothetis, and J. B. Goense, The effect of labeling parameters on perfusion-based fMRI in nonhuman primates, *Journal of Cerebral Blood Flow & Metabolism*, *28*(3), 640–652, 2008.

Zelinski, A. C., L. M. Angelone, V. K. Goyal, G. Bonmassar, E. Adalsteinsson,

and L. L. Wald, Specific Absorption Rate Studies of the Parallel Transmission of Inner-Volume Excitations at 7 Tesla, *Journal of Magnetic Resonance Imaging*, *28*, 1005–1018, 2009.

Zhang, Y., M. Brady, and S. Smith, Segmentation of brain MR images through a hidden Markov random field model and the expectation-maximization algorithm, *IEEE transactions on medical imaging*, *20*(1), 45–57, 2001.

Zhao, F., P. Wang, and S. G. Kim, Cortical depth-dependent gradient-echo and spin-echo BOLD fMRI at 9.4T, *Magnetic Resonance in Medicine*, *51*, 518–24, 2004.

Zhao, F., P. Wang, K. Hendrich, K. Uğurbil, and S. G. Kim, Cortical layer-dependent BOLD and CBV responses measured by spin-echo and gradient-echo fMRI: Insights into hemodynamic regulation, *Neuroimage*, *30*, 1149–1160, 2006.

Zhao, J. M., C. S. Clingman, M. J. Närväinen, R. A. Kauppinen, and P. C. Van Zijl, Oxygenation and hematocrit dependence of transverse relaxation rates of blood at 3T, *Magnetic Resonance in Medicine*, *58*(3), 592–597, 2007.

Zheng, D., A.-s. LaMantia, and D. Purves, Specialized Vascularization of the Primate Visual Cortex, *Journal of Neuroscience*, pp. 2622–2629, 1991.

Zweifach, B. W., and H. H. Lipowsky, Quantitative studies of microcirculatory structure and function. III. Microvascular hemodynamics of cat mesentery and rabbit omentum, *Circulation research*, *41*(3), 380–390, 1977.

Appendix

Nederlandse samenvatting

Functionele magnetische resonantie beeldvorming, functionele MRI, is een niet-invasieve techniek om hersenactiviteit te meten. Hoewel het uiteindelijke doel het meten van neuronale activiteit is, meten de momenteel beschikbare MR-methoden de veranderingen die door neuronale activiteit geïnduceerd worden in de omliggende vasculatuur. Van een neuron wordt gezegd dat het actief is, wanneer het niveau van synaptische activiteit hoger is dan in zijn rusttoestand. Na activering neemt de energetische behoefte van neuronen toe, waardoor het verbruik van metabolieten en zuurstof toeneemt. Om te garanderen dat aan de verhoogde metabole vraag wordt voldaan, zetten de capillairen en slagaders in de nabijheid van het geactiveerde gebied uit, waardoor het bloedvolume en de -stroom naar het gebied toenemen. MRI kan een signaal meten dat de bloedstroom, het bloedvolume of het zuurstofverbruik in een regio weerspiegelt, en ook een signaal dat een combinatie is van deze drie parameters, het bloedzuurstofniveau-afhankelijke signaal (in het Engels Blood Oxygenation Level Dependent Signal, BOLD-signal).

Sinds het BOLD-signaal voor het eerst werd ontdekt in de vroege jaren '90, is dit de meest gebruikte methode om hersenactiviteit met MRI te meten. In vergelijking met de fysiologische parameters die we eerder noemden, is het gevoeliger-voor neuronale activering, het kan gemakkelijk worden gemeten met algemeen beschikbare software en MRI-apparatuur, en het maakt het mogelijk om een volledig hersenbeeld sneller te verkrijgen, in 2-3 seconden per beeld. Vergeleken met andere niet-MR-gebaseerde technieken om de hersenfunctie te meten (bijvoorbeeld elektro-encefalografie, magneto-encephalographie of positron emissie tomografie), is het belangrijkste voordeel de mate waarin alle hersengebieden weergegeven kunnen worden en de ruimtelijke resolutie die MRI kan bereiken. Met andere woorden, het is mogelijk om hersengebieden te meten die zich in het centrum van de hersenen bevinden en die een belangrijke rol spelen in sommige cognitieve processen (bijvoorbeeld de hippocampus, de amygdala en de thalamus) en het is gebruikelijk om te meten met een ruimtelijke resolutie van 3x3x3 mm^3.

Bij deze resoluties is het mogelijk om te identificeren welke regio's betrokken zijn bij het uitvoeren van een bepaalde taak zoals het maken van een onderscheid tussen echte en verzonnen woorden. Het is echter niet mogelijk om de interacties of hiërarchie tussen deze regio's vast te stellen, zonder een bepaald model van hersenfunctie te veronderstellen. Inderdaad vindt neuronale communicatie in milliseconden plaats, te snel om gemeten te worden met de MRI-methoden die tot nu toe beschikbaar zijn.

Het meten van hersenactivatie op het corticale laminaire niveau is een veelbelovende methode om de interactie tussen verschillende regio's te meten zonder een a priori model aan te nemen. De cortex is een ~ 3 mm dikke laag neuronen die zich over het hersenoppervlak uitstrekt. Het bevat neuronale cellichamen en is daarom het deel van de hersenen waar signalen verwerkt worden. Het is verdeeld in lagen en afhankelijk van de rol die een bepaalde regio heeft bij het verwerken van een taak, zal een bepaalde laag een sterkere activering vertonen dan andere, wat de inschatting van de interacties tussen regio's zal vergemakkelijken.

Gezien de kleine dikte van de cortex, is het noodzakelijk om te meten met resoluties van minder dan 1 mm. Wanneer alle andere relevante parameters voor het verkrijgen van een beeld onveranderd blijven, neemt de signaal-ruisverhouding met toenemende beeldresolutie in MRI af. Vanwege technische beperkingen was het in de eerste jaren van MRI niet mogelijk om de activering op het niveau van corticale lagen te meten. In de afgelopen 15 jaar zijn echter in toenemende mate high-field MRI-scanners beschikbaar gewordenen zijn er doorslaggevende verbeteringen aangebracht in de hardware en software die bij beeldacquisitie gebruikt worden . Als gevolg hiervan is het mogelijk geworden om beelden te verkrijgen met een hoge ruimtelijke resolutie en een voldoende signaal-ruisverhouding, terwijl de opnametijden acceptabel zijn voor toepassingen in de neurowetenschappen.

Het softwareprogramma of de code die in MRI wordt gebruikt om een afbeelding te verkrijgen, wordt een MR-sequentie genoemd. Hierin worden de vorm, de duur en de volgorde van de radiofrequentiepulsen en veranderingen in het magnetische veld omschreven, die toegepast moeten worden om een beeld te verkrijgen. De twee hoofdtypen van sequenties worden spin-echo (SE) en gradiënt-echo (GE) genoemd. Op BOLD gebaseerde activering wordt meestal gemeten met gradiënt-echosequenties omdat dit sneller eneenvoudiger is, en gevoeliger voor neuronale activering. Het belangrijkste nadeel is dat het grootste deel van het gemeten activeringssignaal afkomstig is van veneuze bloedvaten met een diameter groter dan 20 μm. Deze aders geven een verstrooiing van het activeringssignaal, dat tot enkele mm kan afwijken van de daadwerkelijke activeringslocatie. Als gevolg hiervan is de spatiale specificiteit van het gemeten activeringssignaal verminderd. In de eerste drie wetenschappelijke hoofdstukken van dit proefschrift

(Hoofdstukken 6, 7 en 8) wordt het effect van deze bloedvaten bestudeerd en gekwantificeerd en worden benaderingen voorgesteld om de verstoringte voorkomen. In het laatste wetenschappelijke hoofdstuk (hoofdstuk 9) wordt de haalbaarheid van laminaire op GE-BOLD gebaseerde fMRI bij magnetische veldsterkten onder 7 T bestudeerd. De belangrijkste bevindingen worden hierna in duidelijke bewoordingen beschreven.

Ten eerste zijn in **Hoofdstuk 6** het laminaire BOLD activeringssignaal en zijn ruimtelijke spreiding bestudeerd. Hiertoe is een model van corticale vasculatuur ontwikkeld. Dit model is gebaseerd op gepubliceerde anatomische en fysiologische onderzoeken en omvat de variatie van de microvasculatuur (samengesteld uit vaten met $\varnothing < 20\,\mu m$) en macrovasculatuur (samengesteld uit vaten met $\varnothing > 20\,\mu m$) in de cortex.

Dit model is gebruikt om spin- en gradiënt-echo-gebaseerde BOLD-activeringsprofielen in de cortex te simuleren. Deze profielen zijn vergelijkbaar met de profielen die experimenteel zijn verkregen. Het model is ook gebruikt om de fysiologische puntspreidingsfunctie (PSF) te schatten. Dat wil zeggen dat het effect is gekwantificeerd dat de activering in één laag heeft in de rest van de lagen. Het is een kenmerk van de corticale vasculatuur dat aders die loodrecht staan op het corticale oppervlak, bloed in één richting van diepere naar hogere lagen afvoeren. Daarom is de geschatte fysiologische PSF niet symmetrisch, maar gebogen richting het corticale oppervlak, waardoor een piek in de activeringslaag en een staart tot aan het corticale oppervlak die vrij constant blijft, getoond worden. . Het belangrijkste verschil tussen de fysiologische PSF van de verschillende lagen is de lengte van de staart, die korter is naarmate de laag zich dichter bij het corticale oppervlak bevindt.

De volgende logische stap, beschreven in **Hoofdstuk 7**, was om de opgedane kennis over de fysiologische puntspreidingsfunctie te gebruiken om te corrigeren voor de signaalspreiding tussen de lagen. Intuïtief kunnen de activeringsprofielen gemeten met MRI begrepen worden als het resultaat van het uitvoeren van de convolutie tussen het laminaire activeringsprofiel en de fysiologische PSF. Vandaar dat het middels het uitvoeren van het omgekeerde proces, de deconvolutie van het gemeten signaal met de fysiologische PSF, mogelijk zou moeten zijn om corticale activeringsprofielen te verkrijgen die vrij zijn van het effect van signaalspreiding tussen lagen. Deze aanpak is getest in twee verschillende datasets. In beide gevallen komen de verkregen profielen meer overeen met die verkregen met werkwijzen die minder last hebben van de spreiding van activeringssignaal tussen lagen (zoals spin-echo). Ten slotte wordt een benadering gegeven om de fysiologische PSF-parameter aan te passen aan een variërend aantal meetpuntenover de cortex, omdat dit aantal vaak varieert tussen verschillende laminaire onderzoeken. De nauwkeurigheid van de deconvolutiebenadering moet nog worden beoordeeld. Dit kan gedaan worden door gedeconvolueerde GE-BOLD corticale

activatieprofielen te vergelijken met profielen die in dezelfde scansessie en bij dezelfde of equivalente experimentele instellingen zijn verkregen met een methode die geen hinder ondervindt van signaalspreiding tussen lagen.

Indien mogelijk geniet het de voorkeur om te meten met een sequentie die geen hinder ondervindt van signaalspreiding tussen lagen, zoals spin-echo. Zoals eerder vermeld, is spin-echo BOLD minder gevoelig voor activering dan zijn tegenhanger, gradiënt-echo. Een optie om de gevoeligheid te verbeteren, is het meten bij hogere magnetische veldsterkten, bij scanners die bijvoorbeeld werken op een hoofdmagneetveld van 7 Tesla. De energie die wordt uitgezonden door radiofrequentiepulsen is echter hoger in spin-echo dan in gradient-echo en zij neemt toe met het kwadraat van de magnetische veldsterkte waarop de metingen uitgevoerd worden. Aangezien dit kan leiden tot een temperatuurstijging van levend weefsel, is het gebruik hiervan om veiligheidsredenen geen optie. De SSFP-sequentie (Steady State Free Precession) is een gradiënt-echosequentie waarvan het onwaarschijnlijk is dat deze zorgt voor oververhitting van het weefsel . Een kenmerk van deze sequentie is dat de tijd tussen opeenvolgende excitatie-radiofrequentiepulsen korter is dan de weefselrelaxatietijden. Dit leidt tot een complex MR-signaal dat enkele spin-echo-achtige kenmerken vertoont.

In **Hoofdstuk 8** werd corticale activering gemeten met behulp van de S2-SSFP-sequentie (een subtype van SSFP), waarbij de temporele parameters werden gekozen die het gemeten activeringssignaal in het weefsel zouden maximaliseren. De metingen leverden echter niet de verwachte resultaten op, aangezien de activeringsprofielen meer gelijk waren aan die verkregen met GE-BOLD dan met SE-BOLD. Om de mogelijke onderliggende redenen hiervoor te begrijpen, is het in hoofdstuk 6 ontwikkelde model aangepast om een benadering van een S2-SSFP-signaal te simuleren. Volgens de simulatieresultaten kunnen de parameters resulteren in een signaal met een grotere bijdrage van macrovasculatuur dan van microvasculatuur, en tonen ze daarom een niet-verwaarloosbare signaalspreiding door de aderen. De veranderingen in de timingparameters die vereist zijn om dit bijdragepatroon om te keren, zouden een nadelig effect hebben op de tijdsefficiëntie en de signaal-ruisverhouding van de verkregen beelden. Om die redenen lijkt de S2-SSFP-sequentie niet geschikt om laminaire activeringsprofielen te meten.

Vanwege de betere signaal-ruisverhouding en een hogere verwachte microvasculaire weging van het activeringssignaal, zijn de meeste laminaire activeringsstudies bij mensen uitgevoerd met een magnetische veldsterkte van 7 Tesla, hoewel het aantal scanners dat bij deze magnetische veldsterkte werkt klein is. Om de gemeten signaal-ruisverhouding verder te verbeteren, kunnen de corticale profielen worden gemiddeld over een geactiveerd deel van de cortex, waardoor een gemiddeld activeringsprofiel wordt verkregen. In **Hoofdstuk 9** werd de haalbaarheid van laag-specifieke functionele MRI bestudeerd bij magnetische veldsterkten lager dan 7 T, voor de geval dat gebruik van deze corticale integratiebenadering word gemaakt.

Er zijn twee soorten ruis in functionele MRI, de thermische en fysiologische ruis. De integratiebenadering compenseert alleen de thermische component van de ruis. Na het toepassen van integratie op een bepaald oppervlak, zal verdere integratie de temporele signaal-ruisverhouding niet verbeteren omdat fysiologische ruis de overhand heeft. In dit onderzoek nam de temporele signaal-ruisverhouding niet verder toe na integratie op een stuk van de cortex met 250 en 150 voxels, bij respectievelijk 1.5 T, 3 T en 7 T. Bij de beelden in deze studie zijn 250 voxels ruwweg gelijk aan een oppervlak van 140 mm^2. Na integratie opeen stuk cortex waarbij het signaal zeker gedomineerd werd door fysiologische ruis, waren de verkregen activeringsprofielen vergelijkbaar met die bij equivalente acquisitieparameters. De metingen bij 7 T presteren echter beter dan die bij lagere veldsterkten waar het gaat om de omvang van het gebied dat geïntegreerd moet worden en de snelheid waarmee een beeld kan worden verkregen. Echter, als de experimentele instellingen dit toestaan, is het mogelijk om corticale activeringsprofielen te meten op veldsterkten lager dan 7 T.

Samenvattend, in het eerste deel van dit proefschrift is een methode gepresenteerd om te corrigeren voor de signaalspreiding tussen corticale lagen en tegelijkertijd te profiteren van de voordelen van GE-BOLD acquisities. Vervolgens leidt de studie naar het gebruik van de S2-SSFP-sequentie om laminaire activeringsprofielen te verkrijgen die vrij zijn van signaalspreiding tussen lagen, tot de conclusie dat deze sequentie mogelijk ongeschikt is voor acceptabele acquisitietijden om hersenfunctie te meten. Als de experimentele omstandigheden ten slotte integratie op een stuk cortex en een lagere temporele resolutie mogelijk maken, kan het mogelijk zijn laminaire activering te meten bij veldsterkten lager dan 7 T.

Laburpena euskaraz

Erresonantzia magnetiko bidezko irudigintza funtzionala, MRI funtzionala, garuneko aktibazioa neurtzeko erabiltzen den teknika ez inbasibo bat da. Teknika honen helburua neuronen aktibitatea neurtzea da, baina, berez, egun MRI-n erabiltzen diren teknikekin, neuronen aktibitateak berauen inguruko sare baskularrean eragiten dituen aldaketak neurtzen dira. Hau da, neurona talde batek bere atseden egoeran baino aktibitate maila altuagoa duenean, beharrizan energetikoa hazi egiten da, eta metabolito eta oxigeno kontsumoa handitu. Zelulek euren beharrizan metabolikoak asebeteko dituztela ziurtatzeko, neuronen inguruko kapilareak eta arteriak dilatatu egiten dira, aktibazio eremuan odolaren bolumena eta emaria handituz.   MRI bidez oxigeno kontsumoaren, odol bolumenaren eta odol emariaren aldaketak neur daitezke, eta baita hiru hauen konbinazioa den seinale bat ere: BOLD seinalea (inglesez Blood Oxygenation Level Dependent signal).

1990eko hamarkadaren hasieran lehen aldiz hauteman zenetik, BOLD seinalea da MRI bidez garunaren aktibazioa neurtzeko gehien erabili den teknika. Goian aipatutako beste neurketekin alderatuz, neuronen aktibazioarekiko sentikorrena da, MRIko ekipamendu eta software ohikoarekin neurtzeko erraza eta garun osoaren irudi bat azkarren lortzea ahalbidetzen duena, 2-3 segundutan. Erresonantzia magnetikoaren fenomenoan oinarritzen ez diren eta garunaren funtzionamendua neurtzeko erabil daitezkeen teknikekin alderatuz (adibidez: elektroentzefalograma, magnetoentzefalograma edo positroien emisioen bidezko tomografia), abantaila nagusietako bat lor daitekeen irismena eta bereizmen espaziala dira. Hau da, prozesu kognitiboan garrantzitsuak diren eta garunaren erdialdean dauden egiturak neur daitezke (adibidez, hipokanpoa, amigdala edo talamoa) eta ohikoa da 3x3x3 mm^3-ko bereizmenarekin neurtzea.

Aipaturiko bereizmen horrekin funtzio jakin bat burutzean (adibidez, benetako eta asmaturiko hitzen artean ezberdintzea) garunean zein eremu aktibatzen diren antzeman daiteke, baina ezin daiteke eremuon arteko hierarkia eta elkarrekintza neurtu, suposaketa batzuk egin edo balizko eredu bat erabili gabe. Izan ere, neuronen arteko komunikazioa milisegundutako kontua da, egungo MRI teknikekin zuzenean neurtzeko azkarregia.

Kortexeko geruza mailako aktibazioa neurtzea aipatutako suposaketak egin gabe eremuen arteko elkarrekintza neurtzeko era bat izan daiteke. Kortexa, edo garun azala, garunaren azalera estaltzen duen ~3 mm-ko geruza da. Batez ere neuronen gorputzez osatua dago, garunean seinalearen prozesamendua gertatzen den lekua da, beraz. Garuneko parte gehienetan sei geruzatan banatuta dago. Eremu batek funtzio baten prozesamenduan duen rolaren arabera, geruza bat edo beste bat

aktibatuko da gehiago, eta honela eremuen arteko elkarrekintza ondorioztatu ahal izango da.

Kortexaren lodiera txikia dela eta, milimetro batez azpiko bereizmenarekin neurtu behar da. MRI bidezko irudiaren lorpenean eragiten duten gainontzeko faktore guztiak berdin mantenduz gero, MRIn seinale eta zarataren arteko erlazioa txikitu egiten da, bereizmena handitu ahala. Zailtasun teknikoak tarteko, MRIaren hastapenetan ez zen posible geruza mailako aktibazioa neurtzea. Hala ere, azken 15 bat urtetan, eremu magnetiko altuko eskanerrak eskuragarriago bihurtu dira, eta hardware zein irudiak lortzeko MRI-n erabiltzen diren sekuentzietan aurrerapen erabakiorrak izan dira. Aurrerapen horiei esker, egun posible da bereizmen espazial handiarekin, gutxieneko seinale eta zarata arteko erlazio batekin, eta neurozientzietan onargarria den abiadurarekin, MRI bidez irudiak lortzea.

Erresonantzia magnetiko bidez irudia lortzeko sekuentzia deituriko kode edo programak erabiltzen dira. Sekuentzia batean irudi bat lortzeko igorri behar diren radiofrekuentzia uhinen eta eragin behar diren eremu magnetikoaren aldaketen ordena eta iraupena definitzen dira Bi sekuentzia mota nagusi daude, spin-echo (SE) eta gradient echo (GE) izenez ezagutzen direnak. BOLD seinalea neurtzeko gehien erabiltzen dena gradient echo sekuentzia da, azkarragoa, sinpleagoa eta neuronen aktibazioarekiko sentikorragoa delako. Bere desabantaila nagusia neurtzen den aktibazioaren zatirik handiena 20 μm baino diametro handiagoa duten zainetatik datorrela da. Zain hauek aktibazio seinalea neuronen jarduna gertatu den ingurunetik kanpo barreiatzen dute, milimetro batzuetakoa izatera irits daitekeen distantzia bateraino, honela neurtzen den aktibazioaren zehaztasun espaziala okertuz. Tesi honen lehenengo hiru atal zientifikoetan (6, 7 eta 8. ataletan) zain hauen eragina aztertu, kuantifikatu eta zuzentzeko edo ekiditeko erak proposatu dira. 9. atalean, geruza mailako aktibazioa 7 Tesla baino eremu magnetiko ahulagoetan neurtzea bideragarria ote den aztertu da. Jarraian, atal hauetako azterketak eta ondorio nagusiak hitz lauz azalduko dira.

Tesi honetako lehenengo ikerketan geruza mailako BOLD seinalearen karakterizazioa eta barreiapen espaziala aztertu da (**6. atala**). Horretarako, kortexeko sare baskularraren eredu bat garatu da. Eredu hau literatura zientifikoan argitaratutako ikerketa anatomiko eta fisiologikoetan oinarritzen da, eta kortexean zehar mikrobaskulaturak (∅<20 μm duten zainek osatua) eta makrobaskulaturak (∅ >20 μm duten zainek osatua) dituen aldaketak egoki islatzen ditu.

Eredu hau erabiliz kortexean zeharreko spin eta gradient echo bidez neurturiko BOLD aktibazioa simula daiteke, eta lortzen diren profilak esperimentalki lortzen direnen antzekoak dira. Eredu honek, halaber, aktibazio puntuaren dispertsio funtzioa (ingelesez Point Spread Function, PSF) balioztatzea ahalbidetzen du. Hau da, puntu (edo kasu honetan geruza) batean gertatzen den aktibazioak

gainontzeko geruzetan duen eragina kuantifikatu da. Arkitektura baskularraren ezaugarrietako bat da, kortexeko odola gainazalari elkarzutak zaizkion zainen bitartez, beti norabide bakarrean drainatzen dela, hots, aktibazioa gertatu den geruzatik hasi eta kortexaren gainazalererantz. Beraz, balioetsitako PSFa, simetrikoa izan beharrean, gainazaleranzko norabidean okerturik dago: aktibazio geruzan tontor bat eta gainazalerantz nahikoa konstante mantentzen den magal bat du. PSF fisiologikoa geruza ezberdinen artean oso antzekoa da, desberdintasun nagusia magalaren luzera delarik; zenbat eta gainazaletik gertuago egon, orduan eta laburragoa.

Hurrengo pausu logikoa lorturiko PSF fisiologikoaren ezagutza GE-BOLD profiletan ematen den geruzen arteko seinalearen barreiatzea zuzentzeko erabiltzea zen (**7. atala**). Intuizioz, MRI bidez neurturiko aktibazio profila, geruzen aktibazio profilaren eta PSF fisiologikoaren arteko konboluzioaren emaitza da. Beraz, kontrako prozesua eginez, neurturiko profilaren eta PSFaren arteko dekonboluzioa kalkulatuz, barreiapen gabeko profilak lortzea posible izan beharko litzateke. Zuzenketa metodo hau bi datu-multzotan frogatu da. Bi kasuetan, zuzenketa egin ondoren lorturiko emaitzak barreiapen arazo gutxiago duten metodoekin (spin echo sekuentziarekin neurtutako BOLD aktibazioa, adibidez) lortutakoen antzekotasun handiagoa dute. Aktibazio profilen lagin kopurua erabilitako prozesamendu eta ikerlariaren araberakoa izaten denez, laginketa desberdinentzako PSFaren balioa nola doitu ere azaldu da atal honetan. Etorkizunean, dekonboluzio metodoaren zehaztasuna balioztatu behar da, horretarako neurketa-saio berean seinalearen barreiapen arazoa duen eta ez duen bi sekuentziekin neurtu eta emaitzak alderatu behar dira.

Aukeran, hobeto da zainen bidezko barreiapenarekin arazorik ez duen sekuentzia batekin neurtzea. Adibidez, lehen aipatu bezala, spin echo sekuentzia batekin. Aktibazioarekiko sentikortasun txikiagoa duenez, hau hobetzeko eremu magnetiko altuagoko eskanerrekin neurtu daiteke, 7 Teslako eremu magnetikoa duten eskanerretan, adibidez. Spin echo sekuentzietan, baina, radiofrekuentzia uhinen bidez energia gehiago transmititzen da, zeina eremu magnetikoaren karratuarekin hazten den. Honek ehun bizidunaren berotze bat ekar dezake, eta beraz, segurtasun arrazoiak tarteko, ez da eremu magnetiko altuetan beti erabil daitekeen sekuentzia bat. SSFP (Steady State Free Processing) izeneko sekuentzia, gradient echo sekuentzia bat da eta ez du ehunaren gehiegizko beroketarik eragingo. Hala ere, sekuentzia honetan radiofrekuentzia uhinen artean dagoen denbora tartea ehunaren ezaugarri bat den erlaxazio denbora baino askoz motzagoa delako, spin echoz neurtzen den seinalearen ezaugarriak ere badituen seinale konplexu bat neurtzea ahalbidetzen du.

Ezaugarri hauek direla eta, **8.atalean** aktibazioa S2-SSFP sekuentzia (SSFP-aren aldaera bat) erabiliz neurtu da, sekuentziaren parametro tenporalak ehunean aktibazio maximoa neurtzeko moduan aukeratuz. Baina lortutako emaitzak ez

dira esperotakoak izan, SSFP profilak gradient echo bidez lortutakoen itxura gehiago dutelako spin echo bidez espero daitezkeen profilak baino. Honen arrazoiak ulertu ahal izateko, 6. atalean garaturiko ereduan S2-SSFP bidezko seinalea simulatu ahal izateko beharrezko aldaketak egin ziren. Hauek erakusten dutenez, erabilitako parametroekin, posible da sare makrobaskularraren seinalea mikrobaskularrarena baino handiagoa izatea eta beraz seinaleak barreiapen maila altua izatea. Erlazio hau alderantzikatzeko sekuentziaren denboretan egin beharreko aldaketek eragin negatiboa lukete sekuentziaren efizientzia tenporalean eta aktibazioarekiko sentikortasunean. Beraz, sekuentzia hau ez da geruzetako aktibazioa neurtzeko aukera egokia.

Seinale eta zararaten arteko erlazio hobea lortzen delako eta BOLD seinalean mikrobaskulaturak pisu haundiagoa duela aurreikusten delako, 7 Tesla izan da gizakietan geruza mailako aktibazioa neurtzeko eremu magnetikorik erabiliena, nahiz eta mundu mailan mota honetako eskaner kopurua oso urria den. Neurtutako seinale eta zararaten arteko erlazioa are gehiago hobetzeko, eremu bateko aktibazio profilak elkarrekin batu edo integratu, daitezke, aktibazioaren batazbesteko profila lortuz. Tesi honen **9. atalean** profilen seinale eta zararaten arteko erlazioa hobetzeko metodo hau erabiliz geruza mailako aktibazioa 7 Tesla (T) baino eremu magnetiko ahulagoa darabilten eskanerretan bideragarria ote den aztertu da.

MRI funtzionalean bi zarata mota daude, termikoa eta fisologikoa, eta integrazio metodo honekin zarata termikoaren eragina konpentsatzen da. Azalera jakin batetik gora, integrazio eremua handitu arren, ez da lortuko seinale eta zararaten arteko erlazioa gehiago hobetzerik, zarata fisiologikoa nagusi delako. Ikerketa honetako emaitzen arabera, gehiago hobetu ezin den seinale eta zarata erlazioa lortzeko integratu beharreko eremua 250, 150 eta 100 voxel-ekoa da 1,5 T, 3 T eta 7 Tn, hurrenez hurren. 250 voxel gutxi gorabehera 140 mm^2-ko azaleraren baliokidea da, kasu honetan. Beraz, 7 Tn integratu beharreko eremua txikiagoa da (hots, aktibazio eremuak txikiagoak izan daitezke) eta datu bilketa efizienteagoa da irudiak lortzeko denbora gutxiago behar delako. Hala ere, baldintza esperimentalek muga horien barruan neurtzea ahalbidetzen badute, posible izan daiteke 7 T baino eremu magnetiko ahulagoa duten eskanerrekin neurtzea.

Laburbilduz, tesi honetan GE-BOLD neurketek dituzten abantailekin neurtu eta barreiapenaren arazoa zuzentzea ahalbidetzen duen metodo bat aurkeztu da lehendabizi. Jarraian, neurketa denbora garunaren funtzionamendua ikertzeko onargarria izatekotan, S2-SSFP neurketa metodoa seinalearen barreiapen arazorik gabeko aktibazio profilak neurtzeko ez dela egokia ikusi da. Azkenik, baldintza esperimentalak bateragarriak badira kortexean zehar seinalea integratzearekin eta efizientzia tenporala txikiagoa izatearekin, geruza mailako aktibazioa 7 T baino eremu magnetiko ahulagoa duten eskanerretan neurtzea posible da.

List of publications

Journal Articles:

Markuerkiaga, I., Barth, M., & Norris, D. G. (2016). A cortical vascular model for examining the specificity of the laminar BOLD signal. Neuroimage, 132, 491-498.

Markuerkiaga, I., Marques, J.P., Bains L.J., & Norris, D.G. An *in-vivo* study of BOLD laminar responses as a function of echo time and static magnetic field strength *(Submitted)*

Markuerkiaga, I., Marques, J.P., Gallagher T.E., & Norris, D.G. Estimation of Laminar BOLD activation profiles using deconvolution with a physiological point spread function *(Submitted)*

Oral presentations and invited talks:

Markuerkiaga, I., Barth, M & Norris,D.G. Investigation of the echo-time dependence of laminar BOLD profiles using a vascular model of the cortex, ESMRMB 2015, Edinburgh

Markuerkiaga, I., Barth, M & Norris,D.G. A vascular model for examining the layer specificity of SE and GE BOLD, HiMR Summer School, 2016, Elba

Markuerkiaga, I., Marques J.P. & Norris, D.G. Deconvolving the laminar gradient echo activation profiles with the spatial PSF: an approach to revealing underlying activation patterns. ISMRM Benelux 2016, Eindhoven

Markuerkiaga, I., Marques J.P. & Norris, D.G. Deconvolving the laminar gradient echo activation profiles with the spatial PSF: an approach to revealing underlying activation patterns. ISMRM 2016, Singapore

Markuerkiaga, I., Marques J.P. & Norris, D.G. A cortical vascular model for examining cortical BOLD profiles, June 2016, Max Planck Institute for Human Cognitive and Brain Sciences, Leipzig

Markuerkiaga, I., Lauren J. Bains, Marques J.P. & Norris, D.G. An *in-vivo* study of BOLD laminar responses as a function of echo time and magnetic field, ISMRM 2017, Honolulu

Guidi, M., **Markuerkiaga I.**, Bains, L., Huber L., Moeller H.E., & Norris D.G., Frequency Signature of Cortical Laminar fMRI, ISMRM 2017, Honolulu

Acknowledgements

This work would not have been possible without the support of many people. It has been a privilege to work with such talented and kind people.

First I would like to express my sincere gratitude to my supervisor and promotor, David Norris, for giving me the opportunity of doing a PhD in the MR methods group at the Donders Institute. Thank you for your scientific guidance and advice over all the projects we have undertaken. I appreciate your openness to discuss any topic, even the small, less relevant side-ideas, and your responsiveness, both during my time at the Donders and after. And of course, thank you for your supportive and positive attitude, both personally and professionally.

I would like to thank Jose Marques for his support and discussions in the multi-field project and the deconvolution approach, and in any other topic, to be honest. Thank you for also giving feedback on the introductory chapters of this thesis and being so supportive anytime I walked in your office.

I thank Markus Barth for valuable discussions and providing me with the key references of cortical vasculature and physiology that served as the basis for the project on the simulation of cortical BOLD activation profiles.

I am thankful to Lauren Bains for helping me out with the measurements at 1.5 T and 7 T and helping me organise participants and trips to Essen. Ich möchte mich auch bei dem Team in dem Erwin Hahn Institut bedanken, insbesondere bei Stefan Maderwald, der sich immer Zeit genommen hat die korrekten Sequenzparameter oder das letzte Problem mit dem Scanner ausführlich zu erklären.

I thank Vahid Malekian for the SSFP sequence and Peter Koopmans, Natalia Petridou and Alessio Fracasso, Peter Kok, Renee Scheeringa, Tim van Mourik and Dan Sharoh for providing me with various sets of MRI functional data to test the deconvolution approach. I thank Dan also for a few spontaneous but lengthy talks on laminar connectivity and his critical comments on Chapter 5 in this thesis. I acknowledge here the anonymous reviewers who contributed to improving the quality and understandability of the submitted articles.

I am grateful to Tara Gallagher, whose eagerness to learn provided the push that the deconvolution project needed. Maria Guidi has been my mate in the distance to whom I owe some useful articles, stimulating discussions and therapeutic laughs.

My PhD position would not have been possible without Penny Gowland, who, as I understand, had the drive and made most of the hard work to put together the successful Marie Curie proposal that became the High Field MRI (HiMR) Marie Slodowska Curie Initial Training Network. Although it comprised a decent

amount of traveling, I sincerely appreciate the training program that Penny and the rest of supervisors in the ITN put together in an attempt to make proper MR researchers out of us. Lesley Martin deserves to be acknowledged as the most patient and understanding assistant. Regarding my time before the PhD, I would like to thank Daniel Padro for introducing me to NMR and MRI and Torsten Reese for encouraging me to take on this PhD position.

I thank the MR group members, past and present, for our collective effort to become better at MRI through the various MR Seminars, Physics Clubs and group lunches that we shared over these last years. A special thank goes here to Jenni Schulz and Jose Marques for accepting to be my paranymphs and to Alberto Llera, our lunch-time mentor on statistical analysis.

I would like to acknowledge the Donders as heaven on Earth of working environments. Through conscious decisions, the management has promoted a fulfilling and stimulating environment, in which it is encouraged that everyone speaks up and that they are heard. Thank you to all the support staff in the technical group, administration and lab manager for being so responsive and swiftly coming up with solutions. As a foreigner who has moved to and from the Netherlands with all the hassle that goes with it, a special mention goes to Tildie and Nicole, Sandra and Ayse in the administration team, who were always so helpful. And of course, I have to thank the Italians for their delicious food and cheerful welcoming in the canteen.

Nijmegen has given me some good friends that I deeply appreciate. I hope that we will be able to overcome the distance and keep in touch in the years to come. I specially want to thank Soley (my unofficial paranymph, among other things), Laura, Sonja, Andi and Zahra for their friendship, for helping me out with moving or opening their home whenever I went back to Nijmegen these last months. I thank Sonja, Nicole, Eric en Linda, die met mij Nederlands heben gesproken. Met jullie hulp end geduld heb ik me in deze land iets meer thuis gevoeld. Dank je nog eens, Sonja, voor de nederlandse samenvatting.

I would also like to express my gratitude to the 'Amsterdam/Harlem Connection'. Muchas gracias, Marta y Rebeca, por invitarme a los planes tan chulos que organizáis. Eskerrik asko baita ere Henrike eta gainerako Euskal Borrel-zaleei hilabeteko azken ostiralean Amsterdamen piskat etxekoagoa den zita jartzeagatik.

Hierbei, möchte ich mich bei der Stuttgarter Clique, ob in Stuttgart, Hamburg oder Berlin, für eure Gastfreundschaft und das Gefühl, dass es sich unter euch immer noch wie ein zweites Zuhause fühlt, bedanken.

Azkenik, Tobatarrak eta lagunak eskertu nahiko nituzke. Esker berezi bana Amaiari, euskarazko laburpenari eginiko zuzenketengatik, Nekaneri, nire lanean hainbeste interes izateagatik, Loreari, behar izan ditudanean jasotako mezu eta bisitengatik, Miren eta Potzuri, azken urteetan zuen bizitza bihurtu den zoramen ordenatu horretan lekua egiteagatik eta Joane, Paule, Koldo eta Leireri, egoteagatik.

Eta batez ere eta beti, aitari eta amari.

Biography

Irati Markuerkiaga (1983) was born and raised in Markina-Xemein, Basque Country, Spain. After graduating from High School in 2001, she went on to study a bachelor's degree in Telecommunications Engineering in Mondragon Unibertsitatea. In order to broader her cultural horizons, in 2005 she moved to Germany and pursued her studies in Electrotechnical Engineering at the University of Stuttgart. It was here, in a course on biomedical engineering, that she first became acquainted with magnetic resonance imaging. After graduating in 2008, she spent a gap year in Brussels learning about topical European issues and working at the European Commission in the Microsystems unit. In 2010 she took on a position as a technician in the NMR/MRI platform in CIC Biomagune, in Donostia-San Sebastian. She combined this position with a master's degree on Biomedical Engineering at the Public University of Navarre. In order to learn more about MRI, in 2013 she started a PhD on layer specific fMRI at the Donders Institute, in Nijmegen, under the supervision of David Norris.

Donders Graduate School for Cognitive Neuroscience

For a successful research Institute, it is vital to train the next generation of young scientists. To achieve this goal, the Donders Institute for Brain, Cognition and Behaviour established the Donders Graduate School for Cognitive Neuroscience (DGCN), which was officially recognised as a national graduate school in 2009. The Graduate School covers training at both Master's and PhD level and provides an excellent educational context fully aligned with the research programme of the Donders Institute.

The school successfully attracts highly talented national and international students in biology, physics, psycholinguistics, psychology, behavioural science, medicine and related disciplines. Selective admission and assessment centres guarantee the enrolment of the best and most motivated students.

The DGCN tracks the career of PhD graduates carefully. More than 50% of PhD alumni show a continuation in academia with postdoc positions at top institutes worldwide, e.g. Stanford University, University of Oxford, University of Cambridge, UCL London, MPI Leipzig, Hanyang University in South Korea, NTNU Norway, University of Illinois, North Western University, Northeastern University in Boston, ETH Zürich, University of Vienna etc. Positions outside academia spread among the following sectors: specialists in a medical environment, mainly in genetics, geriatrics, psychiatry and neurology. Specialists in a psychological environment, e.g. as specialist in neuropsychology, psychological diagnostics or therapy. Positions in higher education as coordinators or lecturers. A smaller percentage enters business as research consultants, analysts or head of research and development. Fewer graduates stay in a research environment as lab coordinators, technical support or policy advisors. Upcoming possibilities are positions in the IT sector and management position in pharmaceutical industry. In general, the PhDs graduates almost invariably continue with high-quality positions that play an important role in our knowledge economy.

For more information on the DGCN as well as past and upcoming defences please visit: http://www.ru.nl/donders/graduate-school/phd/